Solution and Interfacial Properties of Cyclic Containing Anionic Surfactants

Deeming, Laura

2025

Solution and Interfacial Properties of Cyclic Containing Anionic Surfactants

LAURA DEEMING
PHYSICAL CHEMISTRY | FACULTY OF SCIENCE | LUND UNIVERSITY

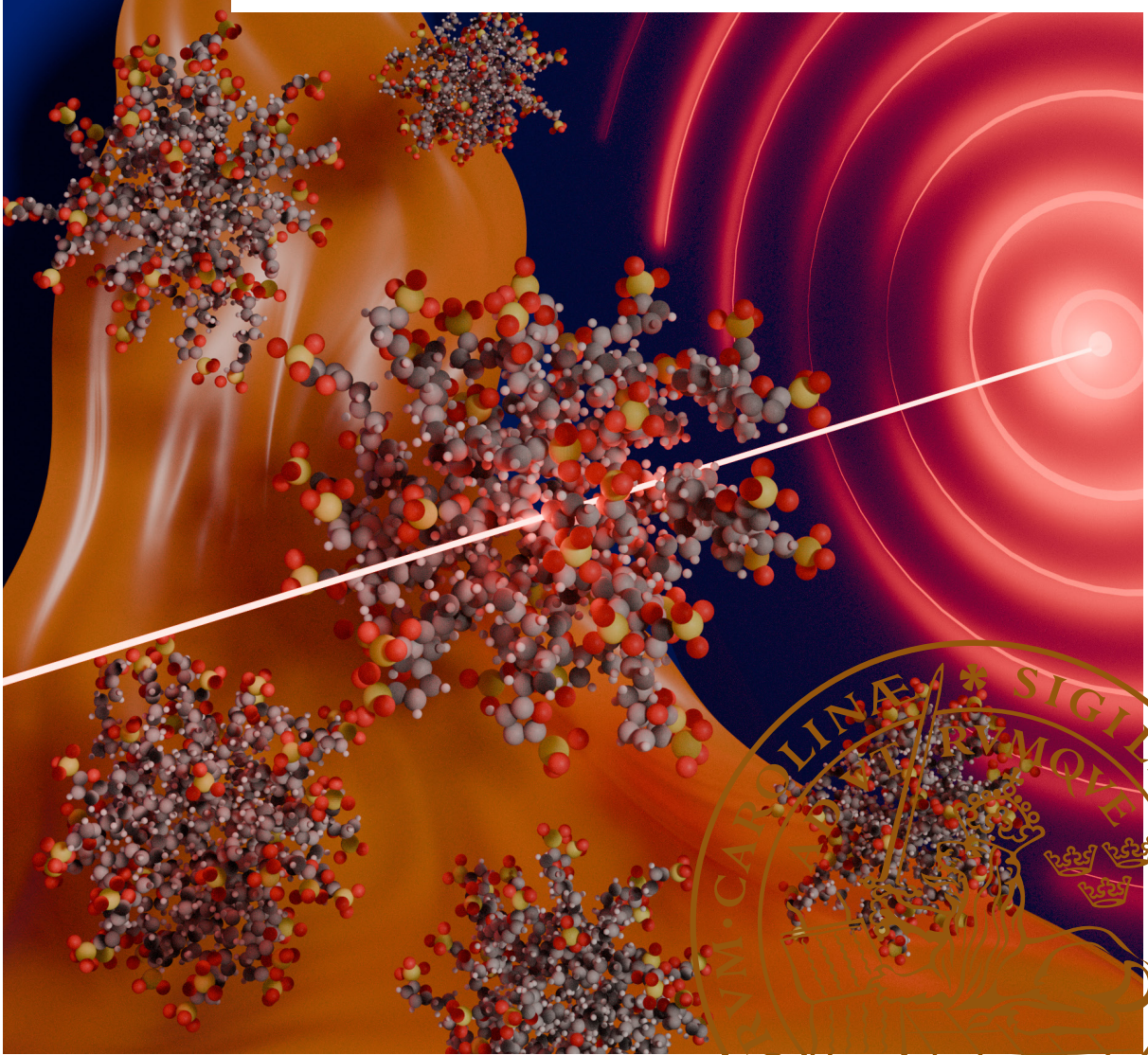

Solution and Interfacial Properties of Cyclic Containing Anionic Surfactants

Solution and Interfacial Properties of Cyclic Containing Anionic Surfactants

Laura Deeming

LUND
UNIVERSITY

DOCTORAL DISSERTATION

Doctoral dissertation for the degree of Doctor of Philosophy (PhD) at the Faculty of Science at Lund University to be publicly defended on 26th of September 2025 at 13.00 in Lecture Hall A, Department of Chemistry, Lund University

Faculty opponent:
Dr. Alison Paul, School of Chemistry, Cardiff University, United Kingdom

Solution and Interfacial Properties of Cyclic Containing Anionic Surfactants

Laura Deeming

LUND
UNIVERSITY

Cover photo by David Ribar

Division of Physical Chemistry
Department of Chemistry
Lund University

ISBN (printed): 978-91-8096-112-7
ISBN (digital): 978-91-8096-113-4

Printed in Sweden by Media-Tryck, Lund University, Lund 2025

Isn't it funny, day by day nothing changes but when you look back, everything is different – C.S Lewis

Table of Contents

Acknowledgements i
Popular Science Summary ii
List of Publications iii
Author Contributions iv
Abbreviations v

Introduction – Fundamentals 1

1 Surfactants 2

1.1 Bulk Solution Surfactant Behaviour 3
1.2 CMC Determination 5
1.2.1 Surface Tension 5
1.2.2 Conductivity 7
1.3 Surfactant and Micelle Structures 8
1.4 Surfactant Adsorption at the Air-Water (A-W) Interface 9
1.5 Surfactant Choices 11
1.5.1 Currently used: Linear alkylbenzene sulfonate (LAS) 11
1.5.2 Surfactant of interest: Oleo-furan sulfonates (OFS) 12
1.5.3 Conventional anionic: Sodium Dodecyl Sulfate (SDS) 13
1.5.4 Conventional non-ionic: Hexaethylene glycol monododecyl ether ($C_{12}E_6$) 14
1.6 Surfactant Mixtures 15
1.7 Relevance to Formulation and Detergency 18

2 Scattering Techniques 19

2.1 Small-Angle Scattering 20
2.2 Small-Angle X-Ray Scattering (SAXS) 21
2.3 Small-Angle Neutron Scattering (SANS) 22
2.4 Neutron Reflectometry 25
Modelling the reflectivity profile 26
Application to surfactant systems 27
2.5 Total Neutron Scattering 28
2.6 Empirical Potential Structure Refinement (EPSR) 29

3 Summary of Results 31
3.1 STFS Alone 31
3.2 Mixture 1: STFS/$C_{12}E_6$ 32
3.3 Mixture 2: STFS/SDS 32
3.4 Mixture 3: STFS/SDS/$C_{12}E_6$ 33
3.5 Ring Comparison 34
4 Conclusions and Future Outlook 35
5 References 36
Paper I-III 41

Acknowledgements

I'd first like to thank **Karen**, for bringing me on a journey that I couldn't have imagined. If you'd have told me everything that has happened in the last 5 years, I wouldn't believe it. Thank you for shaping me into an independent person and for giving me these opportunities.

Thank you to all the beamline scientists I've worked with over the last 5 years, especially **James Doutch**, **Tristan Youngs** and **Daniel Bowron**; your knowledge and willingness to answer any question, no matter how simple has been greatly appreciated. To **Hanna**, thank you for your kindness and help with NR when I was clueless.

To my research group, past and present: **Brad, Iva, Zakir, George, Jake, Maggie, Ronak, Subramee, Krishna, Petteri, Glenn and Nguyen**. Thank you for all the laughs, hugs and beamtime sleep deprivation support.

To **Niamh**, **Elly** and **Ellen**, my office companions, thank you for being exactly what I needed through the different stages (logic, comfort and advice – I'll let you decide who is who!) and for always being willing to yap. Bonus thank you to **Ellen** and **Luke** for taking care of me in the last stretch of this PhD and to **Natalie**, the tiniest and best new addition, thank you for proving the scientific fact that holding a baby is the best stress relief.

To my "Bath Life" and Dev-family: **Nat, Millie, Col, Andrew** and **Giles**. Thank you for shaping the start of this journey and introducing me to Catan (even if we are never allowed to play together again..). And to **Sophie**, my "anything can be sangria" friend, for being a constant source of laughter and chaos even across the world. To **Harriet** and **Charl,** I know you still don't know what I do but I know you'll always be my loudest cheerleaders.

And then after a terrifying move to Sweden two years into the PhD (wouldn't recommend doing that again!), I was lucky to land amongst more incredible people. To the Phys Chem crew - **Davide, Erika, Gianluca, Gisele, Jen, Marco, Marija, Nicole, Noemi, Sebastian, Sophie** and everyone I've been lucky enough to meet. Thank you for encouraging me to slow down, take plenty of fika breaks and feeding me when I forget. To **David**, **Franci** and **Isabel**, my little micelle, the last year has been so special with you, and I can't thank you for your support enough.

To my family – **Alison, Tony, Nikki & Max**. Thank you for your unwavering support and for always being there for me, even from afar.

And finally, to **Phil**. You have been my rock throughout this journey and your belief in me, even when I doubted myself, kept me going more times than I can count.

Popular Science Summary

Every time we do our laundry, there are many complex processes at work to remove oil and dirt from our clothes. Within our detergent there are many components, all with varying functions including enzymes for targeted stain removal, buffers for pH regulation, thickeners to tune the viscosity and additives like fragrances and preservatives. However, the key ingredients that underpin the vast majority of the mechanisms in these commercial products are surfactants, which are molecules that help oil and water mix. These amphiphilic molecules adsorb at oil/dirt interfaces and lift them away from clothing before removing them in the wash.

All formulations use a combination of surfactants, and this work aims to investigate interactions between these species, for a surfactant with a unique structure that has not previously been explored in depth in literature in mixtures with two common surfactants. By exploring their behaviour in binary and ternary mixtures, in the bulk as well as at the air-water interface, we can investigate the effect this surfactant structure has on the self-assembly behaviour.

This work aims to provide new insights into how different types of surfactants work together and contribute to the development of more environmentally friendly formulations, whilst still retaining the high cleaning performance of the currently used surfactants.

List of Publications

I Mixed micellar solutions of an oleo-furan sulfonate surfactant with anionic and non-ionic surfactants

L. Deeming, N. R. Leaman, D. Honecker, Y. Chen, K. Ma, K. J. Edler

Journal of Colloid and Interface Science, 2025, 699, 138201

II Composition of mixed oleo-furan sulfonate containing systems at the air-water interface

L. Deeming, I. Manasi, E. Wilson, M. Kroon, R. Welbourn, K. J. Edler

Manuscript in preparation for submission

III Water and counterion structuring around cyclic anionic surfactant micelles in solution

L. Deeming, N. Leaman, D. T. Bowron, T. G. A. Youngs, J. Poon, K. J. Edler

Manuscript in preparation for submission

Author Contributions

Paper I

I planned and performed the experimental work and data analysis. For the neutron scattering experiment, I was assisted by Niamh L, Dirk H and Karen E. Deuterated samples were provided by Yao C and Kun M. I wrote the paper with feedback from other authors.

Paper II

I planned and performed the experimental work and data analysis. For the neutron reflectivity experiment, I was assisted by Iva M, Ellen W, Maggie K and Rebecca W. Karen E assisted with data analysis. I wrote the paper with feedback from other authors.

Paper III

I planned and performed the experimental work and data analysis. For the neutron scattering experiment, I was assisted by Niamh L and Karen E. Daniel B, Tristan Y and Karen E assisted with simulation set up and analysis. Jai-Fei P provided deuterated materials. I wrote the paper with feedback from other authors.

Abbreviations

A-W	air – water interface
CMC	critical micelle concentration
CPP	critical packing parameter
D_2O	deuterium oxide / heavy water
EPSR	empirical potential structural refinement
HMF	hydroxy methyl furfural
LAS	linear alkylbenzene sulfonate
MAC	maximum additive concentration
NR	neutron reflectivity
OFS	oleo furan sulfonate
RMSA	rescaled mean spherical approximation
RST	regular solution theory
SANS	small-angle neutron scattering
SAXS	small-angle x-ray scattering
SDBS	sodium dodecyl benzene sulfonate
SDS	sodium dodecyl sulfate
SLD	scattering length density
STFS	sodium tetradecyl furan sulfonate

Introduction – Fundamentals

Commercial surfactants are predominantly derived from non-renewable petrochemical sources, and a growing public demand for sustainability has driven research into bioderived alternatives. While environmental impact is a driving force behind the search for sustainable surfactants, their performance cannot be compromised and must match that of established commercial surfactants, if they are to be viable replacements. Linear alkylbenzene sulfonate (LAS), the most widely used anionic surfactant, remains unmatched in terms of cost-effectiveness and large-scale commercial viability. Although LAS is biodegradable[1], it is currently produced from petrochemical feedstocks.

This project explored a structurally related surfactant, sodium tetradecyl furan sulfonate (STFS), which can be synthesised from sustainably sourced precursors. The aim was to determine how this new species behaves within the complex surfactant mixtures commonly found in formulated products.

1 Surfactants

Surfactants (derived from *surf*ace *act*ive age*nts*) are amphiphilic molecules composed of a hydrophobic tail, typically a long hydrocarbon chain, and a hydrophilic headgroup that exhibits strong affinity for polar solvents such as water. This dual character causes surfactants to preferentially adsorb at interfaces between immiscible phases (e.g. air-water or oil-water), where they reduce interfacial tension by disrupting the cohesive interactions within the polar phase.

Upon dissolution in water, and above both the critical micelle concentration (CMC) and Krafft Temperature (T_k), surfactant molecules spontaneously self-assemble into micelles (Figure 1). These thermodynamically stable aggregates minimise the free energy of the system by sequestering the hydrophobic tails within the micelle core, while orienting the hydrophilic headgroups outward to maintain favourable interactions with the polar aqueous environment.

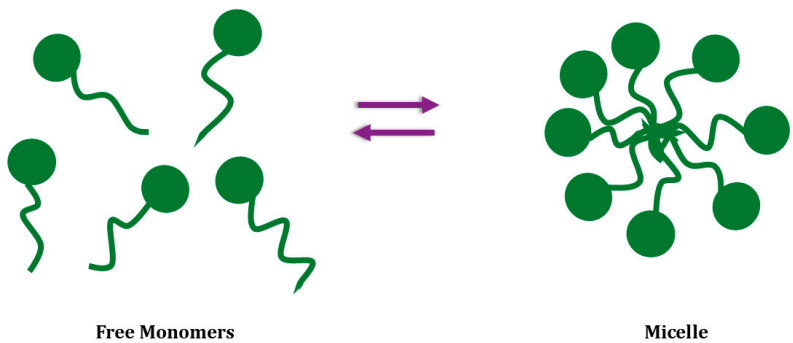

Figure 1: Schematic illustration of the dynamic equilibrium of micellization between surfactant monomers and micelle.

The amphiphilic nature of surfactants facilitates the solubilisation of hydrophobic substances in aqueous environments, a property extensively exploited in the detergency industry to remove oil- and grease-based contaminants using water. Beyond detergency, surfactants are also widely employed to functionalise surfaces[2,3], stabilise emulsions[4–6] and manipulate interfacial properties across a range of commercial formulations.

Given their versatility, surfactants are broadly categorised based on the nature of their hydrophilic headgroup into four main classes, as outlined in Figure 2.

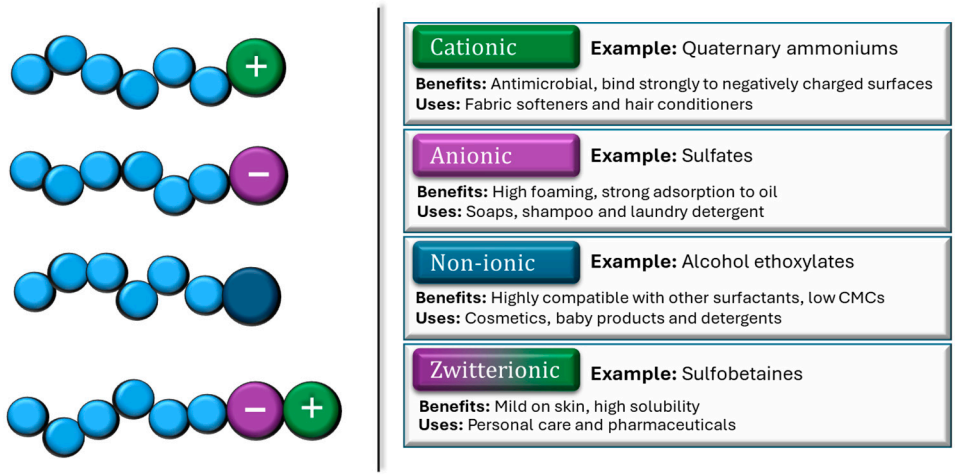

Figure 2: Overview of the four main classes of surfactants, highlighting their typical molecular structures, key functional benefits and common applications.

The surfactants studied in this work fall within the anionic and non-ionic classes, with these two categories frequently combined in detergent formulations. The complimentary properties of ionic and non-ionic species can be exploited to enhance performance, improve solubility, and lower the overall critical micelle concentration of the system.

1.1 Bulk Solution Surfactant Behaviour

A fundamental parameter in characterising surfactant behaviour in solution is the critical micelle concentration (CMC), defined as the bulk surfactant concentration at which micelle formation becomes thermodynamically favourable, and further surfactant addition primarily increases the micelle population while the monomer concentration remains essentially constant.

Micelle formation also only occurs above the Krafft temperature, the minimum temperature at which the surfactant is soluble. The CMC itself is influenced by various factors including temperature, ionic strength (e.g. salt addition) and the presence of co-solutes such as polymers or additional surfactants, all of which can modulate the micellisation process.

The thermodynamics of micellisation can be described using Gibbs free energy[7]:

$$\Delta G = \Delta H - T\Delta S \quad (1)$$

where **ΔG** is the change in Gibbs free energy, **ΔH** is the enthalpic contribution, **T** is the absolute temperature in Kelvin and **ΔS** is the entropic contribution. For micellisation to occur spontaneously, **ΔG** must be negative.

In most surfactant systems, ΔH is relatively small and positive, particularly for surfactants with lower CMCs, making the process predominantly driven by entropy. The entropy changes associated with micelle formation arise from several competing contributions.

On one hand, the translational entropy of surfactant monomers decreases upon micellisation, as the individual free monomers aggregate into a more ordered structure. This leads to fewer possible spatial configurations and a negative entropy contribution ($\Delta S < 0$).

On the other hand, two major factors contribute positively to the overall entropy: the release of structured water molecules into the bulk solvent and the increase in conformational freedom of the hydrocarbon tails. Prior to micellisation, water molecules form hydration shells around individual hydrophobic tails, limiting their mobility. Upon micellisation, these water molecules are released into the bulk solvent, thereby increasing their degrees of freedom. Additionally, within the micellar core, the surfactant tails are no longer constrained by the hydration shell, allowing for increased conformational flexibility. Both of these factors result in a positive entropy contribution ($\Delta S > 0$).

Overall, the positive entropic contributions, arising from the release of structured water and the increased conformational freedom of hydrophobic chains, outweighs the negative contribution associated with the more ordered structure of the micelle compared to free monomers. And as a result, micellisation occurs spontaneously under appropriate conditions (i.e. above the CMC and Krafft temperature).[7] The extent to which these opposing contributions influence micellisation can vary depending on surfactant structure and the presence of co-surfactants.

Micellar systems are often described using the pseudo-phase approximation, a thermodynamic model in which micelles are treated as a distinct pseudo-phase entities in equilibrium with free surfactant monomers in bulk solution as well as the surface.[8] Within this framework, micellisation is conceptualised as a phase transition and the equilibrium between monomeric and aggregated states is governed by the equality of the chemical potentials. That is, at equilibrium, the chemical potentials of the micellar pseudo-phase, the monomeric species in bulk solution, and any surface-adsorbed surfactant are equal. Below the CMC, the surfactant chemical potential increases logarithmically with concentration.[9]

This approximation facilitates the application of thermodynamic tools, such as the Gibbs–Duhem relation[10], to analyse micellisation equilibria and derive meaningful macroscopic parameters. One such parameter is the standard free energy change of micellisation, ΔG_{mic}, which can be related to the CMC using:

$$\Delta G^0_{mic} = RTlnCMC \quad (2)$$

where **R** is the gas constant (8.314 $Jmol^{-1}K^{-1}$), **T** is the temperature in Kelvin and the **CMC** is expressed in molar units. This relation allows for a quantitative comparison of how thermodynamically favourable micellisation is across different surfactant systems, using experimentally measurable quantities such as the CMC.

1.2 CMC Determination

Micelle formation is typically accompanied by abrupt changes in most physical properties, and many experimental techniques have been used to quantify the changes and determine a CMC. Common methods include surface tension, fluorescence, osmotic pressure, NMR and conductivity, with review papers available to discuss the advantages and limitations of each method.[11–13] In this work, surface tension and conductivity were used to determine CMCs for the systems studied, providing complementary insights into micellisation behaviour.

Although it is standard practice to report a singular CMC value, in actuality, the determined value can vary depending on the technique used, surfactant purity and the experimental conditions. As a result, a range of CMC values is often reported for a given surfactant.[13]

1.2.1 Surface Tension

Surface tension, or the surface free energy per unit area, is one of the earliest techniques for characterising micellisation[14,15] and remains a widely used fundamental method for studying surfactant adsorption at the air-water interface.

Several experimental approaches exist for determining the CMC using surface tension including the Wilhelmy plate, pendant drop and sessile drop methods[9]. The du Noüy ring method[16] was used as the primary method for this work, in which a platinum-iridium ring is slowly raised through the aqueous phase to the air-water interface, and the maximum force exerted on the ring is measured. This force can then be related back to the surface tension using known correction factors to account for the geometry of the ring. The pendant drop method[17] was used in Paper III due to a need for small sample volumes. This techniques involves taking an image of a

suspended liquid drop and calculation of the surface tension using the Young-Laplace equation[18] from the shape and curvature of the drop.

Surface tension is first measured for pure water, followed by incremental additions of a known concentration of surfactant stock solution. After equilibration, another surface tension value is recorded, and the CMC determined from the intersection from linear extrapolation of two straight lines in the surface tension isotherm (Figure 3a). Pure water has high cohesive forces due to hydrogen bonding between the molecules leading to a surface tension of 72 mN/m at 25 °C[19], although this is temperature dependent and decreases to 67.9 mN/m at 50°C.[20] Below the CMC, surface tension decreases progressively with increasing surfactant concentration as monomers adsorb at the interface, replacing surface water molecules with less strongly interacting species. This alters the balance of chemical potentials between the bulk and surface phases, driving further adsorption until the interface becomes saturated. It is a common misconception that at the CMC the surface becomes fully saturated, thus causing the onset of micelle formation in the bulk, and therefore a plateau in the surface tension. However, it is more accurate to say that above the CMC, the chemical potential hardly varies leading to minimal changes at the surface and thus a plateau in the surface tension occurs.

Graphically, this is shown as a plot of surface tension versus log(surfactant concentration), where the curve shows a characteristic decrease in surface tension with increasing concentration, followed by a plateau beyond the CMC (Figure 3a). The CMC is indicated by the inflection point on the curve, marking the onset of micelle formation in bulk solution.

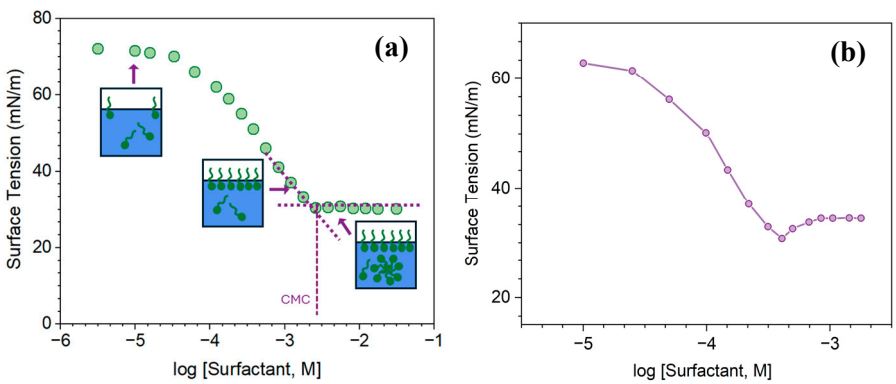

Figure 3: Surface tension as a function of the logarithm of the surfactant concentration for (a) a pure surfactant and (b) an impure surfactant.

Surface tension measurements are highly sensitive to the presence of surface-active impurities, which can significantly impact the isotherm shape and lead to uncertainties. The most common literature example is dodecanol contamination in SDS solutions[21–24], where even trace amounts of the highly surface active impurity

can lead to significant surface tension reductions in comparison to pure SDS. Due to the lower polarity of the dodecanol, it is preferentially adsorbed at the surface at low concentrations. However, once SDS reaches its CMC, such impurities can be solubilised within micelles, returning the surface tension back to that of pure SDS. This can lead to small dips in surface tension isotherms (Figure 3b) and uncertainties in parameters such as the CMC and are important to consider when interpreting data.

1.2.2 Conductivity

Another widely used method for determining the CMC of surfactants is electrical conductance. This method is only applicable to ionic surfactants, a distinct limitation in comparison to other CMC methods, but its simple and inexpensive setup still make it a common technique. Below the CMC, most ionic surfactant monomers behave as strong electrolytes in solution, contributing strongly to the conductivity as fully dissociated ions. Above the CMC, micelles form and as they are considerably larger and less mobile than the individual monomers and are partially ionized, the conductivity increases more slowly above the CMC, producing a distinct break in the conductivity-concentration curve.

The ratio of the conductivity gradients below and above the CMC can be used to estimate the degree of dissociation of the counterion i.e. the fraction that remain free in solution after micellisation. For Paper III, this is denoted using the parameter, β. While β is typically defined in literature as the fraction of bound counterions, the convention adopted for Paper III reflects consistency with previously published work.[25–27] However, for Paper I, the traditional notation for counterion dissociation, α, was used. This can also give an indication of how repulsive the headgroups of the surfactants in the micelle are. Highly charged, repulsive headgroups typically require more counterions close to the surface upon micellisation to screen the surface charge, resulting in lower degrees of dissociation (represented either by α or β) and sharper breakpoints in the conductivity curve.

While conductivity offers a simple and efficient method for determining CMC, it becomes less reliable in systems with small aggregation numbers, where the gradient change is subtle, leading to uncertainty in the CMC value[28]. Additionally, for anionic/non-ionic mixtures, the highly charged nature of the anionic surfactant can be shielded by the non-ionic presence rather than needing counterion condensation at the surface, leading to minimal changes in the gradient prior to- and above the CMC and a counterion dissociation parameter of ~1.

1.3 Surfactant and Micelle Structures

The shape of a micelle is an important parameter that determines many application properties such as their solubilisation capacity for oil and the viscosity of the overall formulation. The simplest model of micelles depicts them as spherical aggregates of surfactant monomers (Figure 1) and this approximation is often valid under dilute conditions. Surfactant behaviour can be tuned through structural modifications such as increasing the alkyl chain length, which generally lowers the CMC by enhancing hydrophobic interactions. However, longer alkyl chains also increases the Krafft temperature, reducing the solubility of the surfactant. As such, surfactant structure choice for commercial applications requires a careful balance between solubility and aggregation behaviour dependent on the desired properties of the formulation. Typically for commercial detergents, spherical micelles are preferential as these encapsulate hydrophobic material (e.g. dirt/oil) best.

A useful indicator for assessing the likely micelle morphology at low concentrations, based on the surfactant monomer structure, is the Critical Packing Parameter (CPP)[29], defined as:

$$CPP = \frac{V_H}{a_0 \cdot l_c} \tag{3}$$

where $\mathbf{V_H}$ is the volume of the hydrophilic tail (Å^3), $\mathbf{a_0}$ is the effective headgroup area (Å^2) and $\mathbf{l_c}$ is the maximum extended length of the hydrophobic tail (Å). The CPP provides a geometric interpretation of how molecular shape influences the preferred curvature of the surfactant aggregate. As illustrated in Figure 4, different ranges of the CPP are associated with distinct micellar morphologies.

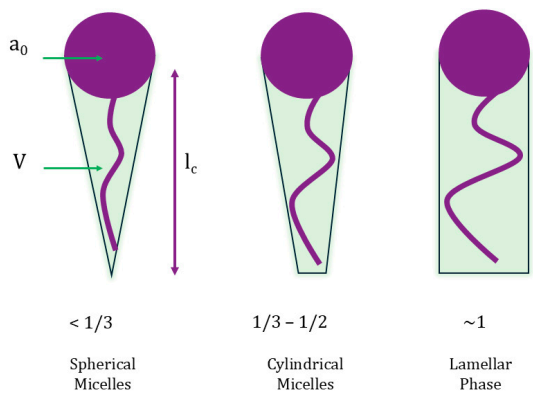

Figure 4: Schematic illustration of common critical packing parameters and their resulting micelle structures.[30]

The volume of the hydrophilic tail is commonly estimated using the Tanford formula[31], $V_H = 27.4 + 26.9n$ ($Å^3$), where n is the number of carbons in the alkyl chain and the fully extended length of the tail is represented using $l_c = 1.5 + 1.265n$ (Å). In contrast, determining a_0 is more complex and can be influenced by temperature, electrolyte concentration and pH.[32]

Most surfactants possess simple, linear single-chained hydrophobic tails between C_{10}-C_{16} in length. In the CPP calculation, the length and volume of the alkyl chain tend to counterbalance each other in the calculation, making the size, charge and structure of the headgroup the dominant factor influencing micellar curvature and morphology.

At low concentrations, ionic micelles typically exhibit aggregation numbers below 100[33,34] and non-ionics typically exhibit higher numbers.[32] This is largely due to electrostatic repulsion between the ionic charged headgroups limiting the number of monomers that can pack into a single micelle, unlike the non-ionics.

As surfactant concentration increases, micelles may elongate from spherical to more anisotropic morphologies such as cylindrical, rod like or wormlike structures. At even higher concentrations, these can further evolve into liquid crystal structures such as cubic, hexagonal or lamellar arrangements. These transitions are driven by a culmination of changes in intermolecular interactions, geometric arrangements and counterion binding, leading to ordered systems with the mobility of a liquid. These structures are important when it comes to rheological properties for a concentrated formulation, making phase diagrams for potential commercial surfactants

A simple and rapid method for identifying these phases is to examine samples under cross polarisers. Isotropic phases such as dilute micellar solutions or cubic phases appear dark because they do not alter the polarised light path. In contrast, anisotropic liquid crystalline phases, such as lamellar or hexagonal, exhibit birefringence, appearing bright due to their ordered, directionally dependent refractive indices. This visual distinction provides a useful first indication of phase structure. However, unambiguous identification of specific phases, particularly between lamellar and hexagonal arrangements, typically requires more sophisticated techniques such as small-angle X-ray scattering (SAXS), as discussed in further detail later.

1.4 Surfactant Adsorption at the Air-Water (A-W) Interface

Surfactant molecules adsorb at the air-water (A-W) interface to reduce the free energy of a surface; a property extensively utilised in product applications. The adsorption is primarily driven by the hydrophobic effect, which favours the removal of hydrophobic molecules from bulk water. Once at the interface, the amphiphilic

nature of surfactants leads to the orientation of hydrophilic headgroups into the aqueous phase and hydrophobic tails toward the air, forming a surface monolayer.

Adsorption at the air-water interface is fundamental to formulation behaviours such as foaming, wetting and emulsification and techniques utilised to study the phenomena provide sensitive insight into surfactant molecular geometry and headgroup interactions. As previously mentioned, the air-water interface has a high surface free energy, due to the presence of unbalanced hydrogen bonds in surface molecules. Surfactant adsorption replaces some of these water molecules with less strongly interacting species, thereby reducing the number of unbalanced bonds, lowering the surface free energy.

The additional amount of surfactant adsorbed per unit area at the air-water interface in comparison to its concentration in the bulk solution is described by the surface excess (Γ, in mmol/m^2). This can be estimated through utilisation of the Gibbs surface excess equation[35] :

$$\Gamma = -\frac{1}{2.303nRT}\left(\frac{\delta\gamma}{\delta \log C}\right) \tag{4.1}$$

Where **n** is the number of species influencing the surface tension (typically n = 2 for ionic surfactants, n = 1 for non-ionic), **R** is the ideal gas constant (8.314 J K^{-1} mol^{-1}), **T** is the temperature of the solution (K)**, γ** is the surface tension (mN m^{-1}) and **C** is the bulk molar concentration (M). The slope **(δγ/δlogC)** is obtained from the linear portion of a surface tension versus log(concentration) curve below the CMC. For surfactant monolayers, values for Γ typically range between 1-4 μmol/m^2 and is a key indication of how surfactants pack at an interface.

The Gibbs surface excess equation links measurable changes in surface tension to the interfacial concentration of surfactant molecules. Once Γ is known, the minimum area per molecule (APM, in Å^2) at the interface can be calculated through the relation:

$$APM = \frac{10^{20}}{N_a \cdot \Gamma} \tag{4.2}$$

Where $\mathbf{N_a}$ is Avogadro's Number (6.022 x 10^{23} mol^{-1}).

At full surface saturation, the surface and bulk solution are in dynamic equilibrium, where monomers continually exchange between the two pseudo-phases, and the chemical potentials can be considered equal.

Use of surface tension as a surface-sensitive technique comes with its limitations, especially when considering mixed surfactant systems. The technique offers only indirect information and cannot distinguish between different components, nor reveal molecular orientation or layer thickness. However, it remains a simple and accessible method that provides valuable insights and can be complementary to other, more advanced surface techniques such as neutron reflectometry.

1.5 Surfactant Choices

Before addressing mixed-surfactant systems, it is essential to first examine the behaviour of each surfactant individually. This section summarises key literature on the surfactants relevant to this study and outlines the rationale for their selection.

1.5.1 Currently used: Linear alkylbenzene sulfonate (LAS)

Linear alkylbenzene sulfonate (LAS) is currently the most widely used anionic surfactant in detergent formulations and its self-assembly behaviour has been extensively studied both alone[36–38] and in mixed systems.[39–41] Its unmatched performance[42], cost-effectiveness and commercial viability make it a critical reference point when developing novel alternatives. As such, LAS is the primary reference against which the behaviour of STFS is compared in this work.

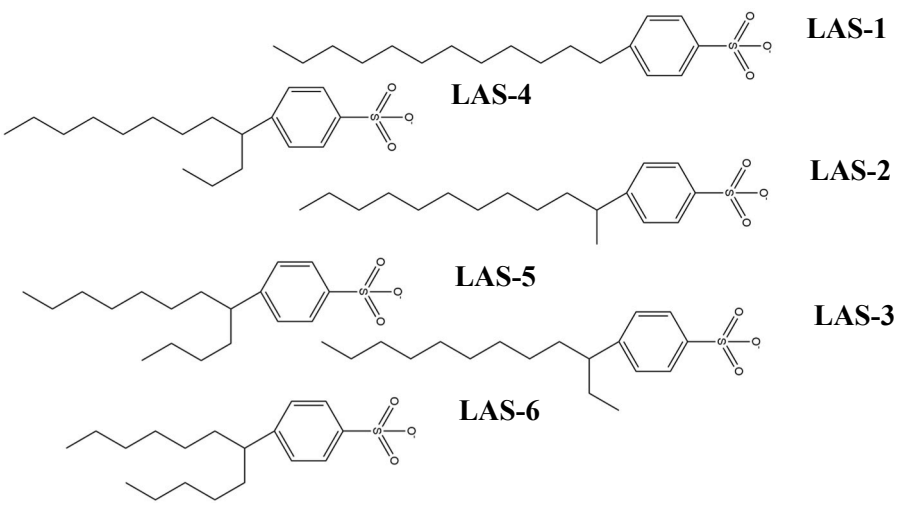

Figure 5: Structures of the various positional isomers of Linear Alkylbenzene Sulfonate (LAS-n, where n denotes the carbon position that the benzene sulfonate is attached at).

Commercial LAS consists of a complex mixture of $C_{10\text{-}14}$ alkyl chains, C_{12} being the most abundant, and different positional isomers for which the benzene ring is located at varying points along the hydrocarbon chain (Figure 5). This structural heterogeneity likely contributes to its effective cleaning efficacy but complicates analysis of self-assembly and its aggregation behaviour, with information on individual isomer properties being limited.[43–45]

Of the isomers, LAS-6 (phenyl ring on carbon 6) is both most water-soluble and most abundant at room temperature, while other isomers (e.g. LAS-1 to LAS-3) show stronger detergency but limited solubility.[43,45] Phase behaviour studies have shown that shifting the benzene ring position can significantly impact the surfactant micellar structure, viscosity and Krafft Point.[43]

To avoid the complexity of isomer mixtures, LAS-6 has often been the focus of many SANS studies[46–49], especially in mixtures with other surfactants. This allows clearer insight to accurately describe a system composition when only dealing with a singular isomer.

That being said, sodium dodecylbenzene sulfonate (SDBS), another name that may refer to LAS and typically represents all positional isomers, has also been extensively mentioned in literature.[50–52] SDBS micelles have been described as having sphero-cylindrical structures in dilute solution with semi minor axis lengths of ~22 Å that shortens with increasing temperature. [53] The limiting area per molecule for SDBS at the air-water interface has been shown to be 59 ± 3Å^2 using surface tension[54] and 61 Å^2 using molecular dynamic simulations.[55]

LAS remains a key ingredient in detergent formulations but its petrochemically based synthesis is not a sustainable option for the future. While some research is focused on looking into improved synthesis routes for LAS,[56,57] the easiest choice would be to swap it out in formulations with an alternative surfactant.

1.5.2 Surfactant of interest: Oleo-furan sulfonates (OFS)

Furan-based anionic surfactants have been proposed as attractive alternatives with the belief that the presence of an aromatic ring may be a key contributor to its performance. It has been theorised that a furan ring, derived from renewable sources, could serve a similar structural role as the benzene ring plays in LAS.

In particular, furan-based surfactants can be synthesised from bio-based platform chemicals such as 5-hydroxymethylfurfural (HMF) and its derivatives.[58,59] HMF is easily obtained from C6 sugars, which is a highly versatile precursor found abundantly in biomass, with an aldehyde and hydroxyl functional group present for chemical modifications. Furan, derived from biobased furfural, can also form surfactants through acylation with the anhydride of a fatty acid using zeolite catalysts before sulfonation, to yield oleo-furan sulfonates (OFS, Figure 6).[60]

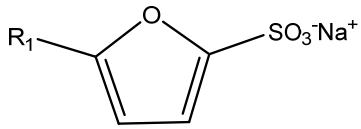

Figure 6: Generalised structure of OFS surfactants where R_1 represents an alkyl chain.

Studies of these oleo-furan sulfonates (OFS) have shown properties comparable to commercial LAS in relation to their wetting and foaming behaviour.[60] The CMC and Krafft temperature of the OFS can be tuned through choice of the hydrophobic chain length, branching of the chain and the presence of a carbonyl spacer between the ring and chain. Whilst the commercial LAS mixture exhibits better solubility and lower CMC values overall, in a direct comparison, the solubility of OFS-12 (Figure 6, where R_1 is a dodecyl tail) is much better than that of LAS-1 (the 1 positional isomer of LAS), based on their Krafft temperatures (30 °C vs 52 °C respectively).[60]

The most significant advantage OFS surfactants have over traditional surfactants such as LAS or SDS is their superior resistance to hard water[60]. Hard water, containing high concentrations of divalent ions e.g. Mg^{2+} and Ca^{2+}, can form insoluble precipitates with traditional anionic surfactants, reducing the effectiveness of the detergent. While conventional formulations rely on, chelating agents to counteract this issue, eliminating the need for additional components in a formulation has both environmental and cost benefits.

Despite these promising attributes, the majority of literature to date has focused on the synthesis and structural modification of OFS surfactants, with comparatively little attention paid to their self-assembly, interfacial behaviour or performance in mixed systems. This work therefore seeks to address these gaps with the focus on one OFS surfactant in detail – sodium tetradecyl furan sulfonate (STFS). Further background information on STFS has been provided in Paper I and Paper II.

1.5.3 Conventional anionic: Sodium Dodecyl Sulfate (SDS)

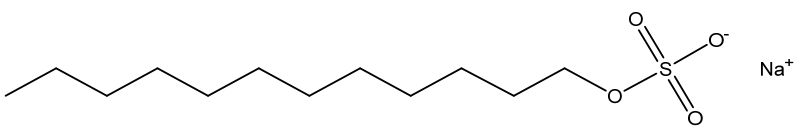

Figure 7: Molecular structure of SDS.

SDS (Figure 7) is one of the most widely used anionic surfactants and was selected for this work as a well-established surfactant to mix with STFS in binary and ternary

systems. Due to its versatility, SDS is incorporated into a broad range of commercial products, including toothpaste, shampoo and laundry detergents. Its simple chemical structure, a C_{12} alkyl chain attached to a sulfate headgroup, combined with cost-effective synthesis has made it the model anionic surfactant in both fundamental and applied research.[61–63]

In aqueous solutions, the dodecyl sulfate anion is most typically associated with a sodium (Na^+) counterion, although the effects of counterion variation on both the self assembly[64] and adsorption at the A-W interface[65,66] have also been explored.

The CMC of SDS in water at room temperature is commonly reported to be ~8.2 mM with micelle radii of ~23.2 Å and aggregation numbers of ~77.[67] While some variability exists across techniques, SDS is known to exhibit a non-monotonic temperature dependence with a CMC minima around 25°C before an increase at higher temperatures.[68] This is relevant to the present work, which employed SDS at elevated temperatures (45-50 °C).

With increasing concentration, SDS is known to transition from spherical micelles to more elongated ellipsoidal or cylindrical micelles.[69] Within this body of work however, solutions are extremely dilute so no elongation of micelles is expected.

At the air-water interface, SDS has a well-characterised surface packing. Literature reports an area per molecule of ~47.4 $Å^2$ at 25 °C using surface tension, increasing slightly to ~50 $Å^2$ at 40 °C.[70] Neutron reflectivity data for the same samples indicate a slightly smaller area per molecule of ~44 $Å^2$ at 25 °C.

1.5.4 Conventional non-ionic: Hexaethylene glycol monododecyl ether ($C_{12}E_6$)

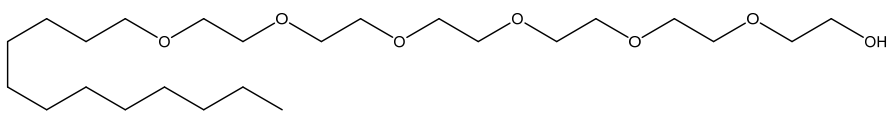

Figure 8: Molecular structure of $C_{12}E_6$.

$C_{12}E_6$ (Figure 8) is a non-ionic surfactant from the polyoxyethlene ether family, denoted by the C_nE_m notation, where *n* represents the alkyl tail length (C_{12}, dodecyl in this case) and *m* indicates the number of ethylene oxide (EO) units in the headgroup before the hydroxide end group (E_6, hexaethylene). $C_{12}E_6$ was chosen as the non-ionic species for this research due to the moderate length of its ethylene oxide chain and the extensive body of literature available.[71–75]

The CMC of the C_nE_m family can be predictably modulated through structural changes to influence the hydrophobic-hydrophilic balance. Increasing the alkyl tail

length reduces the CMC, whilst increasing the ethylene oxide headgroup length raises it. Due to its non-ionic nature, literature CMC values for $C_{12}E_6$ are very low, ranging between 0.060-0.087 mM.[32,76,77] Like many non-ionic surfactants, the CMC of $C_{12}E_6$ exhibits a non-monotonic temperature dependence, which is particularly relevant in this work as some measurements were performed near its reported cloud point (~48 °C).[78] This is the temperature at which the solution becomes turbid due to phase separation caused by dehydration of the ethylene oxide headgroups at elevated temperatures.

Non-ionic surfactants like $C_{12}E_6$ are widely used in formulations to reduce CMC, increase solubility of a mixture and improve tolerance to external changes such as pH and electrolyte addition. Although electrolyte addition can lower the CMC of non-ionic surfactants, the effect is typically less pronounced than with ionic surfactants.[32]

At dilute concentrations just above the CMC, $C_{12}E_6$ forms spherical micelles but with increasing temperature or concentration, these micelles elongate and transition to cylindrical or wormlike micelles.[78] SANS studies have characterised these micelles in dilute solution as polydisperse spheres with a radius between 27.0-28.5Å over a temperature range.[79] Dynamic light scattering (DLS) and static light scattering (SLS) studies of the C_iE_j surfactant family found that increasing temperature typically led to an increase in aggregation number and micelle size, reflecting the dehydration of the ethylene oxide chains, a behaviour also visualised using molecular dynamics for $C_{12}E_6$.[80]

At the air-water interface, $C_{12}E_6$ forms a stable monolayer with a reported area per molecule of 55 ± 3 $Å^2$ at room temperature, decreasing slightly when temperature is increased to 46 °C, as determined by neutron reflectometry.[81,82] This value serves as a useful reference for evaluating changes in interfacial packing upon mixing surfactants.

1.6 Surfactant Mixtures

Surfactants are rarely used individually in commercial formulations, either inadvertently due to inherent polydispersity of surfactants, having multiple isomers and chain lengths, or purposefully to provide a benefit to the formulation. Instead, a combination of different surfactant types can result in enhanced or tuneable properties. For example, anionic surfactants may be added for increased foaming in laundry detergents or strong adsorption for heavy duty cleaning products while non-ionic surfactants are commonly included to lower the CMC and because they have a superior wetting ability.

When mixed components are structurally very similar (i.e. two non-ionic surfactants with slightly differing chain lengths), ideal mixing can occur as all intermolecular interactions are equal. In these cases, the CMC of the mixed system is simply the weighted sum of the individual CMCs based on the molar ratios in the bulk. This is described by Clint's equation[83] such that:

$$\frac{1}{CMC_{12}} = \frac{\alpha_1}{CMC_1} + \frac{\alpha_2}{CMC_2} \tag{5.1}$$

where $\boldsymbol{\alpha_1}$ and $\boldsymbol{\alpha_2}$ are the solution molar ratios of each surfactant and $\mathbf{CMC}_1$, $\mathbf{CMC_2}$ and $\mathbf{CMC_{12}}$ are the individual and mixed system CMCs respectively. This equation can also be extended to ternary and multicomponent systems.

However, surfactants rarely mix ideally, and the behaviour of mixtures is then dependent on two main factors: the relative surface activities of each component (related to their CMC values and accounted for in ideal mixing), and the interactions between the two components. These factors lead to non-linear behaviour in mixed CMC or surface tension values, which cannot be captured by Clint's equation alone

Surfactant mixing has been heavily studied[48,84–87], with most non-ideal mixing being modelled using regular solution theory (RST), applied within the pseudo-phase framework introduced earlier. RST accounts for deviations from ideality using activity coefficients, $\mathbf{f_1}$ and $\mathbf{f_2}$, of the two surfactants, modifying Equation 6 to give the non-ideal mixing equation:

$$\frac{1}{C_{12}} = \frac{X_1}{f_1 C_1} + \frac{X_2}{f_2 C_2} \tag{5.2}$$

where $\mathbf{X_1}$ represents the mole fraction of surfactant 1 within the micelle or at the surface. When discussing interactions and mixtures in the bulk micellar solution, $\mathbf{C_1}$, $\mathbf{C_2}$ and $\mathbf{C_{12}}$ represent the CMC of the individual and mixed surfactants respectively. However, when discussing surface compositions, $\mathbf{C_1}$, $\mathbf{C_2}$ and $\mathbf{C_{12}}$ represent the concentration of the individual and mixed surfactants respectively that is required to reduce the surface tension to a chosen value.

The activity coefficients can be described using a singular interaction parameter, $\boldsymbol{\beta}$:

$$ln f_1 = \beta(1 - X_1)^2 \tag{5.3a}$$

$$ln f_2 = \beta {X_1}^2 \tag{5.3b}$$

and these equations can be combined and X_1 solved iteratively using:

$$\frac{(X_1)^2\ ln\ (\propto_1 C_{12}/C_1X_1)}{(1-X_1)^2\ ln\ [\propto_2 C_{12}/C_2(1-X_1)]} = 1 \tag{5.4}$$

and the β parameter is calculated using:

$$\beta = \frac{ln(\alpha_1 C_{12}/X_1 C_1)}{(1-X_1)^2} \tag{5.5}$$

The interaction parameter, β, can be used to quantify the nature of interactions due to mixing, with one value (β_S) describing adsorption at the interface and another (β_M) describing aggregation in the bulk. Though calculated using the same equations, they refer to distinct pseudo-phases and are not directly interchangeable. A negative β is indicative of synergistic interactions, with favourable mixing and lower CMC values than ideal mixing would predict. A positive β in turn signals unfavourable mixing, which is typically uncommon and is likely due to strong electrostatic repulsions. Most surfactant mixtures have a negative interaction parameter with anionic/cationic mixtures having characteristically the strongest electrostatic attractions and thus highly negative interaction parameters (β < -10). Ionic/non-ionic mixtures typically have negative values but not as strong as anionic/cationic mixtures. The more similar the surfactant structures, the closer to ideal mixing a system typically is.

There are alternative approaches to RST for describing the non ideality of mixed surfactant systems including Nagarajan with a molecular thermodynamics approach[88,89] and the mass action model90 but the simplicity and overall applicability of RST has led to it being the main thermodynamic approach used to analyse mixed surfactant systems.

RST does have limitations as a theory for adsorbed mixed surfactant monolayers, as it makes the assumption that the entire layer is comprised only of surfactant molecules, neglecting to model the effect of the inclusion of water molecules that are almost certainly in the surface layer. It is also only applicable for mixtures where X_1 falls between 0.2-0.8 for both micelles and surface, failing to accurately describe extreme compositions.

1.7 Relevance to Formulation and Detergency

While substituting an alternative bioderived surfactant into a formulation may seem simple, retaining the effective cleaning properties of commercial species like LAS is more complex. Biosurfactants, such as rhamnolipids[91,92] and sophorolipids[93,94] have presented as advantageous and promising alternatives over the past ten years. However, the high production costs and difficult purification methods limits their viability on an industrial scale as a full replacement to petrochemical-derived surfactants.

A more realistic transitional approach involves mixed surfactant system, combining bio-derived surfactants and conventional surfactants. Studies of such systems are crucial, as partial substitution is likely be the first step in reducing the reliance on petrochemical-derived surfactants in commercial formulations.

Designing effective formulations requires detailed knowledge of how molecular features, such as chain length and headgroup interactions, can influence key properties such as self-assembly and adsorption behaviour. These considerations become more complex in multicomponent systems, where competitive and cooperative adsorption mechanisms may operate simultaneously. Is one surfactant dominant in the mixtures? Is there overall synergism?

A key measure of detergency is the ability of a micelle to solubilise oily hydrophobic solutes. This capacity can be quantified using the maximum additive concentration (MAC), utilised in Paper III, which represents the saturated solubilization capability of a given solute within a micellar solution. Previous studies have used UV-Vis to track the solubilisation of hydrophobic perfume molecules to determine the maximum capacity that the micelles could encapsulate, useful for formulations[95–98]. We have extended its use to small hydrophobic molecules such as cyclohexane. Typically, the MAC is identified from the inflection point in a plot of solution absorbance versus incremental hydrophobic solute addition (as a model “dirt”) to a solution of known surfactant concentration, corresponding to the onset of turbidity as micelles become saturated. This allows us to directly compare the capabilities of two surfactants of similar structure.

2 Scattering Techniques

Scattering techniques are a powerful tool used to probe the nanoscale structure of materials, accessing length scales in the angstrom to nanometre range. The wavelength of the radiation sets the length scale that can be measured. In this work, both X-rays and neutrons are employed for probing the surfactant self-assembly behaviour.

A typical scattering set up includes a collimated beam of radiation (either X-rays or neutrons for this research) directed at a sample of thickness *d*. The incoming radiation has a defined wavelength (λ) and energy (E). While most of the radiation is transmitted or absorbed by the sample, a small fraction that interacts with the sample and is scattered at an angle different to that of the incident angle (See Figure 9).

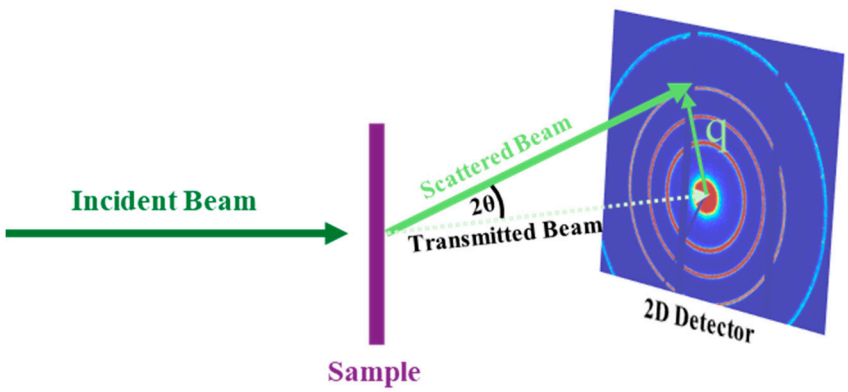

Figure 9: Schematic diagram of a small-angle scattering setup.

It is this scattered intensity that is measured and analysed to provide structural as well as spatial information about the material. The scattered intensity is recorded as a function of the scattering angle and converted into a function of the scattering vector, q, defined as:

$$q = \frac{4\pi}{\lambda}\sin\theta \tag{6}$$

where $\boldsymbol{\lambda}$ is the wavelength of the incident radiation and $2\boldsymbol{\theta}$ is the scattering angle. In most structural studies, elastic scattering is assumed, meaning there is no significant energy transfer between the incident beam and the sample, so the energy of the incident and scattered radiation is conserved, and only the direction is altered.

A key experimental consideration for all scattering experiments is that the measured signal contains a contribution from background scattering. This includes incoherent and inelastic scattering from the sample as well as contributions from the sample environment and instrument components such as air, cell windows, slits and detector housings. For neutron studies, the inelastic scattering, often arises from hydrogen-rich materials, and can elevate the background and reduce contrast. For total neutron scattering, background treatment is particularly important due to the wide Q-range and data reduction workflow attempts to subtract inelastic and instrumental background contributions to ensure modelling of the scattering data is accurate.

This section presents a brief overview of the scattering techniques used in this work but more extensive descriptions can be found in various review papers and books[99–101].

2.1 Small-Angle Scattering

Small-angle scattering (SAS), which includes both small-angle X-ray scattering (SAXS) and small-angle neutron scattering (SANS), focuses on scattering at low q values (typically 0.01-1 $Å^{-1}$) corresponding to real-space structures on the order of 1-100 nm. These techniques probe the forward-scattered radiation and are well suited for non-invasive, *in situ* studies of soft matter systems like micelles, polymers and colloids. This scattering results in an intensity versus q profile which can be interpreted through models that describe both the particle size/shape (form factor, P(q)) and interactions between particles (structure factor, S(q)).

In systems of charged micelles or with high polydispersity, traditional model-free approaches such as Guinier or Porod analysis may not yield reliable structural parameters, due to overlapping contributions from particle shape and interparticle interactions. Therefore, model-based fitting was employed throughout this work, allowing quantitative parameters to be extracted.

Fitting theoretical models against experimental data was performed using a least-squares method, minimizing the reduced chi-squared value to evaluate the quality of the fit. Multiple common micelle models were trialled in combination with relevant assumptions to best capture the structure and behaviour of the systems studied.

The intensity of scattering is proportional to the square of the difference in scattering length density (SLD, ρ) between an object and its surroundings, typically referred

to as the “contrast”. This makes the SLD essentially a measure of how strongly a material scatters and can be given by:

$$\rho = \frac{\sum n_i b_i}{V} \tag{7}$$

where $\mathbf{n_i}$ and $\mathbf{b_i}$ are the number and coherent scattering length (for either X-ray or neutron) of atom ***i*** respectively and **V** is the molecular volume.

2.2 Small-Angle X-Ray Scattering (SAXS)

SAXS relies on differences in electron density between the background and scattering bodies to generate scattering contrast, making it especially useful for systems where components differ significantly in atomic number. In aqueous surfactant solutions, however, the electron density contrast between micelles and water is often low, which leads to weak scattering signals. Additionally, just above the CMC, the number of micelles in the system may be sparsely distributed, leading to signals that are not representative of the bulk solution. Consequently, SAXS data alone cannot definitively resolve dilute micellar architecture without assumptions and complementary data to form a full structural analysis.[102]

In contrast, for highly concentrated surfactant solutions, SAXS is a powerful tool for identifying liquid crystalline phases formed. These phases give rise to distinct Bragg peaks corresponding to the long-range ordering of the surfactant molecules. Braggs law is used to relate the scattering vector to the interplanar distance:

$$d = \frac{2\pi}{q_{peak}} \tag{8}$$

where $\mathbf{q_{peak}}$ indicates the distance (d) between the aligned particles. The relative distances of these Bragg peaks on the q scale are indicative of the liquid crystal structure. For example, a lamellar phase yields q_{peak} with a ratio of distances of 1, 2, 3, 4 etc. whilst a hexagonal phase would have ratios of 1, √3, 2, √7 etc.

2.3 Small-Angle Neutron Scattering (SANS)

Whilst SAXS can be a useful technique to give structures, shapes and size information about a system, SANS offers a distinct advantage for studying micellar systems. In neutron scattering, contrast arises from differences in SLD, dependent on the atomic nuclei. Notably, the coherent scattering lengths of hydrogen and deuterium vary greatly (-3.741 x10^{-5} Å for ^{1}H versus 6.671 x10^{-5} Å for ^{2}D) enabling selective contrast variation by replacing hydrogen atoms with deuterium in specific parts of a molecule such as the surfactants alkyl tail. Using D_2O instead of H_2O as a solvent also helps to reduce the incoherent background contribution from ^{1}H.

The measured intensity in a SANS experiment can be expressed as:

$$I(\lambda,\theta) = I_0(\lambda)\Delta\Omega\eta(\lambda)T(\lambda)V\frac{\delta\Sigma}{\delta\Omega}(Q) \tag{9.1}$$

where $\mathbf{I_0}$ is the incident flux, $\mathbf{\Delta\Omega}$ is the solid angle element and $\boldsymbol{\eta}$ is the detector efficiency, parameters that are all instrument specific and which do not vary between samples for a given instrument set-up. **T** is the sample transmission, **V** is the sample volume and $\mathbf{\delta\Sigma/\delta\Omega(Q)}$ is the differential scattering cross section, which is a quantitative formulation of the interaction of the radiation with the sample.

This differential scattering cross-section can be defined as:

$$\frac{\delta\Sigma}{\delta\Omega}(Q) = N_p V_p^2 (\Delta\rho)^2 P(Q) S(Q) + B_{back} \tag{9.2}$$

and this parameter contains all the information about the sample. $\mathbf{N_p}$ is the number concentration of the scattering bodies, $\mathbf{V_p}$ is the volume of one scattering particle, $\mathbf{\Delta\rho}$ is the difference in scattering length density between the particle and solvent. P(Q) is the form factor and S(Q) is the structure factor and B_{back} is the background scattering from incoherent scattering.

The form factor, P(Q), is used to model the shape and size of a particle. For this work, a core-shell model was employed for all micelles, using either a prolate ellipsoidal model[103] or polydisperse sphere model[104]. These models are appropriate for surfactant micelles, which typically exhibit distinct SLD contrast between their hydrophobic core (alkyl chains) and hydrophilic shell (headgroups and associated hydration layer). The P(Q), in this case incorporates the SLD term seen in equation 9.2 above, to account for the contrast for between these regions. The core-shell sphere form factor is defined as:

$$P(q) = \frac{3}{V_s}\left[V_c(\rho_c - \rho_s)\frac{\sin(qr_c) - qr_c\cos(qr_c)}{(qr_c)^3} + V_s(\rho_s - \rho_{solvent})\frac{\sin(qr_s) - qr_s\cos(qr_s)}{(qr_s)^3}\right]^2 \quad (9.3)$$

where $\mathbf{r_c}$ represents the core radius, assumed to contain only the alkyl hydrocarbon chains of the surfactants, with a theoretical limiting value of the length of a fully extended chain calculated using the Tanford formula[31], $l_c = 1.265n_c + 1.50$ as previously discussed. $\mathbf{r_s}$ represents the total micelle radius which includes the alkyl core radius plus the polar shell thickness, consisting of the hydrophilic shell groups and a certain degree of hydration. $\boldsymbol{\rho_c}$ and $\boldsymbol{\rho_s}$ are the scattering length densities of the core and shell respectively. $\mathbf{V_c}$ and $\mathbf{V_s}$ are the micellar core and total micelle volume respectively and can be calculated using the volume of a sphere, $V = (4\pi/3)\cdot r_x^3$ where $\mathbf{r_x}$ is either the core radius, $\mathbf{r_c}$, or the total micelle radius $\mathbf{r_s}$. The form factor is normalised by the average particle volume and convoluted with a Schulz distribution to represent the polydisperse nature of the system.

The structure factor, S(Q), is used to model the interparticle interactions. For charged micelles (or spheres), the most common structure factor used to model interactions is the Hayter-Penfold structure factor, based on the rescaled mean sphere approximation (RMSA) and a screened Coulomb potential. This structure factor takes into account the volume fraction of the particles (V_f), the effective surface charge of the particle (z), the concentration of additional electrolyte in the system and the dielectric constant of the medium (water, ε ~78 at 25 °C). The structure factor becomes equal to one with infinite dilution of the particles, indicating no interaction. High electrolyte presence can also reduce the structure factor contribution through shielding of the repulsions between the charged particles. In some studies, electrolytes are deliberately added to isolate the form factor contribution[85,105]. For this study however, it was decided to study the surfactants in pure water, without alteration first, before possible progression towards investigating the effect electrolytes may have.

Figure 10 displays how the combination of the polydisperse core-shell form factor (Fig. 10a) and the Hayter Penfold structure factor (Fig. 10b) leads to an overall scattering pattern (Fig. 10c).

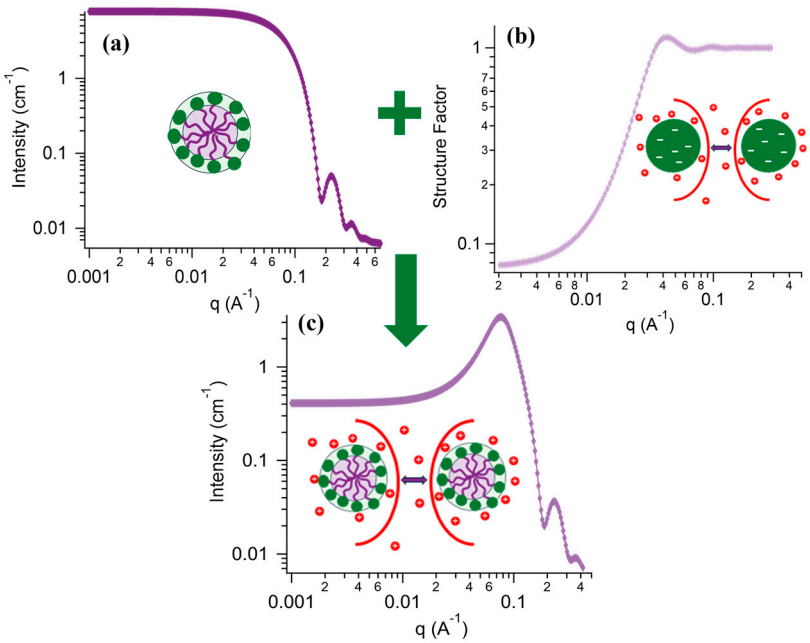

Figure 10: Breakdown of the main SANS model used to fit the experimental data in this model. (a) P(Q) contribution from a polydisperse core-shell model, highlighting the micelle internal structure (b) S(Q) calculated using the Hayter-Penfold model to account for interparticle interactions (c) Full model representing total scattering intensity.

There are two main types of neutron sources used for SANS:

Steady state SANS instruments rely on continuous neutron production via nuclear fission in a research reactor (e.g. ILL). The neutrons are moderated (cooled) and transported through neutron guides to minimise intensity loss to the beamline. The sources typically use monochromatic beams, where a narrow wavelength band is selected using a velocity selector. To access a broad *q*-range, measurements are usually taken using multiple sample-detector distances and the resulting data are stitched together. However, some reactor-based instruments can perform time-of-flight (TOF) measurements if a broad wavelength band is used. In these cases, choppers are employed to define the start and end of a neutron pulse, enabling wavelength resolution via TOF, even at a continuous source.

Time of Flight (TOF) SANS at pulsed spallation sources (e.g. ISIS) generates short bursts of neutrons by irradiation of a heavy element target with a high energy proton beam. The neutron beam is not monochromatized meaning that neutrons with a shorter wavelength travel faster, reaching the detector sooner than those with longer wavelengths. This means a wide q-range can be covered using a single sample-detector-distance. Only TOF SANS was used in the research of this thesis.

2.4 Neutron Reflectometry

Neutron reflectometry (NR) is a powerful, non-destructive technique for probing the structure of surfaces and interfaces at the nanometre scale. While the total reflection of neutrons was first observed by Fermi and Zinn in the 1940s[106], the rising popularity of NR as a surface sensitive technique did not gain prominence until the 1980s. It is exceptionally well-suited for studying soft matter systems, including polymer thin films[107], lipid membranes[108] and, most relevant to this thesis, surfactant monolayers at the air-water interface[109].

In an NR experiment, a highly collimated neutron beam is directed at a flat interface at a grazing angle of incidence, θ_i. For specular reflection, where angle of incidence is equal to angle of reflection ($\theta_i = \theta_r$), the measurement is sensitive to the average composition profile in the direction normal to the interface (z plane). This provides a one-dimensional structural map of the interface (Figure 11). The reflectivity signal is measured as a function of the momentum transfer vector, Q_z, which is defined by the experimental geometry:

$$Q_z = \frac{4\pi}{\lambda} sin\theta_i \tag{10.1}$$

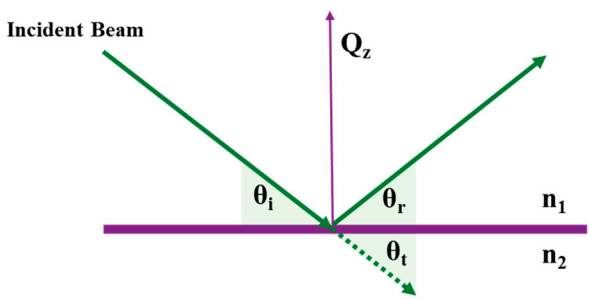

Figure 11: Simple model of reflectivity across two media with varying refractive indices (n).

The reflectivity is proportional to the square of the Fourier transform of the SLD profile, highlighting the direct relationship between the measured reflectometry data and the interfacial structure. The reflectivity, R, related to the momentum transfer in the z plane Q_z, can be written as:

$$R(Q_z) \approx \frac{16\pi^2}{{Q_z}^4} \left| \int_{-\infty}^{+\infty} \rho(z) exp^{(izQ_z)} dz \right|^2 \tag{10.2}$$

where ***ρ(z)*** is the scattering length density. This also demonstrates how the reflectivity curve is highly Q^4 dependent, so signal is lost into the background quickly.

Modelling the reflectivity profile

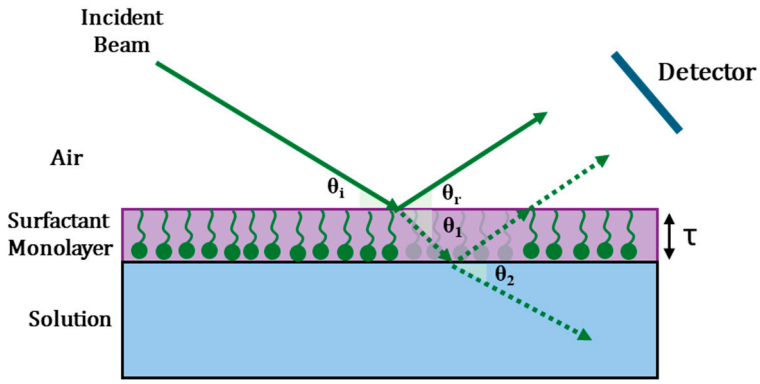

Figure 12: Schematic illustration of specular neutron reflectometry of a surfactant monolayer at the air-water interface, showing reflection and transmission of a neutron beam through a stratified medium.

Since NR does not produce a direct image, the experimental reflectivity profile $R(Q_z)$ can be analysed through fitting with a structural mode to determine the interfacial structure. The standard approach is to represent the interface as a series of discrete layers (a "slab model"), each defined by its own thickness **(τ)**, scattering length density **(ρ)** and interfacial roughness **(σ)**.

Theoretical reflectivity for a multilayer system can be modelled using the Abelès optical matrix formalism[110]. The incident neutron beam is refracted by each layer in varying amounts, as shown in Figure 12, and this method computes a characteristic matrix for each layer and multiplies them together to find the properties of the entire system. A fitting algorithm then systematically varies the model parameters (τ, ρ, σ for each layer) to minimise the differences between the theoretical reflectivity curve and the measured experimental data, typically by minimising the chi-squared, χ^2, the sum of squares of the weighted deviations.

The simplest system would be a clean air-water interface (Figure 11) where the only parameters to consider would be the SLD_{air}, $SLD_{solvent}$ and one surface roughness (typically ~3Å due to capillary waves and slight misalignment of packing), as well as a scale factor and background parameter. When there is an adsorbed uniform layer at the surface, for example a surfactant monolayer, the model can be extended using additional parameters such as the thickness (τ_i), SLD (ρ_i), hydration of the layer and a second roughness (σ_i) between the layer and the aqueous subphase.

Though this approach is an approximation rather than an exact model, it describes these types of systems well and allows for accurate fits to the experimental data. In this thesis, all NR datasets were analysed by fitting multiple contrast conditions, using χ^2 minimisation to identify optimal model parameters that consistently describe the system.

Application to surfactant systems

Most literature describes mixed surfactant adsorption as a single slab model due to simplicity and a lack of contrast between the head and tail regions.[48,93,111] This is particularly necessary when no deuteration is employed in specific parts of the molecule and to avoid over-parameterising the model.

Campbell *et al.*[112] presented how different theoretical models (i.e. one slab, two slab and roughness effect) of the same datasets could yield significantly different structural parameters, dependent on what was fitted and what was kept fixed to match molecular constraints. It was shown for surfactants (SDS and CTAB) that a two-layer model was possible for single surfactant systems when multiple isotopic contrasts were available to constrain the model. However, when dealing with mixed surfactant systems, the SLD of the adsorbed layer becomes a compositionally weighted parameter, which introduces additional complexity and correlation between fitted variables such as thickness and SLD. As a result, attempts to apply a two-slab models become over-parameterised and less reliable.

For these reasons, and to remain consistent with previous literature, the NR data in Paper II was modelled as a single-slab monolayer to represent the mixed surfactant film at the air-water interface.

For an adsorbed mixed surfactant monolayer, the fitted scattering length density, $\boldsymbol{\rho(z)}$, and layer thickness $\boldsymbol{(\tau)}$ can be used to extract parameters using the relation:

$$\rho(z) * \tau = \sum \frac{\Sigma\, b_n}{APM_n} \tag{11.1}$$

where $\mathbf{b_n}$ and $\mathbf{APM_n}$ are the coherent scattering lengths and the area per molecule for each surfactant, n, in the mixture respectively. The parameters ρ and τ inversely compensate each other during fitting so treating them as a combined parameter ($\rho\tau$) reduces the error compared to fitting the individual parameters. The total surface excess, $\boldsymbol{\Gamma_{tot}}$, is then calculated using:

$$\Gamma_{tot} = \frac{10^{\,20}}{N_A\, APM_{tot}} \tag{11.2}$$

where $\mathbf{N_A}$ represents Avogadro's constant (6.022×10^{23} mol^{-1}) to convert units from $Å^2$ per molecule to mol m^{-2}, and $\mathbf{APM_{tot}}$ is the total area per molecule for the surface (in $Å^2$). Further details on how parameters such as Γ and APM were calculated from the fitted reflectivity curves and extended to the binary mixed systems is given in Paper II.

2.5 Total Neutron Scattering

Total neutron scattering, sometimes referred to as neutron diffraction, is a powerful technique that considers a wide Q-range which can contain information about short-range atom interactions as well as more long-range interparticle interactions. Unlike traditional diffraction, which focuses on Bragg scattering and the long-range crystalline order it implies, total scattering includes both Bragg and diffuse scattering components. The latter arise from local structural deviations and short-range atom correlations that are not captured in average crystallographic models. This makes total neutron scattering particularly useful for characterising disordered systems, amorphous materials or liquids where such local structure is significant and the material is lacking long-range order.

Whereas SANS focuses on low Q regions (typically $Q < 0.5$ $Å^{-1}$) to study large-scale structures, total neutron scattering captures the full scattering pattern across a wide Q range (0.1-50 $Å^{-1}$). This broad Q coverage enables the recovery of real-space structural information via Fourier transformation of the structure factor, S(Q), yielding the radial distribution functions, g(r) of two atoms (a and b) which can be described in a general form as:

$$g_{ab}(r) = \frac{N_b}{4\pi r^2 \cdot dr \cdot \rho_b} \tag{12.1}$$

where $\mathbf{N_b}$ is the number of atoms of type b in a spherical shell of thickness **dr** at distance **r**, and $\boldsymbol{\rho_b}$ is the bulk density of b-atoms. At large r values, where atomic correlations vanish, g(r) approaches 1, indicating a random distribution at infinite dilution.

To obtain meaningful structural data, high instrumental precision is required. Experimental setup is similar to that used in neutron powder diffraction but must be capable of collecting data over a wide Q range with high signal-to-noise ratios. This is essential for resolving weak diffuse features that are often overshadowed by Bragg peaks or background scattering. Accurate correction for artifacts (i.e. background noise, incoherent scattering[113], absorption and contributions from the sample container) is also critical.

These corrections are typically applied during data reduction using software such as *Gudrun*[114]. In this workflow, input parameters such as the sample composition, bulk density and the thickness and material of the sample container are used to correct for multiple scattering and absorption effects. The end result is a reliable total scattering structure factor, S(Q), from which the pair distribution function g(r) can be obtained and used for detailed structural analysis. In many cases, g(r) serves as an input for further modelling using methods such as Empirical Potential Structure Refinement (EPSR), which allows us to build 3D atomistic models consistent with both the scattering data and known physical constraints.

2.6 Empirical Potential Structure Refinement (EPSR)

EPSR is a reverse Monte Carlo-like refinement technique developed by Soper[115] that allows us to model disordered systems at an atomistic level. The method uses an initial simulation model before the additional constraint of refining the simulation against neutron diffraction experimental data, instead of relying fully on predefined force fields.

Within EPSR, the simulation explores configurational space using trial moves. There are four types of trial moves – molecule translations, molecule rotations, molecular side chain rotations and individual atom movements. A move is defined as a small random change in the xyz coordinates or an arbitrary rotation around a random axis. Each move is then accepted or rejected based on the change of the total potential energy of the system, weighted with a Boltzmann factor, where the energy difference is defined as:

$$\delta U = U_{new} - U_{old} \tag{12.2}$$

If δU is larger than 0, the move is rejected. If the reverse is true, a random number ξ is computed and the Boltzmann factor check performed. The trial move is only accepted if $\xi < e^{-\beta\delta U}$, otherwise the move is rejected. Here, $\beta = 1/(k_B T)$ where T is the temperature and k_B the Boltzmann constant.

The total potential energy, U, is made up of two main terms: the reference potential energy, U_{ref}, and the empirical potential energy, U_{ep}. U_{ref} includes both intramolecular terms, such as bond stretching, angle bending and torsion potentials, as well as intermolecular terms. The intermolecular reference potential between atoms is derived from Lennard-Jones potentials and the effective Coulombic charges to give:

$$U_{\alpha\beta}^{ref}(r_{ij}) = 4\epsilon_{\alpha\beta}\left[\left(\frac{\sigma_{\alpha\beta}}{r_{ij}}\right)^{12} - \left(\frac{\sigma_{\alpha\beta}}{r_{ij}}\right)^{6}\right] + \frac{q_\alpha q_\beta}{4\pi\epsilon_0 r_{ij}} \qquad (12.3)$$

where **αβ** describe the types of atoms i and j respectively, $\epsilon_{\alpha\beta}$ is the depth of the potential well, $\sigma_{\alpha\beta}$ is the distance at which the interatomic potential is zero and q_α, q_β are the point charge values of α and β.

After equilibration under U_{ref} (Figure 13a), the U_{ep} is introduced incrementally to guide the atomic and molecular movements towards a structure that more closely matches the experimental diffraction data (Figure 13b). This approach allows the model to retain molecular realism while better capturing the local structure observed in experiments. While micelle formation is a spontaneous and rapid process in real systems, this process in EPSR takes a long time due to the large amount of localised trial moves needed for the surfactants to approach each other in an energetically favoured way, making large-scale cooperative assembly inherently slow.

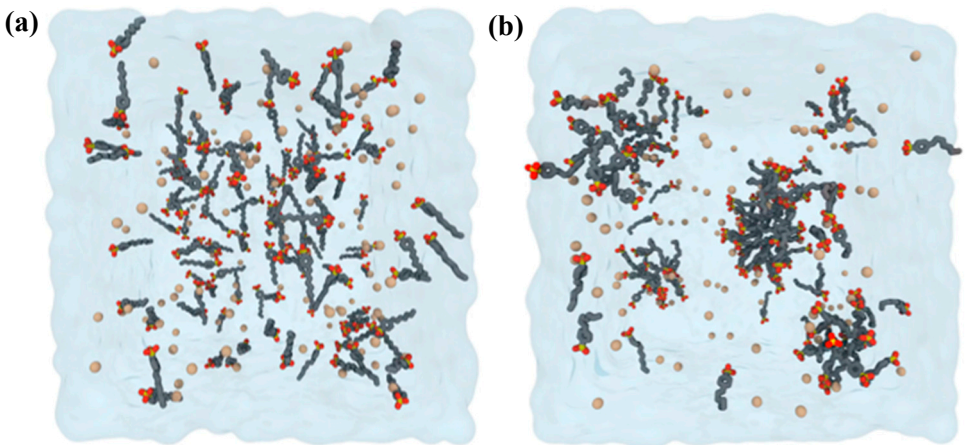

Figure 13: (a) Initial and (b) refined EPSR simulation boxes of surfactant molecules in solution.

As with other reverse modelling techniques, EPSR does not produce a unique structural solution but rather generates one or more plausible configurations consistent with both experimental data and physical constraints. EPSR has been widely used to investigate solvent structure[116,117], hydrogen bonding[118,119] and aggregation phenomena[120,121] in liquids and soft matter. In the context of this thesis, EPSR was used to obtain radial distribution functions, coordination numbers and atomistic configurations that reveal the local structure of two short chained surfactants, allowing for a comparison of differing headgroup structures and their effect on the micelle packing.

3 Summary of Results

This body of work explores the structural behaviour of the bio-derived surfactant STFS, both alone and in combination with common anionic (SDS) and non-ionic ($C_{12}E_6$) surfactants, with particular focus on the air-water interface and bulk aqueous environments at very dilute concentrations. A combination of scattering techniques, surface tension and conductivity measurements provided complimentary insights into the micellar and interfacial characteristics of these binary and ternary mixtures and how its arrangement is shaped by its structure and electrostatic properties. Paper I focuses of the self-assembly behaviour of the binary and ternary mixed surfactants systems, Paper II focuses on the surface behaviour of the binary systems and Paper III focuses on comparisons of two structurally similar surfactants, differing only by the ring structure in the headgroup. The working hypothesis for this work was that the furan headgroup of STFS could enable micellisation and mixing behaviours comparable to those of other common anionic surfactants such as LAS.

3.1 STFS Alone

When studied in isolation, STFS exhibits similar behaviour to other anionic surfactants of similar structures e.g. LAS and SDS, although its relatively higher Krafft temperature limits its use as a standalone surfactant in formulations. The critical micelle concentration (CMC) of STFS was experimentally determined to be 0.69 ± 0.05 mM, similar to that of previous literature of the species.[60] Small-angle X-ray scattering (SAXS) at high concentrations (>20 Wt%) showed phase transitions from a lamellar crystalline phase below the Krafft temperature to a hexagonal liquid crystalline phase upon heating.

In dilute systems at 45 °C, small-angle neutron scattering (SANS) revealed prolate ellipsoidal core–shell micelles with concentration-invariant dimensions (major core axis: 34.2 ± 0.3 Å, minor axis: 26.3 ± 1.6 Å). At the air–water interface, neutron reflectometry (NR) at 45 °C measured an area per molecule (APM) of 41 ± 6 Å², compared to 59 ± 6 Å² determined from surface tension data at 50 °C.

Literature of the similar benzene-based surfactant[49], LAS, shows the APM for the single surfactant to be between 54-61 Å^2 [49–51] with a surface excess value of 3.1 x 10^{-10} mol cm^{-2}, dependent on the technique employed, making it a comparable size to STFS.

3.2 Mixture 1: STFS/$C_{12}E_6$

In STFS/$C_{12}E_6$ mixtures, the absence of electrostatic repulsion and the steric compatibility between headgroups enabled strong synergistic interactions in both bulk and interfacial environments. The CMC was significantly reduced relative to each individual component and to ideal mixing predictions, with the Krafft temperature lowered below room temperature, a clear formulation advantage. SANS at room temperature showed polydisperse core–shell spherical micelles (~55 Å total micelle diameter) that were stable in shape and size across molar ratios and concentrations.

$C_{12}E_6$ reduced electrostatic repulsion between STFS headgroups, leading to micelles dominated by $C_{12}E_6$ at the CMC, but approaching the bulk composition at higher concentrations (10-20 mM). The micelle interaction parameter, β_M, was calculated as -6.68 ± 0.26, indicative of strong bulk synergism. Surface tension data collected at 50 °C gave $\beta_S = -1.87 \pm 0.41$, much smaller in magnitude than β_M. The resultant mole fraction of STFS present at the surface, X_1, increased with increasing bulk STFS content, ranging from 0.25 to 0.37. NR experiments at 45 °C confirmed co-adsorption, with surface mole fractions of STFS (0.46-0.65) exceeding those from surface tension (0.25-0.37).

While literature on structurally similar systems is limited, one study on SDBS/ $C_{12}E_6$ mixtures (where SDBS has a benzene moiety in the headgroup) reported general synergistic behaviour but did not provide explicit β values[6]. In contrast, a study of SDBS/$C_{12}E_8$ with added NaCl (0.1M)[122] reported a micelle β of −3.3 and surface β of −4.8, showing that STFS/ $C_{12}E_6$ mixtures demonstrate stronger synergism in the bulk but slightly weaker at the surface suggesting this pairing is highly adaptable for future formulations.

3.3 Mixture 2: STFS/SDS

STFS/SDS mixtures were expected to show limited compatibility due to like-charge repulsion between sulfonate and sulfate headgroups. At room temperature, poor solubility reflected STFS's high Krafft temperature, but small additions (< 0.1M) of monovalent salts could mitigate this in formulation. At 45 °C, SANS revealed micelles similar in size to those in STFS/$C_{12}E_6$ (Total micelle diameter ~ 51 Å), but with thinner shells due to the smaller sulfate headgroup in SDS compared to the ethoxylated chain in $C_{12}E_6$. SANS contrast variation confirmed minimal SDS in most mixed micelles.

Despite SDS having a much higher CMC (8.2 mM vs. 0.69 mM for STFS), mixed CMCs were significantly lower than SDS alone and ideal mixing predictions, with

β_M = -2.91 ± 0.17, smaller than that of STFS/$C_{12}E_6$ but still indicative of moderate favourable interactions. This is unusually favourable for anionic-anionic systems where typically they have very small interaction parameters[32] (both β_M and β_S) between +1 ≥ β ≥ -1.

Surface tension analysis could not yield a reliable surface interaction parameter due to deviations from the Regular Solution Theory (RST) model at extreme composition values. However, NR data at 45 °C confirmed a high surface mole fraction of STFS, with minimal spectral differences between hh and hd contrasts. Quantification was limited by experimental uncertainty, but the overall picture supports preferential enrichment of STFS at the interface (X_1 > 0.9).

Literature for anionic-anionic systems remains largely unexplored, likely due to strong electrostatic repulsions typically causing unfavourable mixing. Literature on SDBS/SDS mixtures reports slight antagonism at high SDBS content[123] with SDS also underrepresented in those systems, in line with the present findings. Furthermore, surface tension studies showed that the APM of SDBS/SDS mixtures exceeded those of the pure components, attributed to increased headgroup repulsions, again echoing the STFS/SDS behaviour. However, LAS mixed with sodium dodecyl diethylene glycol sulfate (SLES) showed ideal mixing behaviour in the bulk solution and slight synergism at the surface using NR (β_s ~ -2).[124] The STFS/SDS system demonstrates that even anionic-anionic pairs can achieve measurable synergism in the bulk, albeit with strong interfacial selectivity.

3.4 Mixture 3: STFS/SDS/$C_{12}E_6$

Ternary mixtures were hypothesised to display intermediate behaviour between the binary extremes, with $C_{12}E_6$ driving compatibility. SANS confirmed all three surfactants participated in the micelles, with CMCs lower than pure $C_{12}E_6$ but slightly higher than STFS/$C_{12}E_6$ mixtures. SDS remained underrepresented in the micelles, consistent with binary trends. Micelle dimensions remained constant across molar ratios and concentrations, though the aggregation number increased with increasing total anionic surfactant content.

RST predictions based on binary interaction parameters failed to accurately capture the observed behaviour, highlighting the limitations of the model. Further work is required to establish surface behaviour in ternary systems, particularly as RST is likely insufficient to predict interfacial composition.

3.5 Ring Comparison

To assess the influence of headgroup ring type on micelle structure, neutron diffraction experiments were performed on SHBS (sodium heptyl benzene sulfonate) and SHFS (sodium heptyl furan sulfonate) short chain surfactants. Benzene rings allowed tighter packing, potentially via π-π interactions, producing compact, spherical aggregates. In contrast, the more polar furan rings increased steric hindrance, leading to less ordered micelles with more solvent-accessible headgroup regions.

Radial distribution functions and atomic density profiles indicated SHFS had 4 more water molecules per sulfonate than SHBS, a result of loose packing rather than direct hydrogen bonding to the furan oxygen. SHBS retained more sodium counterions at the micelle surface, while SHFS showed great counterion dissociation.

Maximum additive concentration (MAC) tests confirmed that SHBS, with its more compact and ordered structure, was able to encapsulate more hydrophobic cyclohexane than SHFS. This is one of the first molecular-resolution studies showing how subtle aromatic ring changes can modulate micelle packing, hydration and counterion binding.

4 Conclusions and Future Outlook

This thesis presents a detailed investigation of the structural and interfacial properties of the bio-derived surfactant STFS and its binary and ternary mixtures with SDS and $C_{12}E_6$. By combining scattering techniques with interfacial characterisation methods, we have demonstrated how molecular architecture, charge effects, and composition influence surfactant interactions in bulk solution and at the air–water interface.

STFS alone forms well-defined micelles and interfacial films, but its high Krafft temperature limits direct formulation use. Mixing with $C_{12}E_6$ produced strong synergism in both bulk and interfacial behaviour, lowering the CMC, improving solubility and enabling co-adsorption. STFS/SDS mixtures exhibited moderate synergism and an unexpected degree of compatibility for anionic-anionic systems, with STFS dominating interfacial adsorption, but solubility was restricted to elevated temperatures. The ternary STFS/SDS/$C_{12}E_6$ system retained key features of both binary systems, though its behaviour deviated from predictions based on Regular Solution Theory, highlighting the need for further characterisation of these interactions.

Simulations comparing furan- and benzene-based headgroups revealed subtle but important differences in counterion binding, hydration and micelle structure, highlighting how aromatic ring chemistry can be used to tune surfactant performance.

Several additional neutron scattering experiments were completed but not included in this thesis, with the goal to publish them at a later date. Additional studies included considering the effect of mono- and di-valent salts on the mixed systems both in the bulk and at the interface and also SANS using a branched alkyl-chain version of STFS as an alternative to reduce the high Krafft temperature.

Overall, these findings support the potential of STFS in future formulations, particularly in mixtures with non-ionic surfactants. Future work should explore the interfacial behaviour of the ternary system as well as considering other co-surfactants. Whilst this thesis chose common anionic and non-ionic standards, there may be much more preferable choices, especially from the prospective of working towards a more sustainable future.

5 References

1 V. M. León, A. Gómez-Parra and E. González-Mazo, *Environ. Sci. Technol.*, 2004, **38**, 2359–2367.

2 S. Mallakpour and S. Soltanian, *RSC Adv.*, 2016, **6**, 109916–109935.

3 S. Zhou, D. Wei, H. Shi, X. Feng, K. Xue, F. Zhang and W. Song, *Talanta*, 2013, **107**, 349–355.

4 Y. Jin, D. Liu and J. Hu, *Polymers*, 2021, **13**, 1127.

5 X. Pei, S. Zhang, W. Zhang, P. Liu, B. Song, J. Jiang, Z. Cui and B. P. Binks, *Angew. Chem. Int. Ed.*, 2021, **133**, 5295–5299.

6 B. Zhang, B. Guan, Y. Tao, W. Liu, B. Peng and K. Lv, *ACS Omega*, 2024, **9**, 23903–23916.

7 P. Atkins, J. de Paula and J. Keeler, *Atkins' Physical Chemistry*, Oxford University Press, Oxford, New York, Eleventh Edition., 2017.

8 D. N. Rubingh, in *Solution Chemistry of Surfactants: Volume 1*, ed. K. L. Mittal, Springer New York, Boston, MA, 1979, pp. 337–354.

9 D. F. Evans and H. Wennerström, *The Colloidal Domain: Where Physics, Chemistry, Biology, and Technology Meet*, VCH Publishers, 1994.

10 H. Akisada, *J. Colloid Interface Sci.*, 1984, **97**, 105–114.

11 M. M. Mabrouk, N. A. Hamed and F. R. Mansour, *Monatsh Chem*, 2022, **153**, 125–138.

12 N. Scholz, T. Behnke and U. Resch-Genger, *J Fluoresc*, 2018, **28**, 465–476.

13 D. R. Perinelli, M. Cespi, N. Lorusso, G. F. Palmieri, G. Bonacucina and P. Blasi, *Langmuir*, 2020, **36**, 5745–5753.

14 S. E. K. Rideal, *An Introduction to Surface Chemistry*, CUP Archive, 1926.

15 E. E. Walker, *J. Chem. Soc., Trans.*, 1921, **119**, 1521–1537.

16 P. L. du Noüy, *J. Gen. Physiol.*, 1925, **7**, 625–631.

17 C. E. Stauffer, *J. Phys. Chem.*, 1965, **69**, 1933–1938.

18 M. L. Anderson, A. P. Bassom and N. Fowkes, *P Roy Soc A-Math Phy.*, 2006, **462**, 3645–3656.

19 J. J. Jasper, *J. Phys. Chem. Ref. Data.*, 1972, **1**, 841–1010.

20 G. Vazquez, E. Alvarez and J. M. Navaza, *J. Chem. Eng. Data*, 1995, **40**, 611–614.

21 J. P. Fang and P. Joos, *Colloids Surf.*, 1992, **65**, 121–129.

22 A. Javadi, N. Mucic, D. Vollhardt, V. B. Fainerman and R. Miller, *J. Colloid Interface Sci.*, 2010, **351**, 537–541.

23 J. R. Lu, I. P. Purcell, E. M. Lee, E. A. Simister, R. K. Thomas, A. R. Rennie and J. Penfold, *J. Colloid Interface Sci.*, 1995, **174**, 441–455.

24 E. L. Correia, N. Brown, A. Ervin, D. V. Papavassiliou and S. Razavi, *Langmuir*, 2022, **38**, 7179–7189.

25 R. Hargreaves, D. T. Bowron and K. Edler, *J. Am. Chem. Soc.*, 2011, **133**, 16524–16536.

26 D. T. Bowron and K. J. Edler, *Langmuir*, 2017, **33**, 262–271.

27 K. J. Edler and D. T. Bowron, *Mol. Phys.*, 2019, **117**, 3389–3397.

28 Y. Song, R. Sun, K. Zhao, X. Pan, H. Zhou and D. Li, *Colloid Polym Sci.*, 2015, **293**, 1525–1534.

29 J. N. Israelachvili, D. J. Mitchell and B. W. Ninham, *J. Chem. Soc., Faraday Trans. 2*, 1976, **72**, 1525–1568.

30 D. Lombardo, M. A. Kiselev, S. Magazù and P. Calandra, *Adv. Condens. Matter Phys.*, 2015, **2015**, 1–22.

31 C. Tanford, *J. Phys. Chem.*, 1972, **76**, 3020–3024.

32 M. J. Rosen and J. T. Kunjappu, *Surfactants and Interfacial Phenomena*, John Wiley & Sons, 2012.

33 N. V. Lebedeva, A. Shahine and B. L. Bales, *J. Phys. Chem. B*, 2005, **109**, 19806–19816.

34 R. G. Alargova, I. I. Kochijashky, M. L. Sierra and R. Zana, *Langmuir*, 1998, **14**, 5412–5418.

35 C. Wang and H. Morgner, *Phys. Chem. Chem. Phys.*, 2014, **16**, 23386–23393.

36 P. Goon, R. G. Bhirud and V. V. Kumar, *J. Surfactants Deterg.*, 1999, **2**, 489–493.

37 J. A. Stewart, A. Saiani, A. Bayly and G. J. T. Tiddy, *Colloids Surf., A*, 2009, **338**, 155–161.

38 L. Cohen, E. Sanchez, M. Martin, F. Soto and F. Trujillo, *J. Surfactants Deterg.*, 2016, **19**, 1089–1092.

39 D. K. Rout, S. Chauhan and A. Agarwal, *Ind. Eng. Chem. Res.*, 2009, **48**, 8842–8847.

40 X. Wang, X. Liu, Y. Huo and J. Niu, *Tenside Surfactants Detergents*, 2020, **57**, 259–264.

41 F. B. Malihi, A. Khaani, N. Changizi and B. Adeeb, *Tenside Surf. Det.*, 2011, **48**, 395–399.

42 G. Broze, Ed., *Handbook of Detergents, Part A: Properties*, CRC Press, Boca Raton, 1999.

43 J.-G. Ma, B. J. Boyd and C. J. Drummond, *Langmuir*, 2006, **22**, 8646–8654.

44 I. Tucker, J. Penfold, R. K. Thomas, C. C. Dong, S. Golding, C. Gibson and I. Grillo, *Langmuir*, 2011, **27**, 6674–6682.

45 F. N. Baumgartner, *Ind. Eng. Chem.*, 1954, **46**, 1349–1352.

46 J. R. Liley, J. Penfold, R. K. Thomas, I. Tucker, J. Petkov, P. Stevenson, I. M. Banat, R. Marchant, M. Rudden and J. Webster, *J. Colloid Interface Sci.*, 2019, **534**, 64–71.

47 R. Bradbury, J. Penfold, R. K. Thomas, I. M. Tucker, J. T. Petkov and C. Jones, *Langmuir*, 2013, **29**, 3361–3369.

48 R. K. Thomas and J. Penfold, *Soft Matter*, 2025, **21**, 3534–3546.

49 J. Penfold, R. K. Thomas, C. C. Dong, I. Tucker, K. Metcalfe, S. Golding and I. Grillo, *Langmuir*, 2007, **23**, 10140–10149.

50 S. K. Hait, P. R. Majhi, A. Blume and S. P. Moulik, *J. Phys. Chem. B*, 2003, **107**, 3650–3658.

51 D. C. H. Cheng and E. Gulari, *Journal of Colloid and Interface Science*, 1982, **90**, 410–423.

52 S. B. Sulthana, S. G. T. Bhat and A. K. Rakshit, *BCSJ*, 2000, **73**, 281–287.

53 D. C. H. Cheng and E. Gulari, *J. Colloid Interface Sci.*, 1982, **90**, 410–423.

54 M. R. Watry and G. L. Richmond, *J. Am. Chem. Soc.*, 2000, **122**, 875–883.

55 X. He, O. Guvench, A. D. Jr. MacKerell and M. L. Klein, *J. Phys. Chem. B*, 2010, **114**, 9787–9794.

56 W. Zuo and H.-W. Wong, *Green Chem. Lett. Rev.*, 2017, **10**, 393–403.

57 M. Rezaei and R. Tarvirdi-zadeh, *Int. J. New Chem.*, 2019, **6**, 76–78.

58 A. Velty, S. Iborra and A. Corma, *ChemSusChem*, 2022, **15**, e202200181.

59 X. Yue and Y. Queneau, *ChemSusChem*, 2022, **15**, e202102660.

60 D. S. Park, K. E. Joseph, M. Koehle, C. Krumm, L. Ren, J. N. Damen, M. H. Shete, H. S. Lee, X. Zuo, B. Lee, W. Fan, D. G. Vlachos, R. F. Lobo, M. Tsapatsis and P. J. Dauenhauer, *ACS Cent. Sci.*, 2016, **2**, 820–824.

61 J. Lu, R. Hou, Y. Wang, L. Zhou and Y. Yuan, *Water Research*, 2022, **226**, 119277.

62 A. Kumar, W. A. Ansari, T. Ahamad, M. Saquib and M. F. Khan, *COVID*, 2021, **2**, e120821189929.

63 Y. Zhang, B. Zhang, S. Yang, Z. Zhong, H. Zhou and X. Luo, *Int. J. Min. Sci. Technol.*, 2021, **31**, 995–1002.

64 M. H. Ropers, G. Czichocki and G. Brezesinski, *J. Phys. Chem. B*, 2003, **107**, 5281–5288.

65 D. T. Allen, Y. Saaka, L. Carlos Pardo, M. Jayne Lawrence and C. D. Lorenz, *Phys. Chem. Chem. Phys.*, 2016, **18**, 30394–30406.

66 S. Pandey, R. P. Bagwe and D. O. Shah, *J. Colloid Interface Sci.*, 2003, **267**, 160–166.

67 J. B. Hayter and J. Penfold, *Colloid. Polym. Sci.*, 1983, **261**, 1022–1030.

68 B. D. Flockhart, *J. Colloid Sci.*, 1961, **16**, 484–492.

69 D. Otzen, *Biochimica et Biophysica Acta (BBA) - Proteins and Proteomics*, 2011, **1814**, 562–591.

70 J. R. Lu, A. Marrocco, T. J. Su, R. K. Thomas and J. Penfold, *J. Colloid Interface Sci.*, 1993, **158**, 303–316.

71 M. Alibrahim, *Tenside Surf. Det.*, 2012, **49**, 330–334.

72 G. Briganti and A. Bonicontro, *J. Non-Cryst. Solids*, 1994, **172–174**, 1173–1177.

73 Wyn. Brown and Roger. Rymden, *J. Phys. Chem.*, 1987, **91**, 3565–3571.

74 W. Brown, R. Johnsen, P. Stilbs and B. Lindman, *J. Phys. Chem.*, 1983, **87**, 4548–4553.

75 J. Gapiński, J. Szymański, A. Wilk, J. Kohlbrecher, A. Patkowski and R. Hołyst, *Langmuir*, 2010, **26**, 9304–9314.

76 L.-J. Chen, S.-Y. Lin, C.-C. Huang and E.-M. Chen, *Colloids Surf. A Physicochem. Eng. Asp.*, 1998, **135**, 175–181.

77 W. C. Swope, M. A. Johnston, A. I. Duff, J. L. McDonagh, R. L. Anderson, G. Alva, A. T. Tek and A. P. Maschino, *J. Phys. Chem. B*, 2019, **123**, 1696–1707.

78 D. John Mitchell, G. J. T. Tiddy, L. Waring, T. Bostock and M. P. McDonald, *J. Chem. Soc., Faraday Trans. 1.*, 1983, **79**, 975–1000.

79 R. Triolo, L. J. Magid, J. S. Johnson and H. R. Child, *J. Phys. Chem.*, 1982, **86**, 3689–3695.

80 F. Sterpone, C. Pierleoni, G. Briganti and M. Marchi, *J Phys Chem B*, 2006, **110**, 18254–18261.

81 J. R. Lu and R. K. Thomas, *MRS Proc.*, 1994, **376**, 235–240.

82 J. Penfold, E. Staples, I. Tucker, L. Thompson and R. K. Thomas, *J. Colloid Interface Sci.*, 2002, **247**, 404–411.

83 J. H. Clint, *J. Chem. Soc., Faraday Trans. 1*, 1975, **71**, 1327–1334.

84 A. Shiloach and D. Blankschtein, *Langmuir*, 1998, **14**, 4105–4114.

85 M. L. Chen, J. Penfold, R. K. Thomas, T. J. P. Smyth, A. Perfumo, R. Marchant, I. M. Banat, P. Stevenson, A. Parry, I. Tucker and I. Grillo, *Langmuir*, 2010, **26**, 17958–17968.

86 J. D. Hines, R. K. Thomas, P. R. Garrett, G. K. Rennie and J. Penfold, *J. Phys. Chem. B*, 1998, **102**, 8834–8846.

87 J. D. Hines, R. K. Thomas, P. R. Garrett, G. K. Rennie and J. Penfold, *J. Phys. Chem. B*, 1997, **101**, 9215–9223.

88 R. Nagarajan, *Langmuir*, 1985, **1**, 331–341.

89 R. Nagarajan and E. Ruckenstein, *Langmuir*, 1991, **7**, 2934–2969.

90 R. F. Kamrath and E. I. Franses, *J. Phys. Chem.*, 1984, **88**, 1642–1648.

91 V. P. Arkhipov, R. V. Arkhipov, E. V. Petrova and A. Filippov, *Magn. Reson. Chem.*, 2023, **61**, 345–355.

92 P. Eslami, H. Hajfarajollah and S. Bazsefidpar, *RSC Advances*, 2020, **10**, 34014–34032.

93 M. Chen, C. Dong, J. Penfold, R. K. Thomas, T. J. P. Smyth, A. Perfumo, R. Marchant, I. M. Banat, P. Stevenson, A. Parry, I. Tucker and R. A. Campbell, *Langmuir*, 2011, **27**, 8854–8866.

94 S. Pal, N. Chatterjee, A. K. Das, D. J. McClements and P. Dhar, *Adv. Colloid Interface Sci.*, 2023, **313**, 102856.

95 M. Abe, K. Mizuguchi, Y. Kondo, K. Ogino, H. Uchiyama, J. F. Scamehorn, E. E. Tucker and S. D. Christian, *J. Colloid Interface Sci.*, 1993, **160**, 16–23.

96 Y. Tokuoka, H. Uchiyama, M. Abe and K. Ogino, *J. Colloid Interface Sci.*, 1992, **152**, 402–409.

97 Y. Tokuoka, H. Uchiyama, M. Abe and S. D. Christian, *Langmuir*, 1995, **11**, 725–729.

98 V. Tchakalova, in *Design and Applications of Self-Assembly Aggregates - From Micelles to Nanoemulsions*, IntechOpen, 2024.

99 O. Glatter, *Scattering Methods and their Application in Colloid and Interface Science*, 2018.

100 P. Lindner and J. Oberdise, *Neutrons, X-rays, and Light: Scattering Methods Applied to Soft Condensed Matter*, 2024.

101 T. Narayanan, *Adv. Colloid Interface Sci.*, 2024, **325**, 103114.

102 H. Schnablegger and Y. Singh, *The SAXS Guide: Getting acquainted with the principles*, Anton Paar GmbH, 4th Edition., 2017.

103 M. Kotlarchyk and S. Chen, *J. Chem. Phys.*, 1983, **79**, 2461–2469.

104 P. Bartlett and R. H. Ottewill, *J. Chem. Phys.*, 1992, **96**, 3306–3318.

105 J. R. Liley, J. Penfold, R. K. Thomas, I. M. Tucker, J. T. Petkov, P. S. Stevenson, I. M. Banat, R. Marchant, M. Rudden, A. Terry and I. Grillo, *J. Colloid Interface Sci.*, 2017, **487**, 493–503.

106 E. Fermi, *Reflection of Neutrons on Mirrors*, Manhattan District, 1946.

107 M. Delcea and C. A. Helm, *Langmuir*, 2019, **35**, 8519–8530.

108 J. H. Lakey, *Curr. Opin. Colloid Interface Sci.*, 2019, **42**, 33–40.

109 J. Penfold and R. K. Thomas, *Curr. Opin. Colloid Interface Sci.*, 2023, **68**, 101766.

110 O. S. Heavens, *Rep. Prog. Phys.*, 1960, **23**, 1.

111 J. Penfold, M. Chen, R. K. Thomas, C. Dong, T. J. P. Smyth, A. Perfumo, R. Marchant, I. M. Banat, P. Stevenson, A. Parry, I. Tucker and I. Grillo, *Langmuir*, 2011, **27**, 8867–8877.

112 R. A. Campbell, Y. Saaka, Y. Shao, Y. Gerelli, R. Cubitt, E. Nazaruk, D. Matyszewska and M. J. Lawrence, *J. Colloid Interface Sci.*, 2018, **531**, 98–108.

113 A. K. Soper, *Mol. Phys.*, 2009, **107**, 1667–1684.

114 A. K. Soper, GudrunN and GudrunX: Programs for correcting raw neutron and x-ray total scattering data to differential cross section 2012.

115 A. K. Soper, *Mol. Phys.*, 2001, **99**, 1503–1516.

116 D. T. Bowron and S. Díaz-Moreno, *J. Phys. Chem. B*, 2009, **113**, 11858–11864.

117 J. M. M. Cordeiro and A. K. Soper, *J. Phys. Chem. B*, 2009, **113**, 6819–6825.

118 J. J. Towey, A. K. Soper and L. Dougan, *J. Phys. Chem. B*, 2012, **116**, 13898–13904.

119 P. Sillrén, J. Swenson, J. Mattsson, D. Bowron and A. Matic, *J. Chem. Phys.*, 2013, **138**, 214501.

120 A. K. Soper and K. J. Edler, *Biochimica et Biophysica Acta (BBA) - General Subjects*, 2017, **1861**, 1652–1660.

121 M. Di Gioacchino, M. A. Ricci, S. Imberti, N. Holzmann and F. Bruni, *J. Mol. Liq.*, 2020, **301**, 112407.

122 P. Liljekvist and B. Kronberg, *J. Colloid Interface Sci.*, 2000, **222**, 159–164.

123 G. Basu Ray, I. Chakraborty, S. Ghosh and S. P. Moulik, *Colloid Polym Sci*, 2007, **285**, 457–469.

124 J. R. Liley, R. K. Thomas, J. Penfold, I. M. Tucker, J. T. Petkov, P. Stevenson and J. R. P. Webster, *J. Phys. Chem. B*, 2017, **121**, 2825–2838.

Paper I-III

Paper I

Journal of Colloid and Interface Science 699 (2025) 138201

Contents lists available at ScienceDirect

Journal of Colloid And Interface Science

journal homepage: www.elsevier.com/locate/jcis

Mixed micellar solutions of an oleo-furan sulfonate surfactant with anionic and non-ionic surfactants

Laura Deeming [a,b], Niamh R. Leaman [a,b], Dirk Honecker [c], Yao Chen [c], Kun Ma [c], Karen J. Edler [a,*]

[a] Center for Analysis and Synthesis, Department of Chemistry, Lund University, Naturvetarvägen 22, Lund 223 62, Sweden
[b] Division of Physical Chemistry, Department of Chemistry, Naturvetarvägen 22, Lund University, 22362 Lund, Sweden.
[c] ISIS Neutron and Muon Source, Science and Technology Facilities Council, Rutherford Appleton Laboratory, Didcot, OX11 0QX Oxfordshire, United Kingdom

GRAPHICAL ABSTRACT

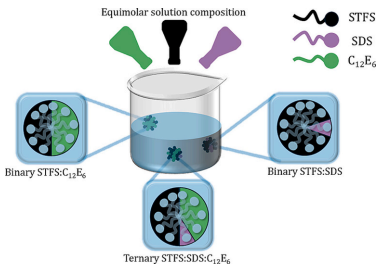

ABSTRACT

Small angle neutron scattering (SANS) has been employed to examine the self-assembly behaviour of sodium 5-tetradecyl furan-2-sulfonate (STFS), an emerging anionic surfactant, in bulk dilute solutions. STFS was also studied in binary and ternary mixtures with a common non-ionic (hexaethylene glycol monododecyl ether, $C_{12}E_6$) and anionic (sodium dodecyl sulfate, SDS) surfactant to explore the shape, size and composition of the mixed systems in dilute solution. SANS confirmed that STFS alone formed prolate ellipsoidal micelles and transitioned to small polydisperse spherical core-shell micelles of 55 ± 5 Å diameter for mixed systems. Anionic/non-ionic STFS/$C_{12}E_6$ mixtures exhibited strong synergistic interactions, with a significant reduction in critical micelle concentration (CMC) and preferential incorporation of $C_{12}E_6$ into the micelle compared to bulk solution molar ratios. In contrast, STFS/SDS mixtures showed weaker synergism, with minimal SDS incorporation attributed to electrostatic repulsions. Ternary systems displayed intermediate behaviour, with STFS and $C_{12}E_6$ dominating micelle formation while SDS remained mostly excluded. At higher concentrations (10, 20 mM) in SANS measurements the STFS/$C_{12}E_6$ tended towards more bulk solution molar ratio mixing behaviour whilst SDS stayed minimally incorporated into the micelle, regardless of concentration.

1. Introduction

Surfactants are a critical component in home and personal care products such as detergents. Typically, these products contain a mixture of surfactant types, optimising synergistic interactions to enable maximum performance at concentrations well below the (CMC) of each

* Corresponding author.
E-mail address: karen.edler@chem.lu.se (K.J. Edler).

https://doi.org/10.1016/j.jcis.2025.138201
Received 7 May 2025; Received in revised form 12 June 2025; Accepted 14 June 2025
Available online 17 June 2025

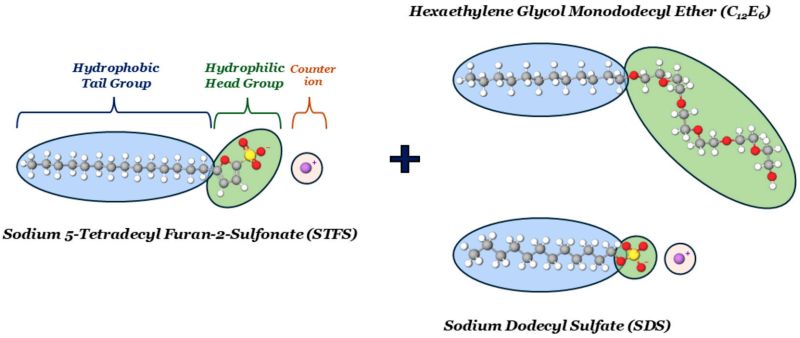

Fig. 1. Chemical structures of sodium 5-tetradecyl furan-2-sulfonate (STFS), hexaethylene glycol monododecyl ether ($C_{12}E_6$) and sodium dodecyl sulfate (SDS).

individual surfactant. In practise, these mixtures are also a balance between many other components present in the detergent, including fragrance, enzymes and builders. However, understanding the fundamental properties of a surfactant mixture alone is the vital first step to achieve formulation before extrapolating to the effect of other components.

The most commonly used industrial surfactants in detergents are currently derived from petrochemical feedstocks [1], making them an unsustainable option for the future. To address environmental concerns there is a growing interest in biobased surfactants such as rhamnolipids [2], surfactin [3] and sophorolipids [4] as well as alternative synthesis options using biomass feedstocks [5]. However, these materials still face many challenges, in that production costs remain too high and most processes cannot be scaled to the quantities needed to fully replace petrochemical-derived surfactants [6,7].

An emerging class of anionic surfactants which holds promise as an industrial alternative are oleo-furan surfactants (OFS), with the key feature of a furan sulfonate hydrophilic head group. These surfactants have been reported in recent years [8,9] but the extent of published analysis on the physiochemical properties has mostly been limited to efficiency tests, CMC determination and hard water micelle stability tests of the single surfactants in comparison to similar common surfactants such as sodium dodecyl sulfate (SDS) or linear alkyl benzene sulfonate (LAS). This research aims to provide a further insight into the packing and arrangement of this emerging surfactant type in bulk solution along with its interaction with commonly used surfactants.

The OFS of interest in this paper is one of the simpler variations, sodium tetradecyl furan sulfonate (STFS, Fig. 1). STFS has only a furan ring and sulfonate head group, with no other linker atoms between the hydrophilic head group and hydrophobic linear alkyl chain. This allows us to focus on the ring structure and consider whether it contributes to beneficial packing within the micelle, particularly in comparison to the widely studied linear alkyl benzene sulfonates [10–12] which share a similar structure but feature a benzene ring instead of the furan. STFS can be synthesised from bio-derived materials such as 5-(hydroxymethyl)furfural (HMF) and fatty acids [9,13] making it a promising alternative to conventional petrochemically derived surfactants.

Mixtures of surfactants are frequently employed in industrial applications to achieve synergistic optimisation of properties depending on their designed use. Anionic surfactants are typically present due to their strong adsorption to dirt, their high foaming ability [18] and their ability to suspend particulates. Non-ionic surfactants are useful for emulsifying oils and are effective in mixed micelles with anionic surfactants to reduce the electrostatic repulsions between the charged headgroups, lowering the CMC of the mixed micelle. It is therefore critical to examine the nature of the interactions between these surfactant head groups. There have been an extensive range of studies related

Table 1
- Literature values for the properties of surfactants used in this study.

	Surfactant type	CMC (mM)	Krafft temperature, T_k (°C)	Cloud point, T_c (°C)
STFS	**Anionic**	**0.73**[8]	**41.5**[8]	–
SDS	**Anionic**	**8.20**[14]	**16–17**[15]	–
$C_{12}E_6$	**Non - ionic**	**0.09**[16]	–	**48.5**[17]

to mixtures of surfactants in the bulk solution, mostly dominated by ionic – non-ionic mixtures [19–21] but also to a lesser extent, non-ionic mixtures [22–24] and zwitterionic mixtures [25,26]. While many papers focus on binary surfactant mixtures in water, more complex compositions of ternary [27–32] and 5 component [33] systems have also been explored. Various methods are available to study the bulk micellar properties including EPR [34,35], NMR [36,37] and most commonly SANS [38,39]. Small angle neutron scattering is ideal for studying mixed micellar systems through the use of selective deuteration of different components to extract micellar compositions and, since it probes the ideal size-scale, for both structural determination of the micelle and the interactions between micelles.

In order to understand the complexities of surfactant mixing, it is crucial to explore the system at both initial micellisation, i.e. at the CMC, as well as at much higher concentrations that are closer to application uses. Sodium dodecyl sulfate (SDS) and hexaethylene glycol monododecyl ether ($C_{12}E_6$) have been selected here for the mixed surfactant system studies with STFS. Both have been chosen due to the substantial amount of literature available (See Table 1) both for the individual surfactants [40–45] and their mixtures [46–49].

Several frameworks have been developed to describe micellar systems. The pseudophase approximation assumes that above the CMC the system exists as two separate phases; an aqueous phase and a micellar phase, coexisting simultaneously. For this theory, it is assumed that a sharp transition occurs as these two pseudophases form.

Using this theory, and assuming ideal mixing of a binary surfactant system, as described by Clint [50], allows for descriptions of micellar systems with similar head groups and thus for a predicted calculation of a CMC value based on the individual surfactant CMCs. There is an assumption that the interactions between the surfactants are identical to those of the pure surfactants even when mixed and that there are no preferential or antagonistic interactions. However, there is commonly non-ideal mixing within a mixed surfactant system and typically the micellisation process can be better described using Rubinghs regular solution theory (RST) [51], which explains deviations from ideal mixing using the interaction parameter, β, accounting for the net (pairwise) interactions between the headgroups of the surfactant monomers as shown below:

$$\beta_{12} = \frac{N_A(W_{11} + W_{22} - 2W_{12})}{RT} \quad (1.1)$$

where N_A is Avogadro's number and W_{11}, W_{22} and W_{12} are the energies of the pairwise interactions between surfactants 1 and 2. Regular solution theory can theoretically predict the CMC of a binary mixed system using:

$$\frac{1}{CMC_{12}} = \frac{\alpha_1}{f_1 CMC_1} + \frac{1-\alpha_1}{f_2 CMC_2} \quad (1.2)$$

With CMC_1 and CMC_2 representing the CMC values of the individual pure surfactants, α_1 the mole fraction of surfactant 1 in solution and f_1 and f_2, the activity coefficients of the surfactants. These activity coefficients can be related to the interaction parameter through the equations:

$$f_1 = \exp \beta_{12}(1 - x_1)^2 \quad (1.3a)$$

$$f_2 = \exp \beta_{12}(x_1)^2 \quad (1.3b)$$

where x_1 is the mole fraction of surfactant 1 in the micelle. The value for x_1 can be found by iteratively solving eq. 1.2 using the known solution composition, CMC values of both the individual surfactants, and the experimentally measured CMC for the mixed micelle.

For the ideal mixing of a mixed surfactant micelle, the value of β_{12} would amount to zero and the values of both f_1 and f_2 would be 1. Departure from ideal mixing leads to variation of the beta parameter. A negative value of β_{12} implies there are synergistic interactions between the surfactant head groups, leading to favourable formation of the mixed micelle and a positive deviation implies net antagonistic interactions between surfactants, usually indicative of strong electrostatic repulsions between similarly charged headgroups. Different approaches to the characterisation of the thermodynamics of mixing of surfactants also exist; including that of Nagarajan [52], the mass action model [53], Markov chain modelling [54] and several molecular dynamics approaches [55,56]. RST is most commonly used due to its simplicity and applicability in most cases.

2. Experimental

2.1. Materials

Sodium 5-tetradecyl furan-2-sulfonate (STFS, ≥99 %) was synthesised by Prosynth, UK and used as provided. Hydrogenated sodium dodecyl sulfate (h-SDS, ≥99 %) and hexaethylene glycol monododecyl ether (h-$C_{12}E_6$, ≥98 %) were purchased from Sigma Aldrich and used without further purification. Deuterated SDS (98.5 % atom % D, purity ≥99 %) and tail-deuterated $C_{12}E_6$ (97 % atom % D, purity ≥99 %) were supplied by ISIS Deuteration Lab, UK. Deuterium Oxide (99.9 % atom % D) used for SANS measurements was purchased from Sigma Aldrich and Milli-Q Ultrapure water was used throughout (18.2 MΩ.cm resistivity at 25 °C). All glassware and cells used throughout experiments were cleaned using Hellmanex 2 % solution, an ethanol/acetone rinse and thoroughly rinsed with Milli-Q water before oven drying.

3. Methods

3.1. Small angle neutron scattering (SANS)

SANS experiments were carried out at ISIS Pulsed Neutron and Muon Source at the Rutherford Appleton Laboratory (RAL, Didcot, UK) on the Larmor and Zoom beamlines using the white beam time-of-flight method. A Q range of 0.005–0.65 $Å^{-1}$ was achieved using a wavelength range of 0.9–13.5 Å and sample detector distance (SDD) of 5 m for Larmor. A wavelength range of 1.75–16.5 Å and SDD of 4 m was used on Zoom to give a Q range of 0.004–0.75 $Å^{-1}$. Beam diameters of 5 × 5 mm and 8 × 6 mm were used on Larmor and Zoom respectively. All samples were run using quartz Hellma cells with 1 mm path length and 1 cm width. Binary and ternary surfactant mixtures of varying molar compositions were measured at 5, 10 and 20 mM total surfactant concentration and at 25 and 45 °C using a temperature controlled multi-position sample changer. It should be noted that some solutions (notably STFS alone or mixed with SDS) were not soluble at 25 °C and were therefore omitted at these lower temperatures. All samples were run in 100 % D_2O unless otherwise stated, with contrast arising only from varying the deuteration of surfactants in the mixtures. Scattering from both the solvent and cell were subtracted during data reduction.

The scattered intensity was measured as a function of the momentum transfer, Q, using $Q = (4\pi/\lambda) \cdot \sin(2\theta/2)$, where λ is the wavelength of the neutron and 2θ is the scattering angle. For micelles in solution, the scattering cross section can be represented using the expression

$$I(Q) = \phi \bullet P(q) \bullet S(q) + Bkg \quad (2.1)$$

where ϕ represents the volume fraction of the micelles in solution, influenced by the concentration of surfactant in solution. The addition of a background constant allows for acknowledgement of incoherent scattering, mostly due to hydrogen present in the system. Eq. 2.1 assumes a decoupling approximation, where P(q) and S(q) are assumed to be independent. This approach is valid for these systems due to the low volume fractions and the low polydispersities observed under these experimental conditions.

SANS data analysis was performed using a model-based approach with all data at different contrasts co-fitted using the NIST NCNR SANS Analysis macros package in Igor Pro (Wavemetrics) [57]. Unless otherwise stated, the form factor, P(Q), is used to describe the micellar structure with a polydisperse core-shell spherical model [58] chosen, a common approach when considering globular micelles. The model calculates P(q) using the below equation:

$$P(q) = \frac{3}{V_s}\left[V_c(\rho_c - \rho_s)\frac{\sin(qr_c) - qr_c\cos(qr_c)}{(qr_c)^3} + V_s(\rho_s - \rho_{solvent})\frac{\sin(qr_s) - qr_s\cos(qr_s)}{(qr_s)^3}\right] \quad (2.2)$$

where r_c represents the radius of the hydrophobic core, assumed to contain only the alkyl hydrocarbon chains of the surfactants, with a theoretical limiting value of the length of a fully extended C_{14} chain (~18 Å). r_s represents the total micelle radius which includes the alkyl core radius plus the polar shell radius, consisting of the hydrophilic shell groups and a certain degree of hydration. ρ_c and ρ_s are the scattering length densities of the core and shell respectively. V_c and V_s are the micellar core and total volume respectively and can be calculated using the volume of a sphere, $V = (4\pi/3)\cdot r_x^3$ where r_x is either the core radius, r_c, or the total micelle radius r_s. The form factor is normalised by the average particle volume using a Schulz distribution to represent the polydisperse nature of the system.

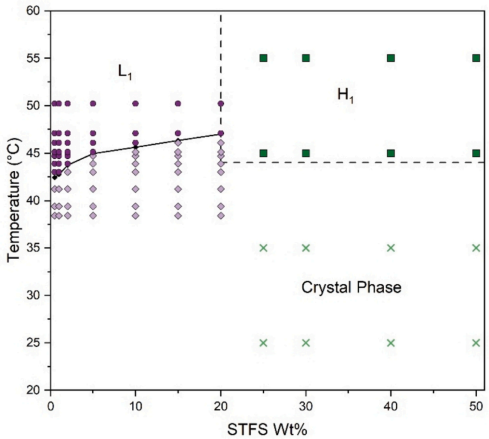

Fig. 2. Schematic phase diagram of STFS in solution as a function of concentration and temperature (x and ■ denote data points measured by SAXS showing the lamellar crystal phase and hexagonal phase respectively. ◆ and ● denote data points measured using birefringence for Krafft temperature determination, where ◆ represent samples below and ● represent samples above the Krafft temperature (solid line).

The Hayter-Penfold screened Coulomb structure factor is applied to describe the inter-particle interactions between spherical objects due to repulsion of charged particles. The structure factor is derived from the Ornstein-Zernike equation and mean spherical approximation (MSA) and takes into account the particle volume fraction (V_f), effective particle charge (z), ionic strength of the system and the dielectric constant of the medium (for water, $\varepsilon \sim 78$ at 25 °C). In this case, the ionic strength was set to zero, and contributions from the surfactant counterions are accounted for in the effective particle charge, which enables counterion binding to the ionic surfactant headgroups to be taken into consideration.

The fits were confirmed by starting the fitting multiple times, from a range of initial values; this returned very similar values for the fitted parameters, suggesting that the fits are robust. To quantify uncertainties, we also compared manually varying parameters until the change affected the quality of the fit. The extent to which a parameter value could be altered without affecting fit quality was similar across all fits and larger than the variation between fits from different starting values, so this is reported as the uncertainty in the tabulated values.

3.2. Small angle X-ray scattering (SAXS)

SAXS measurements for the highly concentrated STFS samples were performed using a SAXSLab Ganesha 300XL pinhole instrument (SAXSLab ApS, Skovlunde, Denmark) using a Cu K_α X-ray microsource, $\lambda = 1.54$ Å and covering a q-range of 0.005–0.73 $Å^{-1}$. Samples were contained in temperature-controlled mica window sandwich cells, thermostatted using a Julabo recirculating water bath. Scattering intensity, I (q), was obtained by radial averaging of the 2D scattering pattern, collected using a 2D 300 k Pilatus detector (Dectris, Switzerland).

3.3. Surface tension

CMC measurements for all binary and ternary mixtures were completed using the Du Nouy ring method [59] on an Attention Sigma 701 tensiometer with a Pt—Ir Du Nouy ring, measuring the equilibrium surface tension of the air/water interface upon addition of the surfactant solution. The addition of surfactant over time to pure Milli-Q water was automated using the Schott Titronic Dispenser and OneAttension software. In the case where a surfactant solution was not soluble at room temperature, a jacketed temperature-controlled beaker and self-circulating water bath were used to maintain a constant temperature of 50 °C and a heated concentrated surfactant mixture was manually pipetted into the beaker before equilibrating. The critical micelle concentration was taken to be the point after which the surface tension ceased to change, although small amounts of surface-active impurities can make this point more difficult to define. Data reported is an average of three CMC measurements with error bars representing the standard deviation.

3.4. Conductivity

Conductance measurements were taken using a Mettler Toledo SevenExcellence and the InLab Trace low conductivity probe, with a cell constant of approximately 0.01 cm^{-1}. Analogous to surface tension measurements, concentrated solutions of surfactant were added manually over time to pure Milli-Q water either at room temperature (25 °C) or high temperature (50 °C). The break point in the slope of the specific conductivity plotted against concentration was taken as the critical micelle concentration [60]. Measurements of the CMC via conductivity were repeated at least twice.

4. Results and discussion

4.1. Phase diagram of STFS

Given that STFS is a surfactant of emerging interest in literature, analysis was undertaken to characterise its surfactant properties at both dilute and high concentrations. Measurements were taken across the concentration range of 0.5 to 50 wt% and between the temperature range of 25 °C to 55 °C. Fig. 2 shows a simplified phase diagram for STFS, highlighting a Krafft temperature of 43 °C, determined by heating the sealed surfactant solution until clear and confirming no birefringence using cross polarizing filters. This value is consistent with previous literature reports of 41.5 °C by Dauenhauer et al. [8] with the slight variation assumed to be related to varying production sources, varying methods of Krafft temperature determination and possibly small amounts of impurities. This elevated Krafft temperature can be attributed to the C_{14} chain as the equivalent C_{12} surfactant exhibits a Krafft temperature of 30 °C [8]. STFS is structurally similar to linear alkylbenzene sulfonate (LAS), a widely used commercial surfactant that is prominent in literature studies [10–12,61]. However, STFS exists as the pure 1-positional isomer which also contributes significantly to the high Krafft temperature. Most previous studies of LAS used either the LAS-6 positional isomer or a commercial grade sodium dodecyl benzene sulfonate (SDBS) which contains a mixture of positional isomers, both of which are much more soluble in water [62,63]. STFS also has a rich phase behaviour at higher concentrations with transition from the micellar region to hexagonal phases, observed through SAXS (Fig. S1). The SAXS temperature study of the higher wt% samples (25–50 wt%) showed a common transition from lamellar-like crystal peaks to the more disordered hexagonal liquid crystal phase with increasing temperatures. Notably this transition appeared to occur at approximately the Krafft temperature, indicating a transition from the crystalline form to the liquid crystalline phase after tail melting occurs.

5. CMC determination

5.1. STFS

The CMC of STFS was determined using both surface tension and conductivity measurements as a function of surfactant concentration (Fig. 3) at 50 °C to ensure solubility above the Krafft temperature (See

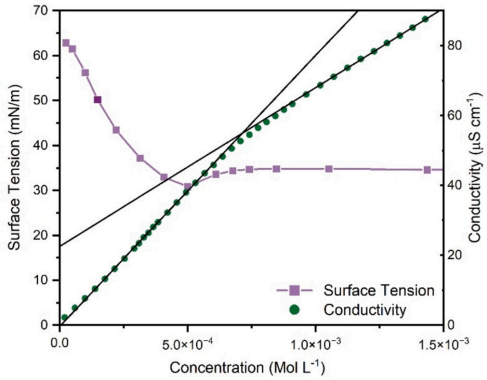

Fig. 3. Determination of the CMC for STFS using tensiometry (■) and conductivity (●) at 50 °C. Uncertainties in data points for both are smaller than symbol size.

Table 2). In typical surfactant systems the CMC is seen as a breakpoint in the data as the surfactant transitions from existing as monomers in solution to aggregate as micelles. A slight minimum exists in the surface tension data, typically indicating the presence of a more surface-active impurity. The CMC from surface tension is therefore defined here as being the first data point after the minima occurs, before the surface tension has stabilised at a constant value. Conductivity measurements provide additional insight, as the technique is not sensitive to surface impurities and can instead give insights into the ion mobility of the surfactant solutions. For typical charged surfactant systems, the gradient of the specific conductivity decreases after the CMC breakpoint as micelles form. This breakpoint coincides with the CMC determined by surface tension. The combination of both methods allows for a more complete picture of the micellisation process. Literature values report the CMC as 0.73 mM[8] for STFS (referred to as OFS-14 in reference [8] and our work remains consistent with this, with CMC values of 0.69 ± 0.05 mM.

5.2. Binary mixtures (STFS/SDS and STFS/$C_{12}E_6$)

In order to explore synergies between STFS and commonly studied anionic and non-ionic species, mixtures of this novel surfactant with SDS and $C_{12}E_6$ were studied. Mixtures of STFS and SDS were insoluble at room temperature but became soluble at the elevated temperatures of 50 °C. In contrast, addition of the non-ionic $C_{12}E_6$ to STFS gave a stable

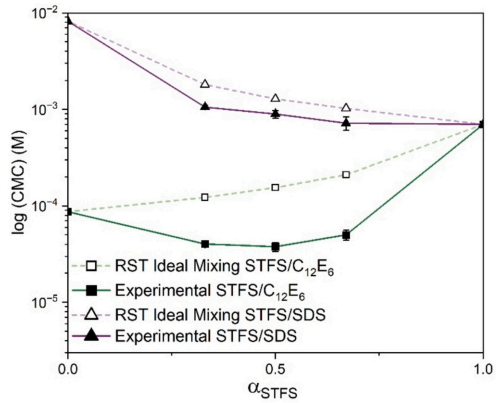

Fig. 5. Comparison of CMC values predicted by RST ideal mixing (dashed lines) and experimentally determined (solid lines) CMC values as a function of the mole fraction of sodium tetradecyl furan sulfonate (STFS) in solution (α). Uncertainties are the maximum variation from CMC experiments performed at least twice.

Table 2-
Thermodynamic and surface properties of STFS. CMC_{lit} is the literature CMC value, CMC_{cond} and CMC_{ST} are the experimental CMC values using conductivity and surface tension respectively. γ represents the surface tension of the surfactant solution. The degree of counterion dissociation is calculated from the change in slope of the conductivity curve before and after the CMC. Uncertainties are the standard deviations in values from triplicate measurements.

	Temperature (°C)	CMC_{lit}, (mM)	CMC_{cond}, (mM)	CMC_{ST}, (mM)	γ above CMC (mN/m)	Degree of dissociation, α
STFS	**50**	**0.73**[8]	**0.67 ± 0.05**	**0.71 ± 0.03**	**31.8 ± 2.9**	**0.60 ± 0.01**

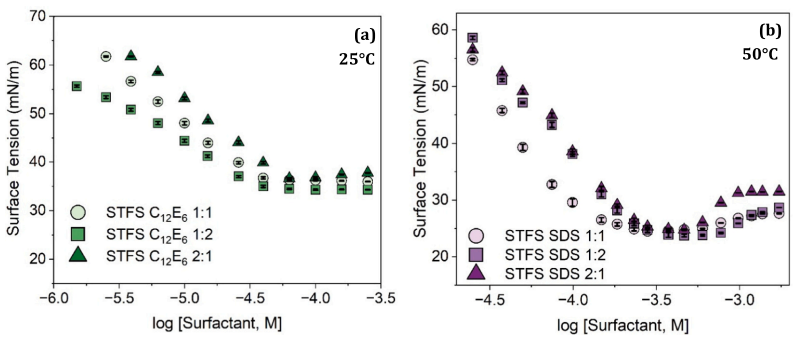

Fig. 4. Equilibrium surface tension as a function of the total surfactant concentration of mixed (a) STFS/$C_{12}E_6$ and (b) STFS/SDS in varying molar ratios. Errors shown on the graphs are from five measurements of the same data point by the du Nouy ring during the experiment, after equilibration had occurred.

mixture at room temperature. Some STFS/$C_{12}E_6$ mixtures were measured at both room temperature (25 °C) and 50 °C for direct comparison with STFS/SDS (shown in Fig. S2 in Supplementary Information). As the CMC values showed minimal temperature dependence, only results from room temperature will be discussed for STFS/$C_{12}E_6$. The primary effect of elevated temperature was an overall reduction in surface tension, attributed to a weakening of cohesive forces between water molecules. In the following discussion, concentration refers to the total moles of all surfactants in solution, while composition is expressed as the molar ratio of the surfactant components. The surface tension data (Fig. 4) show distinct pre-micellar behaviours for the two systems. The surface tension data for STFS/$C_{12}E_6$ (Fig. 4a) shows a variation in the gradient prior to the CMC between the three molar ratios and therefore differences in preferential adsorption to the interface. However, post-CMC surface tensions remain similar at ~35 mN/m regardless of the molar ratio composition, with CMC values significantly lower than those predicted by RST ideal mixing (Fig. 5). In contrast, STFS/SDS (Fig. 4b) exhibits an invariant pre-micellar gradient across molar ratios, indicating a consistent adsorption profile, while post-CMC surface tensions remain in a stable range of ~30 mN/m.

Experimental data for STFS/$C_{12}E_6$ aligns with expectations for an anionic-non-ionic surfactant mixture, exhibiting a clear synergism of the micellar system highlighted in Fig. 5 (open squares) with a strong negative deviation from RST ideal mixing (solid squares) across all compositions. The interaction parameter, $\beta = -6.68$, indicates highly favourable mixing, exceeding the SDS/$C_{12}E_6$ system, which has reported literature values ranging between −2.6 to -4 [64]. This favourable mixing leads to an early onset of micelle formation and in turn, CMC values much lower than those of either individual surfactant. RST predictions for STFS mole fractions in the micelle (Table 3) show that increasing bulk STFS composition leads to greater STFS incorporation into the micelle. However, $C_{12}E_6$ is preferentially incorporated in the micelle at all compositions, likely to shield the strong electrostatic repulsions between the sulfonate head groups. This behaviour is expected, as the surfactant with the lower CMC (indicating a more favourable free energy of micellisation) normally dominates micelle composition at the onset of micellisation. Consequently, STFS is dominant in the STFS/SDS micelles but remains the minority species in STFS/$C_{12}E_6$ micelles. Due to low ionic surfactant concentrations, conductivity measurements were unsuitable for CMC determination of STFS/$C_{12}E_6$, as no distinguishable gradient variation was observed across a wide concentration range. Therefore, CMC values for anionic/non-ionic systems were determined solely from surface tension measurements, where a clear breakpoint was observed.

Anionic-anionic surfactant mixtures of STFS/SDS gave rise to much more unusual micellisation behaviour. Whilst there is some literature discussing anionic-anionic surfactant systems [52,65–67], such mixtures are less commonly studied than those involving different headgroup classifications. Previous studies suggest that most surfactant mixtures of the same classification type (e.g. anionic-anionic) exhibit near-ideal mixing ($\beta \approx 0$) [68] or only slightly synergistic/antagonistic deviations ($\beta < \pm 1.5$). This binary system was selected to probe whether the furan ring presence and the longer C14 alkyl chain in STFS could misalign the sulfonate-sulfate headgroups sufficiently to promote favourable mixing.

Surface tension measurements revealed a distinct minimum (Fig. 4b), which may arise from impurities in either the STFS or the SDS. Alternatively, this behaviour could reflect an extended transition region prior to micelle formation, given the relatively broad concentration range (~1 mM) over which the minimum occurs. In this region, the surface is fully saturated with surfactant molecules and any surface-active impurities, but micellisation has not yet commenced. In solution, small aggregates and dimers may form before the concentration is further increased and mixed micelles begin to form. Conductivity measurements further support this interpretation, showing a gradual rather than abrupt change in slope (Fig. S3), indicating a continuous transition rather than distinct pre- and post-micellar regions. This behaviour likely stems from differences in hydrophobicity and solubility between the two anionic surfactants, where STFS may begin to self-aggregate before SDS reaches a concentration at which mixed micellisation becomes thermodynamically favourable.

In Table 3 the conductivity CMC values for STFS/SDS were averaged with surface tension CMC measurements giving a β parameter of −2.91, indicating synergistic mixing between the two anionic surfactants. This result may seem unexpected given the strong electrostatic repulsions between the sulfonate-sulfate head groups. A comparable system, sodium dodecyl benzene sulfonate (SDBS) mixed with SDS, exhibited an average β parameter of +0.66 [65], suggesting slight antagonistic deviations from ideal mixing, attributed to steric hindrance from the benzene ring. In contrast, the synergistic behaviour observed for STFS/SDS may arise from differences in alkyl chain length and/or the presence of the slightly polar furan ring, which could reduce electrostatic repulsion and promote more favourable packing within the mixed micelles.

5.3. Ternary mixture (STFS/SDS/$C_{12}E_6$)

Ternary surfactant mixtures can exhibit complex behaviour due to the myriads of interaction possibilities, which are reflected in the CMC values. Most studies simplify ternary mixing of surfactants by considering only binary pairwise interactions, extending RST by using binary β parameters to predict ternary behaviour [27,69,70].

Table 4 outlines the predicted CMC values assuming ideal mixing ($\beta = 0$), the RST predicted CMC (derived from experimental binary β parameters) and the experimentally determined ternary CMC values for varying molar ratios of the three components. Consistent with the behaviour of STFS/$C_{12}E_6$ binary mixtures, experimental ternary CMC values are sufficiently low that conductivity measurements show minimal gradient variation due to low ionic strength, making precise CMC determination difficult. Surface tension data, however, shows a clear breakpoint to yield definitive CMC values (Fig. S5). Regardless of composition, equilibrium surface tension at concentrations above the CMC remain similar, ranging between 35 and 38 mN/m.

Table 3
– Thermodynamic and surface properties of the binary mixed micelle system. CMC_{ideal} is the predicted CMC for ideal mixing using RST ($\beta = 0$), CMC_{ST} is the experimental CMC using surface tension only and CMC_{Av} is the combined averaged CMC using surface tension and conductivity techniques. X_{STFS} is the mole fraction of STFS within the micelle, estimated from experimental data using RST. Experiments were performed at least twice to provide uncertainty estimations.

	Temperature (°C)	CMC_{ideal}, (mM)	CMC_{ST}, (mM)	CMC_{Av}, (mM)	γ above CMC (mN/m)	X_{STFS}, (RST)	Interaction Parameter, β
STFS:$C_{12}E_6$	25						
1:2		0.12	0.040 (±0.003)	–	34.1 ± 0.4	0.34 (±0.03)	−6.68 (±0.26)
1:1		0.16	0.038 (±0.004)	–	35.1 ± 0.6	0.39 (±0.04)	
2:1		0.21	0.050 (±0.006)	–	36.5 ± 0.4	0.42 (±0.05)	
STFS:SDS	50						
1:2		1.81	–	1.054 (±0.054)	28.4 ± 0.6	0.68 (±0.03)	−2.91 (±0.17)
1:1		1.29	–	0.893 (±0.082)	27.5 ± 0.4	0.75 (±0.07)	
2:1		1.03	–	0.720 (±0.115)	29.6 ± 1.9	0.78 (±0.06)	

Table 4
- Thermodynamic and surface properties of the ternary mixed micelle systems measured at 25 °C. Experiments were performed at least twice to provide error estimations.

	Predicted CMC, ideal mixing (mM)	Predicted CMC, RST β (mM)	Experimental CMC, Surface tension (mM)	Surface tension, γ above CMC (mN/m)
		STFS: SDS: $C_{12}E_6$		
1:1:1	**0.214**	**0.040**	**0.061 (± 0.002)**	**36.5 ± 0.3**
1:2:1	**0.282**	**0.046**	**0.089 (± 0.008)**	**36.3 ± 0.7**
1:1:2	**0.151**	**0.046**	**0.069 (± 0.008)**	**36.7 ± 1.0**
2:1:1	**0.258**	**0.026**	**0.072 (± 0.003)**	**36.2 ± 0.4**
1:2:2	**0.320**	**0.049**	**0.065 (± 0.009)**	**37.0 ± 0.2**
2:1:2	**0.179**	**0.032**	**0.053 (± 0.002)**	**37.9 ± 0.3**
2:2:1	**0.187**	**0.031**	**0.083 (± 0.002)**	**35.1 ± 0.4**

All ternary compositions exhibit a negative deviation from ideal mixing (Fig. 6), indicating a strong driving force for micellisation. Whilst experimental CMC values are closer in value to those predicted using the RST binary β parameters than those assuming ideal interactions (β = 0) they do not align fully, demonstrating that the interactions of the ternary systems cannot be solely described using binary pairwise interactions and additional contributions must be considered. Although the CMC values are relatively similar across compositions, an increasing proportion of anionic surfactant (STFS or SDS) leads to a higher CMC, consistent with their inherently higher individual CMC values in comparison to the non-ionic $C_{12}E_6$. Whilst solution molar ratios may not fully reflect micellar composition, the variations in CMC between ratios is a confirmation that all three components are present and contributing towards the micelle. Notably, all mixed micelle CMC values are close to that of pure $C_{12}E_6$ which is advantageous for formulations, allowing the use of anionic surfactants at much lower concentrations than required for single component systems.

5.4. Small angle neutron scattering

SANS was utilised to probe the micellar shape, size and composition of pure STFS as well as its binary and ternary mixtures with SDS and $C_{12}E_6$. Measurements were conducted at three concentrations, but the most dilute solutions (5 mM) exhibited weak scattering, resulting in poor fitting and large parameter errors. This data is included in the supplementary information and not discussed in further detail here. Micelle compositions were determined using simultaneous equations of the alkyl core scattering length density (SLD) values after fitting the multiple alkyl tail deuteration contrasts. Initial volume fractions, prior to fitting, were estimated assuming a density of 1 g/cm^3, based on surfactant concentration and solution composition. The micelle core was modelled as containing only the surfactant alkyl tails, while the furan ring, sulfonate/sulfate groups and the ethylene oxide chains were assumed to reside fully in the hydrated shell region. Aggregation numbers were determined by dividing the total core volume by the individual tail volume, calculated using Tanfords formula, $v = 27.4 + 26.9.n_c^{70}$, where n_c represents the number of carbons in the alkyl chain (C_{12} for SDS and $C_{12}E_6$, C_{14} for STFS) in the proportions calculated from the micelle composition. Shell hydration (Fig. S8b and S8d) was calculated from the volume difference between the total shell volume and the occupied headgroup volume. Various models were trialled for data fitting, however, the polydisperse core shell sphere model outlined in the methods section above gave the best fitting results for the mixed systems and so was preferred as the simplest description for most of the observed scattering patterns. Pure STFS micelles required use of a prolate micelle shape to achieve good fits.

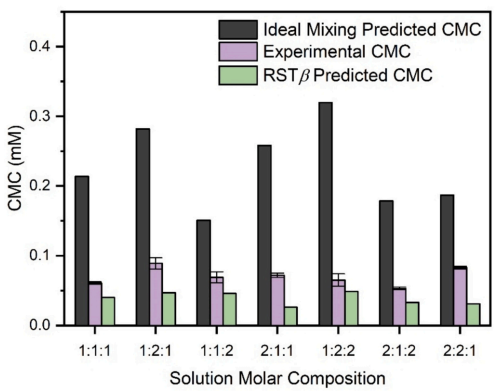

Fig. 6. CMC values for the ternary STFS:SDS:$C_{12}E_6$ mixtures in varying solution compositions. The black column denotes CMC values predicted for ideal mixing (β = 0), the purple denotes the experimentally determined CMC values and green represents the predicted CMC values using the β parameters obtained from the individual binary mixtures.

5.5. STFS

SANS measurements of STFS solutions were run at concentrations of 10–50 mM using multiple contrasts by varying the H_2O/D_2O ratio, with STFS fully hydrogenated. Fig. 7 illustrates the expected increase in structure factor with increasing concentration, consistent with increased electrostatic repulsions between charged micelles. While a polydisperse core-shell sphere form factor adequately described scattering from the mixtures, pure STFS scattering data required a prolate ellipsoidal form factor model [71]. Model parameters, outlined in Table 5, indicate that the shape and size of pure STFS micelles remain invariant with increasing concentration, with total major and minor axis diameters of $d_1 = 34.2 \pm 0.3$ Å and $d_2 = 26.3 \pm 1.6$ Å respectively and an aggregation number of 103 ± 2. An increase in apparent surface charge can be seen with increasing concentration, resulting from the larger structure factor contribution to the scattering, as described by this model.

5.6. Binary mixtures (STFS/SDS and STFS/$C_{12}E_6$)

The self-assembly behaviour of the binary mixtures was explored at dilute concentrations (5, 10 and 20 mM) to investigate non-ideal mixing effects, identified by the previously reported CMC data. To further examine these effects, the same three molar ratios (2:1, 1:1 and 1:2) were studied to determine whether equimolar compositions or a mixture dominated by one component induced deviations in micellar composition relative to the solution ratios. Measurements were performed at

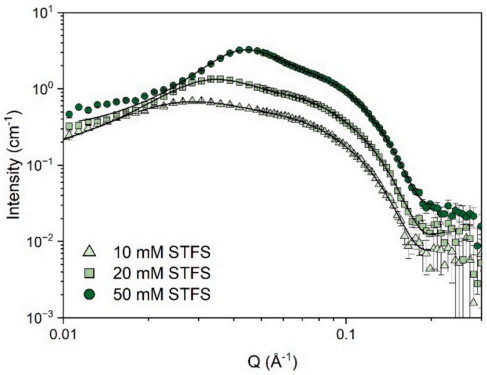

Fig. 7. SANS data for increasing concentration (10, 20 and 50 mM) of h-STFS in 100 % D2O.

Table 5
– Key parameters from prolate ellipsoid core shell fitting of STFS SANS data collected at 45 °C. r_1 and r_2 represent the major and minor axis of the core respectively, t_s represents the shell thickness and N_{agg} is the aggregation number of the micelle.

c (mM)	Volume fraction, Φ	Surface charge, z (±1)	r_1 (Å) (±1 Å)	r_2 (Å) (±1 Å)	t_s (Å) (±1 Å)	N_{agg} (±5)
STFS						
10	**0.00575 (±0.00025)**	**11.3**	**25.8**	**19.8**	**8.7**	**106**
20	**0.00935 (±0.00015)**	**14.7**	**27.2**	**19.0**	**6.7**	**102**
50	**0.02200 (±0.00200)**	**18.4**	**28.0**	**18.6**	**6.1**	**101**

both room temperature (25 °C) and elevated temperatures (45 °C) to examine temperature dependent effects (Fig. S7). Minimal changes in the fitted parameters were observed for STFS/$C_{12}E_6$, therefore only room temperature results will be discussed, with high temperature fitted parameters provided in SI Table S6/7.

5.7. STFS/$C_{12}E_6$

SANS data for binary STFS/$C_{12}E_6$ mixtures reveals that micelles remain small, polydisperse and globular across all compositions and concentrations. Increasing concentration primarily enhances the structure factor peak, indicating a higher micelle volume fraction and greater inter-micellar interactions, without evidence of elongation into ellipsoids in this dilute concentration range. Micelle compositions largely reflect the bulk mole fraction of each surfactant, contrasting with CMC data that suggested enrichment of $C_{12}E_6$ within micelles contributing to its lower CMC value through reduction of the electrostatic repulsions. These findings suggest that while synergistic interactions promote micellisation at concentrations close to the CMC, mixing behaviour approaches the bulk solution molar ratio at higher concentrations, as is often seen is surfactant mixtures [49].

The shape and size of these small globular micelles are likely determined by an intricate balance between the steric hindrance of the large ethylene oxide groups present in the $C_{12}E_6$ and the electrostatic repulsions of the furan sulfonate head groups. Shiloach and Blankschtein [72] observed that in SDS or SDE_6S (a structural analogue of SDS with 6 ethylene oxide (EO) groups between the sulfate and the C_{12} alkyl chain) mixed with $C_{12}E_6$, CMCs values remained largely unchanged. They concluded that electrostatic interactions, rather than steric effects, predominantly govern micelle behaviour in systems with sulfate and polyoxyethylene head groups. This was reiterated by Garamus [47], where in the absence of salt, electrostatic interactions were found to dominate, leading to monotonic changes in micelle properties with no maxima observed in the aggregation number across all solution compositions for SDS/$C_{12}E_6$.

Table 6 summarises the key model parameters for the fitted SANS data across varying concentrations and solution compositions. The observed apparent core radii, ranging from 18.7 to 22.0 Å, exceed the fully extended alkyl chain length, estimated using the commonly reported Tanford equation $l_c = 1.265n_c + 1.50$ [73]. From this calculation, C_{12} and C_{14} chains would be expected to be ~16.7 Å and 19.2 Å at full extension respectively. This discrepancy may arise due to the fluxional polydispersity of the micelles, leading to deviations from a perfectly spherical shape or from partial incorporation of the STFS furan ring into the core despite its polar nature. Additionally, the difference in chain length between C_{12} and C_{14} surfactants may cause misalignment or inefficient packing in the core, further contributing to a slightly larger core radius than expected. To address such discrepancies, studies on similar mixed micelle systems [33,74,75] introduce an additional model parameter "ext" to account for variations in packing constraints, including uncertainties in the alkyl core/headgroup interface, while

Table 6
– Fitted parameters extracted from the SANS data fitted using a polydisperse core-shell sphere model with a Hayter Penfold structure factor at 25 °C for STFS/$C_{12}E_6$ mixtures.

	c (mM)	Volume fraction, Φ	Surface charge, z (± 1)	r_c (Å) (±1 Å)	t_s (Å) (±1 Å)	N_{agg} (± 5)	Polydispersity (%) (± 1)	Solution composition (Mol fraction of STFS)	Micellar composition (Mol fraction of STFS)
STFS: $C_{12}E_6$	**10**								
1:2		**0.00415 (±0.00015)**	**17.8**	**19.6**	**6.7**	**85**	**14**	**0.33**	**0.38 ± 0.02**
1:1		**0.00425 (±0.00025)**	**22.1**	**18.7**	**8.3**	**73**	**8**	**0.50**	**0.49 ± 0.01**
2:1		**0.00445 (±0.00015)**	**22.4**	**21.1**	**5.8**	**100**	**10**	**0.66**	**0.78 ± 0.01**
	20								
1:2		**0.00845 (±0.00045)**	**21.9**	**20.0**	**7.2**	**92**	**14**	**0.33**	**0.34 ± 0.00**
1:1		**0.00835 (±0.00035)**	**24.5**	**20.4**	**6.7**	**94**	**11**	**0.50**	**0.55 ± 0.01**
2:1		**0.00865 (±0.00025)**	**26.0**	**22.0**	**5.7**	**114**	**11**	**0.66**	**0.74 ± 0.01**

keeping the alkyl chain core radius fixed at the fully extended tail length during fitting. We did not however feel it was appropriate to introduce a further variable in our fitting models, to avoid over fitting; the polydisperse core-shell sphere model fits well and accounts for all the features seen in our scattering data. The shell thickness, t_s, for all STFS/$C_{12}E_6$ samples is consistent with literature values for SDS/$C_{12}E_6$ mixtures, typically between 5 and 8 Å[47]. While a fully extended E_6 head group measures ~21 Å in length [76,77], such extension is entropically unfavourable due to loss of conformational freedoms. For micelles of SDS/$C_{12}E_6$ mixtures [49] in electrolyte solutions, shell thicknesses (including the hydration layer) were reported to lie between 5 and 10 Å, implying coiling of the EO head group. The hydrophilic or hydrophobic classification of the furan group remains unclear with analogous studies on SDBS, featuring a benzene ring instead of a furan, classifying the aromatic ring as part of the hydrophilic shell, due to the steric hindrance and rigidity of the ring relative to the flexibility of the alkyl chains comprising the micelle core [10,12,78]. Although the furan oxygen imparts slight polarity to this group, it is likely less hydrophilic than water or surrounding polar groups, with MD simulations between furan and a water molecule showing that the furan oxygen acts as a much weaker hydrogen bond accepter than similar structures [79] so the EO chains likely coil tightly to reduce less favourable interactions between themselves and the less polar furan.

Previous studies on anionic/non-ionic mixtures report slight micellar growth and a reduction in the micelle charge with increasing non-ionic content [7,47] [7], which is partially consistent with our findings. In anionic-rich solutions, electrostatic interactions dominate, whereas steric effects prevail in non-ionic conditions. As shown in Fig. 8a, increased $C_{12}E_6$ content reduces structure factor contributions, reflecting a decreased micellar surface charge due to the increased shielding from the EO groups. Micelle size remains consistent however, with no significant micellar growth with increasing $C_{12}E_6$ content. Similarly, an increase in total surfactant concentration (Fig. 8b) does not induce micellar growth, but instead increases the micelle volume fraction, shifting the structure factor peak to higher q.

5.8. STFS/SDS

Anionic/anionic mixtures (Fig. 9) were insoluble at room temperature due to the high Krafft temperature of STFS and were therefore studied at 45 °C to ensure solubility within application-relevant conditions. Scattering patterns for mixtures containing h-SDS or d-SDS overlapped almost entirely (Fig. S8), indicating minimal SDS incorporation into the small polydisperse globular micelles across all compositions. A slight increase in SDS presence within micelles occurs at higher surfactant concentrations, suggesting a shift towards bulk solution molar ratio mixing behaviour as concentrations significantly exceed the CMC.

Compared to the anionic/non-ionic mixtures, the core radius remains similar as both systems are composed of C14/C12 alkyl chains. The shell thickness for all molar ratios of STFS/SDS also remains constant and comparable (within the technique resolution) to STFS alone, STFS/$C_{12}E_6$, as well as literature values for SDS at similar concentrations [80]. Considering the significant headgroup volume difference between SDS (57.9 Å^3) and $C_{12}E_6$ (397.6 Å^3), variation in the shell thickness would be expected. However, it appears the thickness of the polar region is restricted by the STFS, regardless of the secondary component of the binary mixture. Other model parameters (See Table 7) for these mixtures also align closely with previous literature on SDS micellar solutions [80].

Surface charge is significantly lower in the anionic/anionic mixtures compared to STFS/$C_{12}E_6$. In anionic/non-ionic systems, the non-ionic component shields electrostatic repulsions between the sulfonates, resulting in a diffuse counterion double layer that imparts a higher apparent surface charge. In contrast, the anionic/anionic mixture relies on counterions to screen the strong sulfate-sulfonate repulsion, leading to counterion condensation. This effect reduces the effective surface

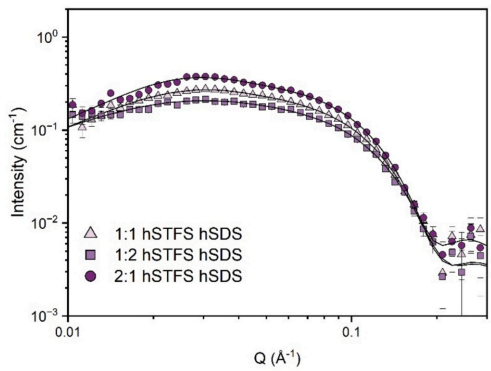

Fig. 9. - SANS data for 10 mM hSTFS: hSDS at varying molar ratios. Solid lines indicate model fits as previously described.

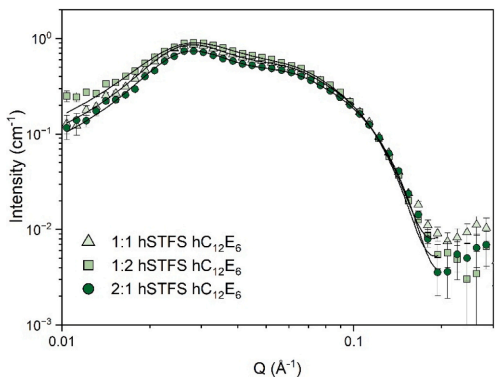

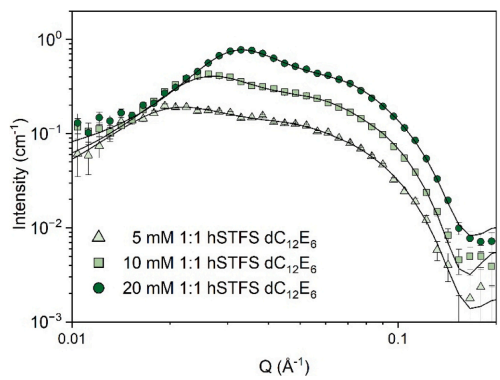

Fig. 8. a - SANS data for 10 mM hSTFS: $hC_{12}E_6$ at varying molar ratios at 25 °C. Solid lines indicate model fits as previously described.b - SANS data for 1:1 hSTFS: $dC_{12}E_6$ at varying concentrations at 25 °C. Solid lines indicate the model fits as previously described.

Table 7
- Parameters extracted from the polydisperse core-shell SANS model with a Hayter Penfold structure factor at 45 °C for STFS/SDS Mixtures.

	c (mM)	Volume fraction, Φ	Surface charge, z (±1)	r_c (Å) (±1 Å)	t_s (Å) (±1 Å)	N_{agg} (±5)	Polydispersity (%) (±1)	Solution composition (Mol fraction of STFS)	Micellar composition (Mol fraction of STFS)
STFS: SDS	**10**								
1:2		**0.00220 (±0.00030)**	**6.9**	**18.9**	**4.8**	**70**	**13**	**0.33**	**0.84 ± 0.02**
1:1		**0.00355 (±0.00015)**	**8.7**	**18.9**	**6.6**	**69**	**11**	**0.50**	**0.94 ± 0.05**
2:1		**0.00375 (±0.00055)**	**10.2**	**21.2**	**4.4**	**102**	**10**	**0.66**	**0.79 ± 0.03**
	20								
1:2		**0.00785 (±0.00015)**	**9.6**	**19.3**	**6.7**	**80**	**9**	**0.33**	**0.47 ± 0.01**
1:1		**0.00860 (±0.00010)**	**10.2**	**20.2**	**6.7**	**88**	**13**	**0.50**	**0.73 ± 0.01**
2:1		**0.00795 (±0.00015)**	**13.1**	**19.8**	**6.8**	**81**	**7**	**0.66**	**0.85 ± 0.01**

charge of the micelles by partially neutralizing the electrostatic repulsions between the charged headgroups.

5.9. Ternary mixtures (STFS/SDS/$C_{12}E_6$)

Micelles across all ternary compositions retain a globular shape with a polydispersity of <15 % based on a Schulz size distribution. Contrast variation (Fig. 10b) of the surfactant alkyl tail confirms the incorporation of all three surfactants in the mixed micelle, with fitted parameters summarized in Table 8. Micelle size and shape show minimal variation across compositions within the resolution of the technique. The scattering pattern of the high concentration (20 mM) equimolar ternary system (Fig. 10a, ●) closely resembles pure STFS (▲), in contrast to the elongation observed for pure $C_{12}E_6$ (▼) and the weak scattering pattern for SDS (■), reaffirming that the mixed micelle retains a predominantly globular structure, similar to that of the binary systems.

The fraction of $C_{12}E_6$ in the mixed micelle is close to the bulk solution molar ratio across the solution compositions (Fig. 11c), suggesting competition between the two anionics for the remaining micelle composition. Consistent with the binary STFS/SDS mixtures, the ternary micelle exhibits minimal SDS inclusion, with a limiting mole fraction under 0.3 across all solution compositions. However, SDS inclusion increases slightly with higher SDS concentration in solution (Fig. 11b). STFS, in turn, is present in higher amounts than bulk solution composition predicts (Fig. 11a). Given the high CMC of SDS (8.2 mM), over ten times that of STFS, it likely remains as monomers in solution at these relatively low concentrations due to its higher monomer solubility.

Fig. 12 a illustrates the consistency of the core radius and shell thickness across solution compositions and concentrations, remaining within the resolution limits of the SANS technique (± 1–2 Å) and ranging between 18.3 and 21.6 Å and 5.6–8.5 Å respectively. Aggregation number increases slightly with total surfactant concentration as well as with a greater anionic surfactant fraction in solution (Fig. 12b), reflecting increased monomer availability while being constrained by headgroup repulsions. Typical literature values for the aggregation numbers of the individual surfactant micelles are 103 monomers for $C_{12}E_6$ [81] and 77 for SDS[80] at similar concentrations, with STFS previously noted above at 103. The mixed micelle values fall approximately in the middle of these individual extremes. Micelle surface charge is highly composition dependent, with ternary mixtures exhibiting intermediate behaviour relative to the two binary systems (See Fig. S9). As the anionic surfactant fraction in the micelle increases, surface charge decreases, due to tighter counterion binding, consistent with trends observed in STFS/SDS systems.

6. Conclusions

This study provides a detailed investigation of the micellization and mixing behaviour of sodium 5-tetradecyl furan-2-sulfonate (STFS) in binary and ternary surfactant mixtures with sodium dodecyl sulfate

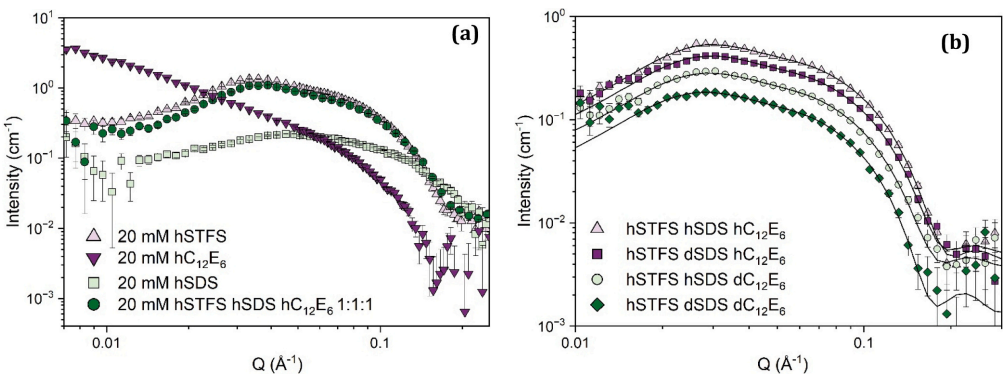

Fig. 10. a - SANS overlay of the individual surfactants in D_2O and the 1:1:1 ternary mixture at 20 mM. b - SANS data of the ternary surfactant mixture at 10 mM in a 1:1:1 Ratio with varying contrasts of hhh (▲), hdh (■), hhd (●) and hdd (◆).

Table 8-
Parameters extracted from the SANS model fitting using a polydisperse core-shell sphere form factor with a Hayter Penfold structure factor at 25 °C for STFS/SDS/$C_{12}E_6$ Mixtures.

	c (mM)	Volume fraction, Φ	Surface charge, z (±1)	r_c (Å) (±1 Å)	t_s (Å) (±1 Å)	N_{agg} (±5)	Polydispersity (%) (±1)	Mol fraction of STFS in micelle	Mol fraction of SDS in micelle	Mol fraction of $C_{12}E_6$ in micelle
STFS: SDS: $C_{12}E_6$										
	10									
1:1:1		**0.00398 (±0.00026)**	**12.4**	**19.4**	**7.4**	**81**	**9**	**0.51 ± 0.02**	**0.14 ± 0.01**	**0.36 ± 0.02**
1:2:1		**0.00390 (±0.00089)**	**9.3**	**19.4**	**8.4**	**77**	**13**	**0.70 ± 0.24**	**0.15 ± 0.05**	**0.19 ± 0.06**
1:1:2		**0.00365 (±0.00038)**	**14.0**	**18.5**	**6.6**	**73**	**13**	**0.27 ± 0.01**	**0.15 ± 0.01**	**0.59 ± 0.03**
2:1:1		**0.00428 (±0.00013)**	**13.1**	**20.1**	**7.6**	**88**	**4**	**0.66 ± 0.01**	**0.10 ± 0.00**	**0.25 ± 0.00**
2:2:1		**0.00418 (±0.00011)**	**10.5**	**20.3**	**8.0**	**90**	**6**	**0.67 ± 0.06**	**0.14 ± 0.01**	**0.21 ± 0.02**
2:1:2		**0.00408 (±0.00029)**	**15.1**	**19.3**	**7.2**	**80**	**9**	**0.54 ± 0.02**	**0.08 ± 0.00**	**0.39 ± 0.02**
1:2:2		**0.00390 (±0.00074)**	**10.7**	**18.3**	**8.3**	**68**	**11**	**0.45 ± 0.07**	**0.17 ± 0.03**	**0.39 ± 0.06**
	20									
1:1:1		**0.00783 (±0.00040)**	**15.8**	**20.2**	**6.2**	**91**	**11**	**0.47 ± 0.04**	**0.20 ± 0.02**	**0.34 ± 0.03**
1:2:1		**0.00757 (±0.00025)**	**16.0**	**19.9**	**5.9**	**86**	**11**	**0.53 ± 0.01**	**0.19 ± 0.01**	**0.30 ± 0.01**
1:1:2		**0.00780 (±0.00065)**	**18.0**	**19.1**	**7.0**	**79**	**10**	**0.31 ± 0.03**	**0.17 ± 0.02**	**0.52 ± 0.05**
2:1:1		**0.00878 (±0.00019)**	**16.5**	**21.2**	**6.8**	**102**	**9**	**0.65 ± 0.05**	**0.11 ± 0.01**	**0.25 ± 0.02**
2:2:1		**0.01113 (±0.00016)**	**13.1**	**21.6**	**8.5**	**110**	**10**	**0.57 ± 0.05**	**0.22 ± 0.02**	**0.22 ± 0.02**
2:1:2		**0.00803 (±0.00046)**	**18.3**	**19.7**	**6.7**	**85**	**9**	**0.53 ± 0.04**	**0.12 ± 0.01**	**0.36 ± 0.02**
1:2:2		**0.00743 (±0.00058)**	**15.0**	**19.4**	**6.0**	**83**	**12**	**0.31 ± 0.01**	**0.27 ± 0.01**	**0.43 ± 0.02**

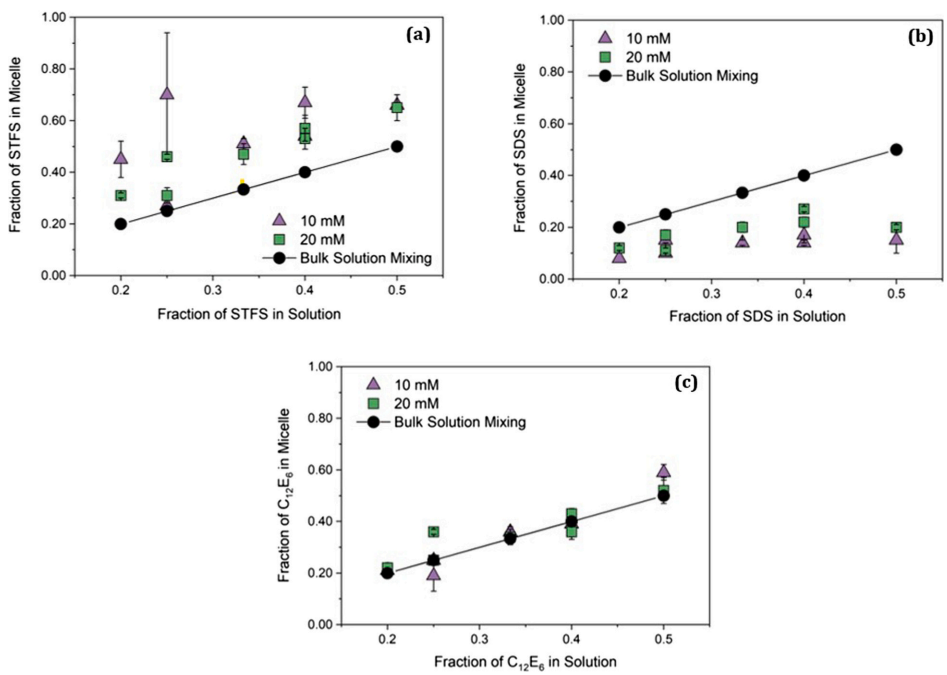

Fig. 11. Composition of component "x" within the micelle determined by the fitted core SLD parameter in comparison to the fraction of the component in solution, where x is (a) STFS (b) SDS or (c) $C_{12}E_6$. Compositions are displayed as 10 mM (▲), 20 mM (■) as well as displaying the predicted composition from mixing at the bulk solution compositions (●).

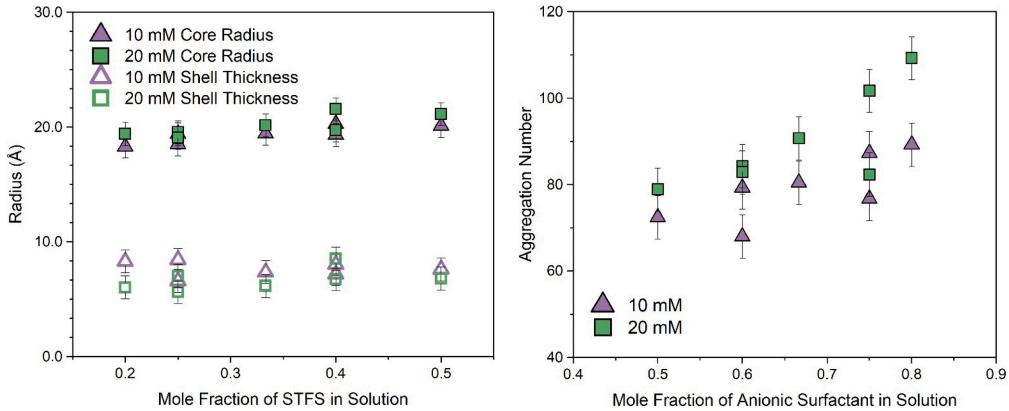

Fig. 12. a – Variation of alkyl core radius at 10 mM (▲) 20 mM (■) and shell thickness at 10 mM (△) and 20 mM (□) with fraction of STFS in the ternary micelle solution. b – Variation in aggregation number for the ternary STFS:SDS:$C_{12}E_6$ system at 10 mM (▲) and 20 mM (■) as a function of the fraction of anionic surfactant (STFS or SDS) in the solution.

(SDS) and hexaethylene glycol monododecyl ether ($C_{12}E_6$). Our hypothesis was that the furan-based head group of STFS could enable favourable micelle mixing in binary and ternary surfactant systems, comparable to other common anionic surfactants such as LAS. The structural and thermodynamic properties of these systems were explored using small-angle neutron scattering (SANS), surface tension, and conductivity measurements across different concentrations, both close to and well above the CMC, and at varying solution molar ratios.

Alone in solution STFS demonstrates typical surfactant self-assembly behaviour, with solutions above the Krafft temperature transitioning from micelles through a 2D hexagonal phase into a liquid crystalline lamellar phase. The dilute phase micelles are prolate ellipsoids which are constant in dimensions over the concentration range studied.

In the mixed micelle systems, small globular micelles are formed. The results demonstrate strong synergistic interactions between STFS and $C_{12}E_6$, leading to significantly reduced critical micelle concentrations and favourable micellar mixing, as indicated by negative deviations from ideality. Fitting of the SANS data in this binary system confirmed the presence of both surfactants in the micelles, with micelle compositions close to those expected from the prepared solutions. In contrast, scattering from the STFS/SDS mixtures, whilst still exhibiting non-ideal mixing, indicated minimal SDS incorporation into micelles at low concentrations, likely due to electrostatic repulsions between the sulfonate and sulfate headgroups. The ternary mixtures showed intermediate behaviour between the two binary extremes with STFS and $C_{12}E_6$ driving micelle formation while SDS is minimally incorporated into the micelle.

This is one of the first detailed structural studies of furan-based anionic surfactants in mixed micellar systems. While previous work has focused on synthesis and applications testing of such surfactants [8,13,82], little has been reported concerning their bulk self-assembly or co-micellisation behaviour. These findings highlight the potential of STFS as a renewable surfactant with tuneable mixed micellization behaviour, offering advantages for detergent formulations by enabling effective micellization at lower surfactant concentrations. Future work will investigate the interfacial properties of these mixtures and explore their performance in more complex formulation environments.

CRediT authorship contribution statement

Laura Deeming: Writing – original draft, Visualization, Methodology, Investigation, Formal analysis, Data curation, Conceptualization. **Niamh R. Leaman:** Writing – review & editing, Investigation. **Dirk Honecker:** Writing – review & editing, Investigation, Data curation. **Yao Chen:** Writing – review & editing, Resources, Investigation. **Kun Ma:** Writing – review & editing, Resources, Investigation. **Karen J. Edler:** Writing – review & editing, Supervision, Resources, Project administration, Funding acquisition, Formal analysis, Conceptualization.

Declaration of competing interest

The authors declare that they have no known competing financial interests or personal relationships that could have appeared to influence the work reported in this paper.

Acknowledgements

LD thanks Unilever and Lund University for co-funding a PhD studentship, as well as the EPSRC (ICASE voucher no. 20000191), the University of Bath and the Centre for Sustainable and Circular Technologies for their support. We thank David Ribar for helpful discussions and coding help for the ternary RST predictions. We thank the ISIS Neutron and Muon Source for beamtime allocations on ZOOM (RB2220094 (**DOI:** https://doi.org/10.5286/ISIS.E.RB2220094-1)) and Larmor (RB2300046 (**DOI:** https://doi.org/10.5286/ISIS.E.RB2300046-1)) instruments, and we also thank the ISIS Deuteration Laboratory for providing the deuterated surfactants. Raw scattering data can be downloaded from the specified DOIs.

Appendix A. Supplementary data

Supplementary data to this article can be found online at https://doi.org/10.1016/j.jcis.2025.138201.

Data availability

A link to the experimental data is included in the paper

References

[1] S. Rebello, A.K. Asok, S. Mundayoor, M.S. Jisha, Environ. Chem. Lett. 12 (2014) 275–287.

[2] E. Guzmán, F. Ortega, R.G. Rubio, Curr. Opin. Colloid Interface Sci. 69 (2024) 101780.
[3] D. Fei, G.-W. Zhou, Z.-Q. Yu, H.-Z. Gang, J.-F. Liu, S.-Z. Yang, R.-Q. Ye, B.-Z. Mu, J. Surfactant Deterg. 23 (2020) 109–118.
[4] S. Pal, N. Chatterjee, A.K. Das, D.J. McClements, P. Dhar, Adv. Colloid Interf. Sci. 313 (2023) 102856.
[5] S. Sohn, P. Do, In Industrial Arene Chemistry, John Wiley & Sons, Ltd, 2023, pp. 729–745.
[6] E. Gayathiri, P. Prakash, N. Karmegam, S. Varjani, M.K. Awasthi, B. Ravindran, Agronomy 12 (2022) 662.
[7] A. Bhadani, A. Kafle, T. Ogura, M. Akamatsu, K. Sakai, H. Sakai, M. Abe, Curr. Opin. Colloid Interface Sci. 45 (2020) 124–135.
[8] D.S. Park, K.E. Joseph, M. Koehle, C. Krumm, L. Ren, J.N. Damen, M.H. Shete, H. S. Lee, X. Zuo, B. Lee, W. Fan, D.G. Vlachos, R.F. Lobo, M. Tsapatsis, P. J. Dauenhauer, ACS Cent. Sci. 2 (2016) 820–824.
[9] H. Nguyen, Y. Wang, D. Moglia, J. Fu, W. Zheng, M. Orazov, D.G. Vlachos, Catal. Sci. Technol. 11 (2021) 2762–2769.
[10] S. Khodaparast, W. Sharratt, H. Wang, E.S.J. Robles, R. Dalgliesh, J.T. Cabral, J. Colloid Interface Sci. 546 (2019) 221–230.
[11] P. Goon, R.G. Bhirud, V.V. Kumar, J. Surfactant Deterg. 2 (1999) 489–493.
[12] A.S. Rafique, S. Khodaparast, A.S. Poulos, W.N. Sharratt, E.S.J. Robles, J.T. Cabral, Soft Matter 16 (2020) 7835–7844.
[13] A. Velty, S. Iborra, A. Corma, ChemSusChem 15 (2022) e202200181.
[14] J.P. Marcolongo, M. Mirenda, J. Chem. Educ. 88 (2011) 629–633.
[15] H. Khan, J.M. Seddon, R.V. Law, N.J. Brooks, E. Robles, J.T. Cabral, O. Ces, J. Colloid Interface Sci. 538 (2019) 75–82.
[16] M.J. Rosen, J.T. Kunjappu, Surfactants and Interfacial Phenomena, John Wiley & Sons, 2012.
[17] M. Alibrahim, Tenside Surfact. Detergents 49 (2012) 330–334.
[18] R.A. Khan, In Environmental Micropollutants, Elsevier, 2022, pp. 117–130.
[19] M. Ludwig, R. Geisler, S. Prévost, R. von Klitzing, Molecules 26 (2021) 4136.
[20] M. Chen, C. Dong, J. Penfold, R.K. Thomas, T.J.P. Smyth, A. Perfumo, R. Marchant, I.M. Banat, P. Stevenson, A. Parry, I. Tucker, R.A. Campbell, Langmuir 27 (2011) 8854–8866.
[21] T.P. Goloub, R.J. Pugh, B.V. Zhmud, J. Colloid Interface Sci. 229 (2000) 72–81.
[22] F. Portet, P.L. Desbene, C. Treiner, J. Colloid Interface Sci. 184 (1996) 216–226.
[23] C. Stubenrauch, P.M. Claesson, M. Rutland, E. Manev, I. Johansson, J.S. Pedersen, D. Langevin, D. Blunk, C.D. Bain, Adv. Colloid Interf. Sci. 155 (2010) 5–18.
[24] P. Bäverbäck, C.L.P. Oliveira, V.M. Garamus, I. Varga, P.M. Claesson, J. Pedersen, Langmuir 25 (2009) 7296–7303.
[25] R. Wang, Y. Li, J. Chem. Eng. Data 58 (2013) 2240–2247.
[26] Y. Zheng, X. Lu, L. Lai, L. Yu, H. Zheng, C. Dai, J. Mol. Liq. 299 (2020) 112108.
[27] A. Graciaa, M. Ben Ghoulam, G. Marion, J. Lachaise, J. Phys. Chem. 93 (1989) 4167–4173.
[28] S.P. Moulik, Md.E. Haque, P.K. Jana, A.R. Das, J. Phys. Chem. 100 (1996) 701–708.
[29] S. Ghosh, J. Colloid Interface Sci. 244 (2001) 128–138.
[30] A. Shiloach, D. Blankschtein, Langmuir 14 (1998) 4105–4114.
[31] Z.H. Ren, J. Huang, Y.C. Zheng, L. Lai, P. Mei, X.R. Yu, Y.L. Chang, J. Mol. Liq. 272 (2018) 380–386.
[32] J. Huang, Z.H. Ren, J. Mol. Liq. 278 (2019) 53–60.
[33] J.R. Liley, J. Penfold, R.K. Thomas, I.M. Tucker, J.T. Petkov, P.S. Stevenson, I. M. Banat, R. Marchant, M. Rudden, A. Terry, I. Grillo, J. Colloid Interface Sci. 487 (2017) 493–503.
[34] Z.O. Et-Tarhouni, E. Carter, D.M. Murphy, P.C. Griffiths, O.T. Mansour, S.M. King, A. Paul, Colloids Surf. A Physicochem. Eng. Asp. 492 (2016) 255–262.
[35] R. Esposito, L. Ingenito, D. Cavasso, A. Siciliano, M.L. Alfieri, L. Chiappisi, G. Fragneto, M.F. Ottaviani, M. Guida, L. Paduano, G. D'Errico, J. Mol. Liq. 367 (2022) 120547.
[36] H. Belarbi, F. Bouanani, J. Mol. Liq. 383 (2023) 122060.
[37] V.P. Arkhipov, R.V. Arkhipov, E.V. Petrova, A. Filippov, Magn. Reson. Chem. 61 (2023) 345–355.
[38] S. Khodaparast, W.N. Sharratt, G. Tyagi, R.M. Dalgliesh, E.S.J. Robles, J.T. Cabral, J. Colloid Interface Sci. 582 (2021) 1116–1127.
[39] I.M. Tucker, A. Burley, R. Petkova, S. Hosking, J.R.P. Webster, P.X. Li, K. Ma, J. Doutch, J. Penfold, R. Thomas, J. Colloid Interface Sci. 626 (2022) 305–313.
[40] M. Zheng, T. Suzuki, Inoue and B. Lindman, Langmuir 18 (2002) 9204–9210.
[41] S. Yoshimura, S. Shirai, Y. Einaga, J. Phys. Chem. B 108 (2004) 15477–15487.
[42] F. Sterpone, G. Briganti, C. Pierleoni, Langmuir 25 (2009) 8960–8967.
[43] B. Hammouda, J. Res. Natl. Inst. Stan. 118 (2013) 151.
[44] F.H. Quina, P.M. Nassar, J.B.S. Bonilha, B.L. Bales, J. Phys. Chem. 99 (1995) 17028–17031.
[45] P.J. Missel, N.A. Mazer, G.B. Benedek, C.Y. Young, M.C. Carey, J. Phys. Chem. 84 (1980) 1044–1057.
[46] P. Baglioni, L. Dei, E. Rivara-Minten, L. Kevan, J. Am. Chem. Soc. 115 (1993) 4286–4290.
[47] V.M. Garamus, Langmuir 19 (2003) 7214–7218.
[48] J. Penfold, E. Staples, I. Tucker, J. Phys. Chem. B 106 (2002) 8891–8897.
[49] J. Penfold, E. Staples, L. Thompson, I. Tucker, J. Hines, R.K. Thomas, J.R. Lu, N. Warren, J. Phys. Chem. B 103 (1999) 5204–5211.
[50] J.H. Clint, J. Chem, Soc., Faraday Trans. 1 (71) (1975) 1327.
[51] D.N. Rubingh, in: K.L. Mittal (Ed.), Solution Chemistry of Surfactants 1, Springer, New York, Boston, MA, 1979, pp. 337–354.
[52] R. Nagarajan, Langmuir 1 (1985) 331–341.
[53] R.F. Kamrath, E.I. Franses, J. Phys. Chem. 88 (1984) 1642–1648.
[54] G.S. Georgiev, Colloid Polym. Sci. 274 (1996) 49–58.
[55] J. Chen, J. Hao, Phys. Chem. Chem. Phys. 15 (2013) 5563–5571.
[56] Y. Wei, X. Wang, L. Dong, G. Liu, Q. Xia, S. Yuan, Colloids Surf. A Physicochem. Eng. Asp. 631 (2021) 127714.
[57] S.R. Kline, J Appl. Cryst. 39 (2006) 895–900.
[58] P. Bartlett, R.H. Ottewill, J. Chem. Phys. 96 (1992) 3306–3318.
[59] P.L. du Noüy, J. Gen. Physiol. 7 (1925) 625–631.
[60] A. Dominguez, A. Fernandez, N. Gonzalez, E. Iglesias, L. Montenegro, J. Chem. Educ. 74 (1997) 1227.
[61] N. Homendra, C.I. Devi, J. Surf. Sci. Technol. 22 (2006) 119–131.
[62] J.-G. Ma, B.J. Boyd, C.J. Drummond, Langmuir 22 (2006) 8646–8654.
[63] J.A. Stewart, A. Saiani, A. Bayly, G.J.T. Tiddy, Colloids Surf. A Physicochem. Eng. Asp. 338 (2009) 155–161.
[64] J. Penfold, E. Staples, L. Thompson, I. Tucker, J. Hines, R.K. Thomas, J.R. Lu, Langmuir 11 (1995) 2496–2503.
[65] S. Vora, A. George, H. Desai, P. Bahadur, J. Surfactant Deterg. 2 (1999) 213–221.
[66] M.E. Haque, A.R. Das, A.K. Rakshit, S.P. Moulik, Langmuir 12 (1996) 4084–4089.
[67] M.J. Rosen, Z.H. Zhu, J. Colloid Interface Sci. 133 (1989) 473–478.
[68] B. Kronberg, K. Holmberg, B. Lindman, Surface Chemistry of Surfactants and Polymers, John Wiley & Sons, 2014.
[69] P.M. Holland, D.N. Rubingh, J. Phys. Chem. 87 (1983) 1984–1990.
[70] J.D. Hines, R.K. Thomas, P.R. Garrett, G.K. Rennie, J. Penfold, J. Phys. Chem. B 102 (1998) 9708–9713.
[71] M. Kotlarchyk, S. Chen, J. Chem. Phys. 79 (1983) 2461–2469.
[72] A. Shiloach, D. Blankschtein, Langmuir 14 (1998) 7166–7182.
[73] C. Tanford, J. Phys. Chem. 76 (1972) 3020–3024.
[74] J. Penfold, M. Chen, R.K. Thomas, C. Dong, T.J.P. Smyth, A. Perfumo, R. Marchant, I.M. Banat, P. Stevenson, A. Parry, I. Tucker, I. Grillo, Langmuir 27 (2011) 8867–8877.
[75] M.L. Chen, J. Penfold, R.K. Thomas, T.J.P. Smyth, A. Perfumo, R. Marchant, I. M. Banat, P. Stevenson, A. Parry, I. Tucker, I. Grillo, Langmuir 26 (2010) 17958–17968.
[76] J.R. Lu, Z.X. Li, R.K. Thomas, E.J. Staples, I. Tucker, J. Penfold, J. Phys. Chem. 97 (1993) 8012–8020.
[77] L. Shi, N.R. Tummala, A. Striolo, Langmuir 26 (2010) 5462–5474.
[78] I. Tucker, J. Penfold, R.K. Thomas, C.C. Dong, S. Golding, C. Gibson, I. Grillo, Langmuir 26 (2010) 10614–10626.
[79] D. Kaur, S. Khanna, Comput, Theor. Chem. 963 (2011) 71–75.
[80] J.B. Hayter, J. Penfold, Colloid Polym. Sci. 261 (1983) 1022–1030.
[81] J. Penfold, E. Staples, I. Tucker, P. Cummins, J. Colloid Interface Sci. 185 (1997) 424–431.
[82] A. Al Ghatta, R.C. Aravenas, Y. Wu, J.M. Perry, J. Lemus, J.P. Hallett, A.C. S. Sustainable, Chem. Eng. 10 (2022) 8846–8855.

Supporting Information

Mixed micellar solutions of an oleo-furan sulfonate surfactant with anionic and non-ionic surfactants

Laura Deeming[ab], Niamh R Leaman[ab], Dirk Honecker[c], Yao Chen[c], Kun Ma[c], Karen J Edler[a]

[a] *Center for Analysis and Synthesis, Department of Chemistry, Lund University, Naturvetarvägen 22, Lund, 223 62, Sweden*
[b] *Division of Physical Chemistry, Department of Chemistry, Naturvetarvägen 22, Lund University, 22362 Lund, Sweden.*
[c] *ISIS Neutron and Muon Source, Science and Technology Facilities Council, Rutherford Appleton Laboratory, Didcot, OX11 0QX, Oxfordshire, United Kingdom*

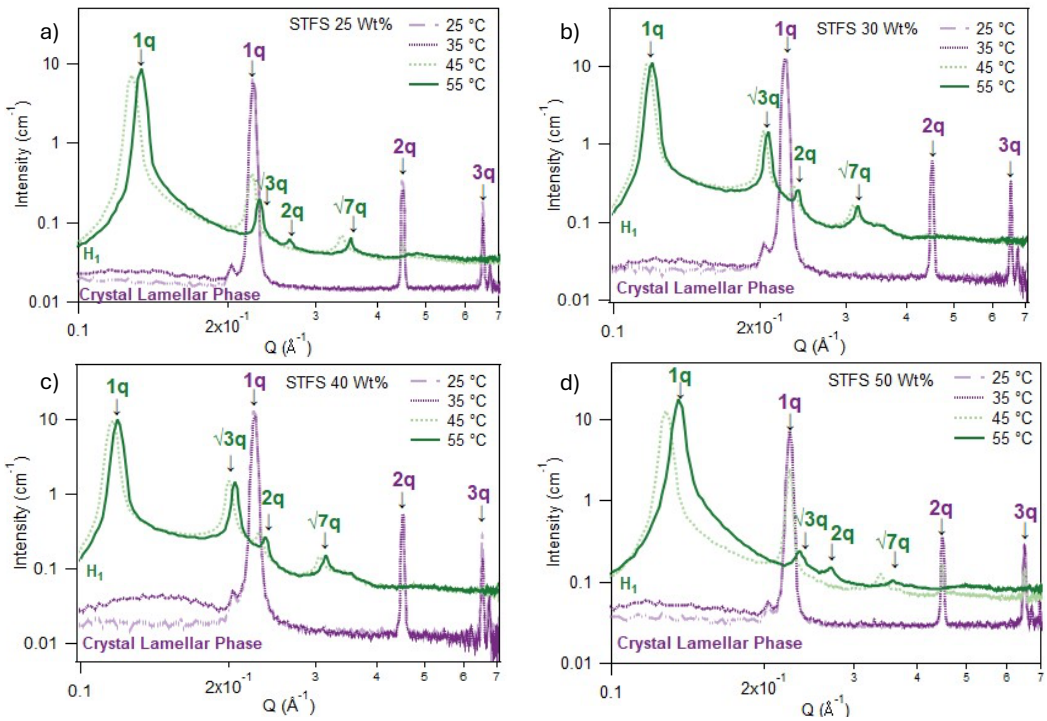

Figure S1 – Small angle X-ray Scattering (SAXS) profiles for sodium tetradecyl furan sulfonate (STFS) at varying concentrations. (a) 25 wt% (b) 30 wt% (c) 40 wt% (d) 50 wt%. Each graph shows SAXS curves measured at multiple temperatures (25, 35, 45 and 55 °C) overlaid to visualise phase changes.

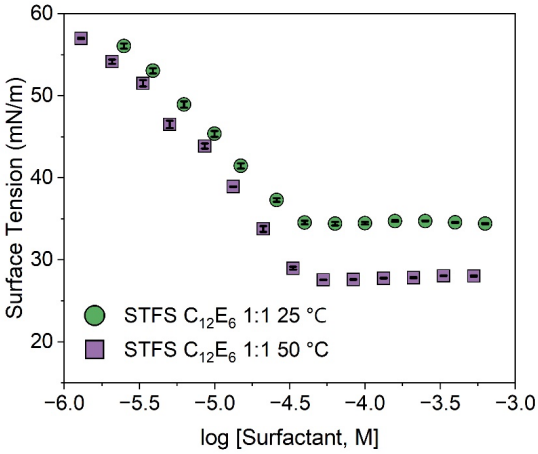

Table S1 – Critical micelle concentration (CMC) and surface tension (γ) above the CMC for STFS/$C_{12}E_6$ at two temperatures.

	25°C	50 °C
CMC (mM)	**0.038** ***(± 0.004)***	**0.044** ***(± 0.006)***
γ above CMC (mN/m)	**35.1 ± 0.6**	**29.7 ± 1.9**

Figure S2 – Equilibrium surface tension (γ) as a function of the total surfactant concentration of STFS $C_{12}E_6$ 1:1 at 25 °C (●) and 50 °C (■). The overlaid curves demonstrate that temperature variation has minimal effect on the CMC, only lowering the final post-CMC surface tension at higher temperatures.

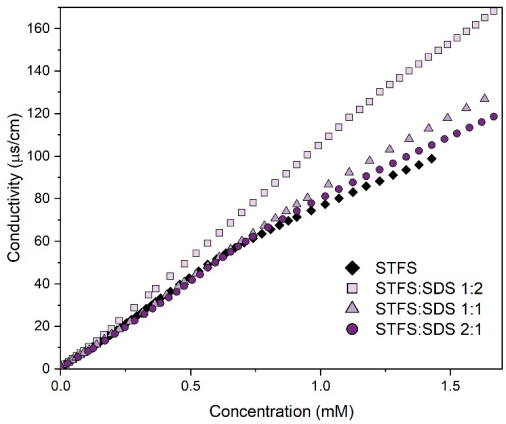

Figure S3 - Conductivity as a function of concentration for STFS (◆) and STFS SDS in three molar ratios, (■) 1:2 (▲) 1:1 and (●) 2:1.

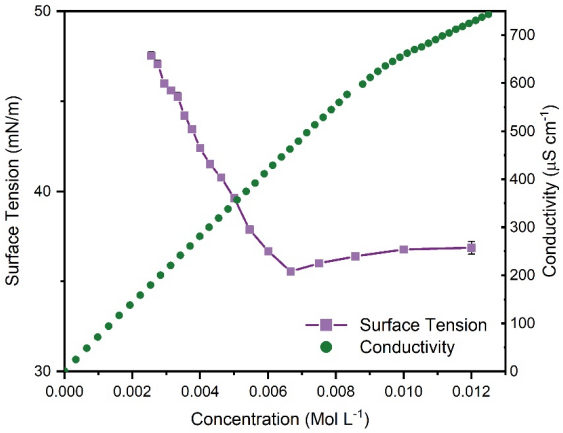

Figure S4 – Determination of the CMC for SDS using tensiometry (■) and conductivity (●) at 50 °C. Uncertainties in data points for both are smaller than symbol size.

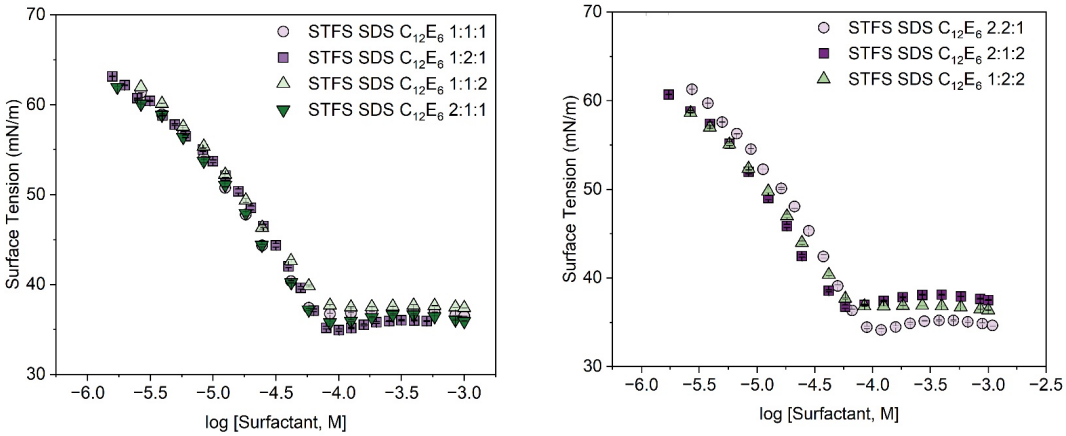

Figure S5 - Equilibrium surface tension as a function of the total surfactant concentration of mixed STFS/SDS/$C_{12}E_6$ in varying molar ratios.

Table S2 –Activity coefficients, f_i, calculated using RST for STFS (1), SDS (2) and $C_{12}E_6$ (3) from experimental CMC data for varying molar ratios of binary STFS/$C_{12}E_6$ and STFS/SDS mixtures.

	Temperature (°C)	f_1	f_2	f_3
STFS:$C_{12}E_6$	**25**			
1:2		**0.056**	**--**	**0.468**
1:1		**0.070**	**--**	**0.353**
2:1		**0.114**	**--**	**0.325**
STFS:SDS	**50**			
1:2		**0.733**	**0.262**	**--**
1:1		**0.846**	**0.220**	**--**
2:1		**0.872**	**0.145**	**--**

Ternary parameters displayed in Table S3 were calculated using a generalised extension of regular solution theory (RST) that considers the ternary system to consist only of linearly additive pairwise interactions. This approach has been used consistently in literature to describe surfactant systems more complex than simple binary mixtures[1,2].

Table S3 – Predicted mole fractions of surfactant within the micelle (X_i) and activity coefficients, f_i, calculated using RST for STFS (1), SDS (2) and $C_{12}E_6$ (3) from experimental CMC data of the individual surfactants combined with the binary β parameters for varying molar ratios of ternary STFS/SDS/$C_{12}E_6$ mixtures.

	X_1	X_2	X_3	f_1	f_2	f_3
STFS: SDS: $C_{12}E_6$						
1:1:1	**0.350**	**0.278**	**0.371**	**0.154**	**0.569**	**0.194**
1:2:1	**0.270**	**0.376**	**0.354**	**0.113**	**0.653**	**0.223**
1:1:2	**0.289**	**0.228**	**0.483**	**0.084**	**0.504**	**0.328**
2:1:1	**0.485**	**0.235**	**0.280**	**0.319**	**0.482**	**0.087**
1:2:2	**0.246**	**0.308**	**0.446**	**0.077**	**0.568**	**0.321**
2:1:2	**0.435**	**0.183**	**0.382**	**0.210**	**0.480**	**0.156**
2:2:1	**0.426**	**0.369**	**0.204**	**0.300**	**0.585**	**0.076**

Scattering Length Density (SLD) Calculations and Fitting

Table S4 – Geometrical constraints and scattering length densities for the tail and head groups of each surfactant used in this study. Tail volumes have been calculated using the Tanford formula[3] and head group volumes are the dry volumes derived from literature cited in the Table or calculated from molecular weight and density.

Component	Molecular Formula	Tail Volume, Tanford Formula[3] (Å³)	Head Group Volume (Å³)	Shell SLD (x10⁻⁶ Å⁻²)	Core SLD (x10⁻⁶ Å⁻²)
h-STFS	$C_{18}H_{31}O_4S$	404.0	151.7	2.98	-0.34
h-SDS	$C_{12}H_{25}O_4S$	350.2	57.9[4]	4.50	-0.37
d-SDS	$C_{12}D_{25}O_4S$	350.2	57.9[4]	4.50	6.60
h-C12E6	$C_{24}H_{50}O_7$	350.2	397.6[5]	0.65	-0.37
d-C12E6	$C_{24}H_{25}D_{25}O_7$	350.2	397.6[5]	0.65	6.60

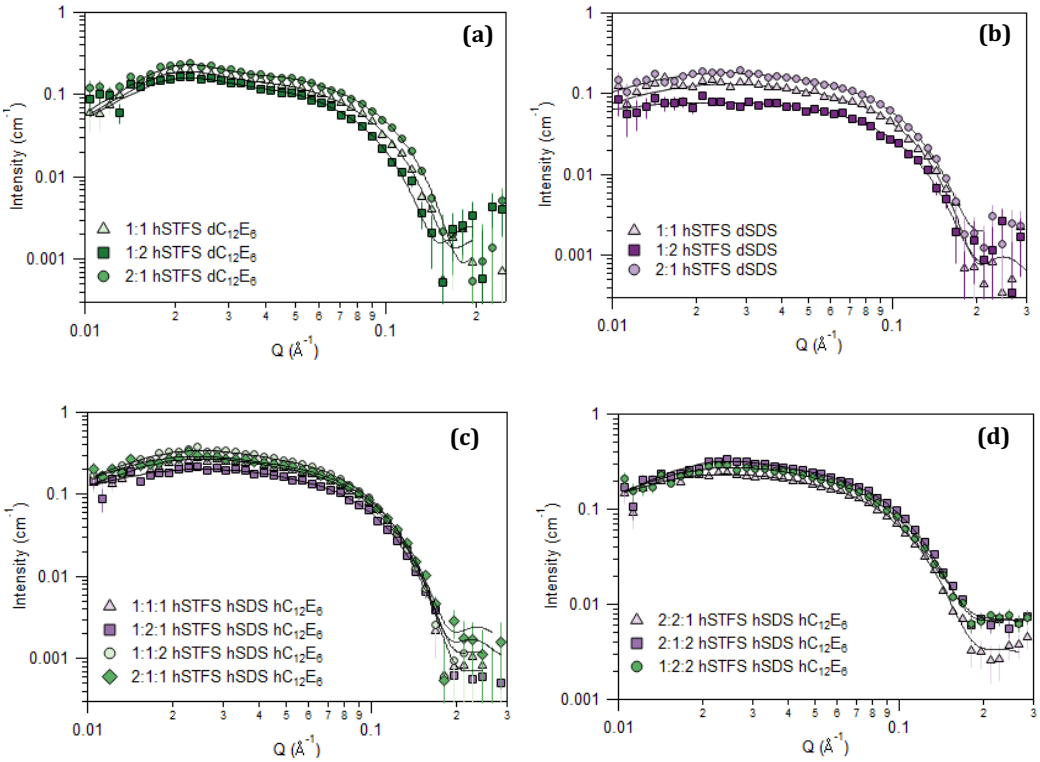

Figure S6 – SANS data for 5 mM (a) hSTFS dC$_{12}$E$_6$ at 25 °C (b) hSTFS dSDS at 45 °C (c) hSTFS hSDS hC$_{12}$E$_6$ at equimolar molar ratio or where 1 component is in excess (d) hSTFS hSDS hC$_{12}$E$_6$ where 2 components are in excess.

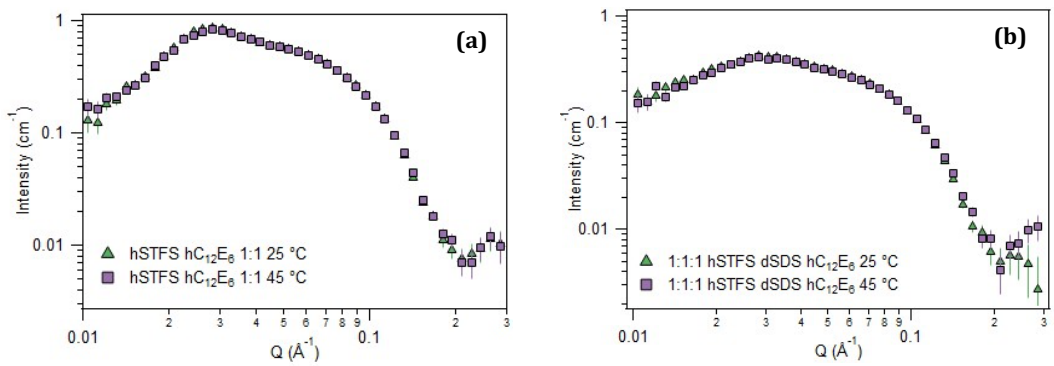

Figure S7 – SANS data for 10 mM (a) 1:1 STFS/C$_{12}$E$_6$ and (b) 1:1:1 STFS/SDS/C$_{12}$E$_6$ at 25 °C (▲) and 45 °C (■), overlaid to show no change in scattering pattern between room and elevated temperatures for samples.

Table S5a – Fitted parameters from SANS data, fit using a polydisperse core-shell sphere model with a Hayter Penfold structure factor at 5 mM for the binary systems of STFS/$C_{12}E_6$ and STFS/SDS. r_1 and r_2 represent the major and minor axis of the core respectively, t_s represents the shell thickness and N_{agg} is the aggregation number of the micelle.

	Temperature (°C)	Volume fraction, Φ	Surface Charge, z (± 1)	r_c (Å) (±1 Å)	t_s (Å) (±1 Å)	N_{agg} (± 5)	Polydispersity (%) (± 1)	Solution Composition (Mol Fraction of STFS)	Micellar Composition (Mol Fraction of STFS)
STFS:$C_{12}E_6$	**25**								
1:2		**0.00215 (± 0.00015)**	**16.9**	**19.3**	**7.5**	**83**	**15**	**0.33**	**0.31 ± 0.01**
1:1		**0.00210 (± 0.00010)**	**19.4**	**21.1**	**6.4**	**103**	**12**	**0.50**	**0.55 ± 0.03**
2:1		**0.00215 (± 0.00005)**	**20.0**	**21.0**	**6.5**	**99**	**10**	**0.67**	**0.70 ± 0.04**
STFS:SDS	**45**								
1:2		**0.00165 (± 0.00005)**	**7.1**	**19.1**	**7.3**	**72**	**6**	**0.33**	**0.85 ± 0.05**
1:1		**0.00125 (± 0.00015)**	**8.4**	**18.4**	**6.0**	**64**	**11**	**0.50**	**0.88 ± 0.37**
2:1		**0.00160 (± 0.00000)**	**8.3**	**19.6**	**5.8**	**77**	**11**	**0.67**	**0.97 ± 0.08**

Table S5b - Fitted parameters from SANS data, fit using a polydisperse core-shell sphere model with a Hayter Penfold structure factor at 5 mM for the ternary systems of STFS/SDS/$C_{12}E_6$ at 25°C. Note that data was not useable for accurate fitting of 2:1:1 and has been omitted.

	c (mM)	Volume fraction, Φ	Surface charge, z (±1)	r_c (Å) (±1 Å)	t_s (Å) (±1 Å)	N_{agg} (±5)	Polydispersity (%) (±1)	Mol Fraction of STFS in Micelle	Mol Fraction of SDS in Micelle	Mol Fraction of $C_{12}E_6$ in Micelle
STFS: SDS: $C_{12}E_6$										
	5									
1:1:1		**0.00195 (±0.00021)**	**9.8**	**17.6**	**8.7**	**61**	**14**	**0.47 ±0.07**	**0.11 ±0.02**	**0.44 ±0.06**
1:2:1		**0.00173 (±0.00037)**	**7.3**	**16.9**	**10.1**	**52**	**11**	**0.54 ±0.22**	**0.13 ±0.05**	**0.35 ±0.15**
1:1:2		**0.00198 (±0.00024)**	**10.3**	**18.4**	**8.2**	**71**	**14**	**0.30 ±0.05**	**0.10 ±0.02**	**0.60 ±0.10**
2:1:1		**---**	**---**	**---**	**---**	**---**	**---**	**---**	**---**	**---**
2:2:1		**0.00143 (±0.00004)**	**8.1**	**18.7**	**5.9**	**72**	**16**	**0.57 ±0.16**	**0.08 ±0.02**	**0.36 ±0.10**
2:1:2		**0.00195 (±0.00005)**	**10.7**	**19.2**	**6.6**	**78**	**14**	**0.50 ±0.07**	**0.03 ±0.00**	**0.48 ±0.07**
1:2:2		**0.00180 (±0.00016)**	**8.3**	**17.2**	**8.2**	**59**	**19**	**0.17 ±0.03**	**0.21 ±0.03**	**0.62 ±0.09**

Table S6 - Fitted parameters extracted from SANS data fit using a polydisperse core-shell sphere model with a Hayter Penfold structure factor at elevated temperatures (45 °C) for STFS/C12E6 mixtures.

	c (mM)	Volume fraction, Φ	Surface Charge, z (± 1)	r_c (Å) (±1 Å)	t_s (Å) (±1 Å)	N_{agg} (± 5)	Polydispersity (%) (± 1)	Solution Composition (Mol Fraction of STFS)	Micellar Composition (Mol Fraction of STFS)
STFS:$C_{12}E_6$	**10**								
1:2		**0.00420 (±0.00010)**	**17.3**	**19.8**	**6.6**	**88**	**15**	**0.33**	**0.36 ±0.02**
1:1		**0.00425 (±0.00025)**	**19.4**	**20.3**	**5.9**	**91**	**14**	**0.50**	**0.62 ±0.04**
2:1		**0.00415 (±0.00005)**	**20.4**	**20.6**	**5.4**	**93**	**11**	**0.66**	**0.74 ±0.02**
	20								
1:2		**0.00865 (±0.00085)**	**17.5**	**19.1**	**8.2**	**81**	**15**	**0.33**	**0.28 ±0.02**
1:1		**0.00835 (±0.00035)**	**19.6**	**20.2**	**6.0**	**91**	**15**	**0.50**	**0.55 ±0.01**
2:1		**0.00865 (±0.00035)**	**20.4**	**20.1**	**6.4**	**87**	**12**	**0.66**	**0.75 ±0.01**

Table 7a - Fitted parameters extracted from SANS data fit using a polydisperse core-shell sphere model with a Hayter Penfold structure factor at elevated temperatures (45 °C) for STFS/SDS/$C_{12}E_6$ mixtures at 10 mM.

	c (mM)	Volume fraction, Φ	Surface charge, z (±1)	r_c (Å) (±1 Å)	t_s (Å) (±1 Å)	N_{agg} (±5)	Polydispersity (%) (±1)	Mol Fraction of STFS in Micelle	Mol Fraction of SDS in Micelle	Mol Fraction of $C_{12}E_6$ in Micelle
STFS: SDS: $C_{12}E_6$										
	10									
1:1:1		**0.00380 (±0.00015)**	**11.7**	**19.0**	**6.5**	**77**	**10**	**0.45 ±0.01**	**0.15 ±0.02**	**0.41 ±0.06**
1:2:1		**0.00388 (±0.00027)**	**9.0**	**19.2**	**6.6**	**78**	**13**	**0.50 ±0.09**	**0.21 ±0.04**	**0.31 ±0.10**
1:1:2		**0.00388 (±0.00011)**	**13.4**	**18.9**	**6.6**	**76**	**13**	**0.33 ±0.06**	**0.13 ±0.01**	**0.54 ±0.05**
2:1:1		**0.00440 (±0.00026)**	**12.5**	**20.8**	**5.8**	**97**	**11**	**0.62 ±0.03**	**0.08 ±0.02**	**0.25 ±0.10**
2:2:1		**0.00383 (±0.00012)**	**9.8**	**18.8**	**7.1**	**72**	**9**	**0.63 ±0.11**	**0.13 ±0.02**	**0.36 ±0.09**
2:1:2		**0.00400 (±0.00022)**	**13.9**	**18.7**	**7.1**	**73**	**11**	**0.53 ±0.09**	**0.07 ±0.03**	**0.41 ±0.07**
1:2:2		**0.00370 (±0.00019)**	**10.8**	**18.5**	**7.2**	**72**	**11**	**0.33 ±0.01**	**0.19 ±0.04**	**0.49 ±0.03**

Table 7b - Fitted parameters extracted from SANS data fit using a polydisperse core-shell sphere model with a Hayter Penfold structure factor at elevated temperatures (45 °C) for STFS/SDS/$C_{12}E_6$ mixtures at 20 mM.

	c (mM)	Volume fraction, Φ	Surface charge, z (±1)	r_c (Å) (±1 Å)	t_s (Å) (±1 Å)	N_{agg} (±5)	Polydispersity (%) (±1)	Mol Fraction of STFS in Micelle	Mol Fraction of SDS in Micelle	Mol Fraction of $C_{12}E_6$ in Micelle
STFS: SDS: $C_{12}E_6$										
	20									
1:1:1		**0.00838 (±0.00017)**	**13.7**	**19.6**	**6.4**	**82**	**13**	**0.53 ±0.05**	**0.17 ±0.02**	**0.31 ±0.05**
1:2:1		**0.00773 (±0.00036)**	**11.9**	**18.7**	**6.7**	**73**	**11**	**0.43 ±0.18**	**0.31 ±0.01**	**0.27 ±0.11**
1:1:2		**0.00793 (±0.00022)**	**15.0**	**19.8**	**5.7**	**86**	**13**	**0.43 ±0.06**	**0.13 ±0.02**	**0.46 ±0.08**
2:1:1		**0.00955 (±0.00029)**	**14.7**	**20.9**	**7.0**	**97**	**12**	**0.69 ±0.05**	**0.10 ±0.03**	**0.23 ±0.07**
2:2:1		**0.00888 (±0.00012)**	**12.2**	**20.0**	**6.5**	**87**	**11**	**0.59 ±0.12**	**0.19 ±0.02**	**0.23 ±0.07**
2:1:2		**0.00810 (±0.00009)**	**16.6**	**19.7**	**6.5**	**84**	**12**	**0.53 ±0.07**	**0.08 ±0.04**	**0.40 ±0.09**
1:2:2		**0.00750 (±0.00021)**	**14.1**	**18.9**	**6.2**	**77**	**13**	**0.30 ±0.05**	**0.25 ±0.02**	**0.45 ±0.11**

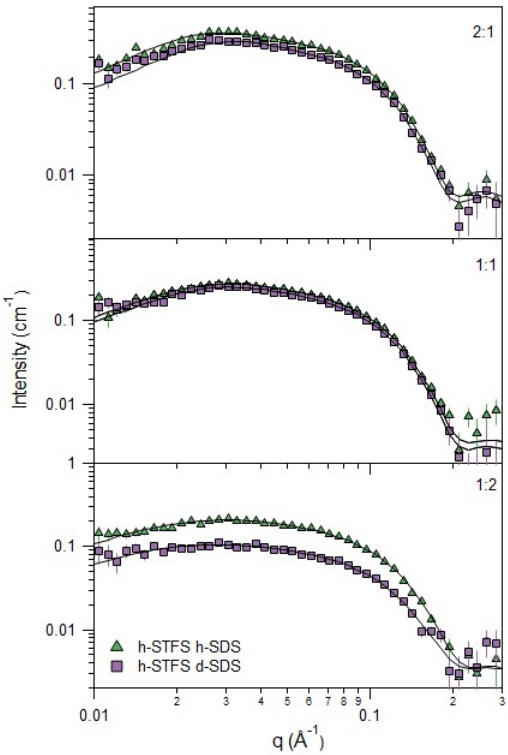

Figure S8 – SANS data at elevated temperature (45 °C) for hSTFS/hSDS (▲) and hSTFS/dSDS (■) at 10 mM to visually demonstrate the minimal inclusion of SDS into the micelle at some molar ratios.

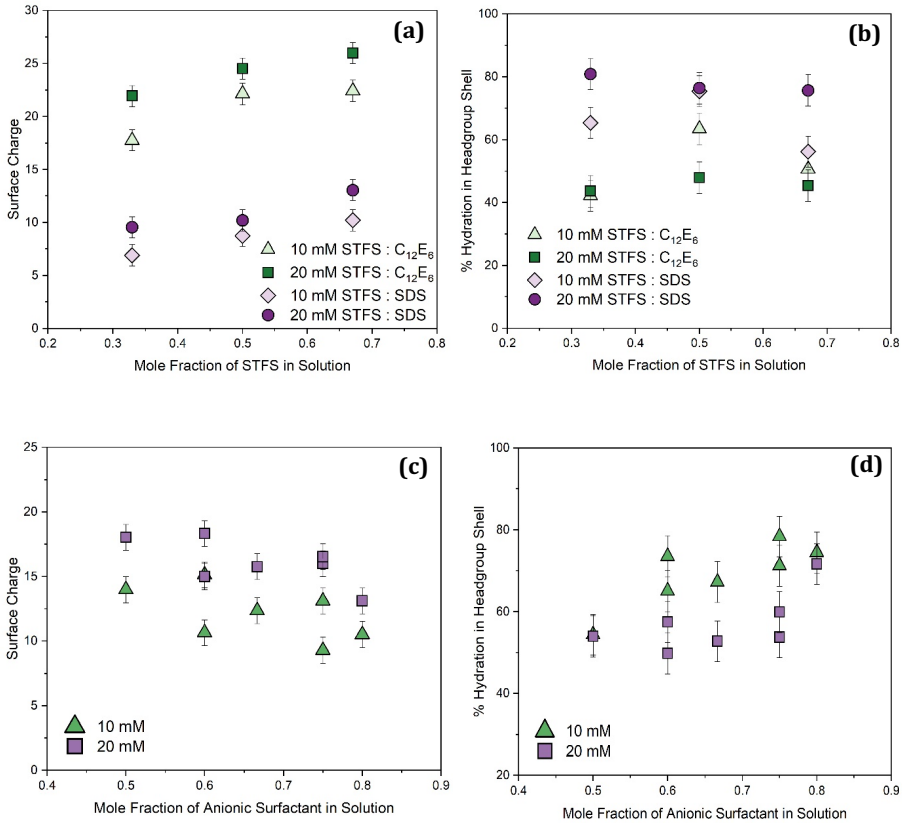

Figure S9 – Additional fitted parameters from SANS data for binary (a) (b) and ternary (c) (d) mixed surfactant systems. Surface charge of the micelle is shown (a) and (c) whilst shell hydration is shown in (b) and (d).

References

1 P. M. Holland and D. N. Rubingh, *J. Phys. Chem.*, 1983, **87**, 1984–1990.
2 A. Shiloach and D. Blankschtein, *Langmuir*, 1998, **14**, 4105–4114.
3 C. Tanford, *J. Phys. Chem.*, 1972, **76**, 3020–3024.
4 E. Caponetti, D. C. Martino, M. A. Floriano and R. Triolo, *Langmuir*, 1997, **13**, 3277–3283.
5 P. Bäverbäck, C. L. P. Oliveira, V. M. Garamus, I. Varga, P. M. Claesson and J. Pedersen, *Langmuir*, 2009, **25**, 7296–7303.

Printed by Media-Tryck, Lund 2025 NORDIC SWAN ECOLABEL 3041 0903

ISBN: 978-91-8096-112-7

Physical Chemistry
Faculty of Science
Lund University